Electronic and Magnetic Properties of Impurities Embedded in Non-Magnetic Finite Hosts

vorgelegt von
Diplom-Physiker
Konstantin Hirsch
aus Berlin

von der Fakultät II - Mathematik und Naturwissenschaften
der Technischen Universität Berlin
zur Erlangung des akademischen Grades

Doktor der Naturwissenschaften
- Dr. rer. nat. -

genehmigte Dissertation

Promotionsausschuss:

Vorsitzender: Prof. Dr. Mario Dähne
Berichter/Gutachter: Prof. Dr. Thomas Möller
Berichter/Gutachter: Prof. Dr. Bernd von Issendorff

Tag der wissenschaftlichen Aussprache: 03. Juni 2013

Berlin 2013
D 83

Kurzfassung

Die elektronischen und magnetischen Eigenschaften einzelner Übergangsmetallatome (Sc, Ti, V, Cr) eingebettet in einen finiten Wirt aus Gold wurde sowohl mit Hilfe von Röntgenabsorptionsspektroskopie und zirkularem Röntgendichroismus als auch mit Hilfe von Dichtefunktionaltheorie am Beispiel von größenselektierten kationischen Clustern in der Gasphase untersucht. Die elektronische Struktur des Dotieratoms hängt sehr empfindlich von der Natur des Fremdatoms, von Quanteneffekten im Wirt sowie deren Zusammensspiel ab. Gerade-ungerade Variationen in der Lokalisierung von Elektronen des Dotieratoms findet man in TiAu_n^+ Clustern und andeutungsweise bereits in ScAu_n^+ Clustern. In VAu_n^+ Clustern hingegen ist die lokale elektronische Struktur des Dotieratoms unabhängig von der Größe des Wirtsclusters. Dennoch lässt sich schlußfolgern, dass es in allen untersuchten Systemen die Tendenz gibt eine gerade Anzahl von Elektronen zu delokalisieren, sofern dies durch die gegebenen Randbedingungen möglich ist.

Das *Anderson impurity model* [1] beschreibt die Wechselwirkung eines einzelnen magnetischen Dotieratoms mit einem homogenen Elektronengas in einer ausgedehnten Festkörperprobe. Für finite Systeme hingegen muss der Einfluß einer Energielücke in der Zustandsdichte des Wirstmaterials berücksichtigt werden. Dies wurde in der vorliegenden Dissertation mit Hilfe eines Hamiltonoperators in *tight binding* Näherung getan. Damit konnte gezeigt werden, dass für finite Systeme grundsätzlich die Beschreibung im *Anderson impurity model* zusammenbricht, und insbesondere der Übergang von magnetischem zu unmagnetischem Verhalten falsch vorhergesagt wird. Es konnte weiterhin gezeigt werden, dass die Energielücke zu einer deutlichen Stabilisierung des Spinmoments des Dotieratoms beiträgt. Die größenabhängige Variation des Spinmoments in nahezu vollständig spinpolarisierten CrAu_n^+ Clustern ist dennoch im Wesentlichen in Übereinstimmung mit dem *Anderson impurity model* [1], da diese Systeme weit vom Übergang von magnetischem zu unmagnetischem Verhalten entfernt sind. Es ergibt sich eine Skalierung des Spinmoments mit der Größe der Bandlücke im Wirtscluster, was durch Austausch des Wirtsmaterials von Gold zu Kupfer bestätigt werden konnte.

Abstract

The electronic and magnetic properties of a single transition metal dopant (Sc, Ti, V, Cr) embedded in a finite gold host were studied. This was done by applying x-ray absorption and x-ray circular dichroism spectroscopy as well as density functional theory to size selected cationic gas phase clusters. The electronic structure of the impurity sensitively depends on the nature of the dopant as well as on quantum confinement in the host cluster and their interplay. An odd-even effect of electron localization in TiAu_n^+ clusters is foreshadowed in ScAu_n^+ clusters, whereas the local electronic structure in VAu_n^+ clusters is almost independent of the gold host size. However, for all investigated systems a strong tendency was found to delocalize an even number of electrons whenever allowed by the given boundary conditions.

The Anderson impurity model [1] describes the interaction of a single magnetic impurity with a homogenous free electron gas in a bulk sample. However, in case of a finite system the influence of an energy gap in the hosts density of states has to be accounted for. This was done within this thesis by studying the problem using a model Hamiltonian in tight binding approximation. Thus, it could be shown that the description of finite systems within the Anderson impurity model breaks down in principle. Especially the magnetic to non-magnetic transition threshold is predicted incorrectly. In addition it was shown that the spin polarization of an impurity atom is substantially stabilized by the presence of an energy gap in the host density of states. Still, the size dependence of the spin magnetic moment of chromium in almost fully spin polarized CrAu_n^+ clusters is essentially in agreement with the Anderson impurity model, since it is far from a magnetic to non-magnetic transition. Therefore, only a scaling of the spin magnetic moment of the impurity as a function of the energy gap could be observed, which was confirmed by substituting the host material from gold to copper.

Contents

1 Introduction **9**

2 Fundamentals **13**

2.1 Spectroscopic Methods 13

2.1.1 X-ray Absorption Spectroscopy 13

2.1.2 X-ray Magnetic Circular Dichroism Spectroscopy . . . 15

2.1.3 XMCD Sum Rules 16

2.1.4 Ion Yield Spectroscopy and Electronic Relaxation Processes 17

2.2 Correlated and Itinerant Electrons 18

2.3 Density Functional Theory 20

2.4 Self-Consistent Calculation of the On-site Coulomb Repulsion U in a DFT+U Framework . . 23

2.5 Anderson Impurity Model 25

2.6 Kondo Effect 27

3 Experimental Setup **31**

3.1 Magnetron Sputtering Cluster Source 31

3.2 Radio Frequency Ion Guide and Quadrupole Mass Filter . . . 32

3.3 Radio Frequency Ion Trap and Magnet 33

3.4 Reflectron Time-of-Flight Mass Spectrometer 35

3.5 Synchrotron Radiation and Undulator Beam-Lines 36

4 Experimental and Computational Details **39**

4.1 Data Acquisition 39

4.2 Data Analysis 42

4.3 Computational Details 43

5 Electronic Structure of Early $3d$ Transition Metal Impurities in Non-Magnetic Gold Clusters **45**

5.1 Local Electronic Structure of Scandium Doped Gold Clusters . . . 46
5.2 Odd-Even Effects in the Electronic Structure of Titanium Doped Gold Clusters . . . 49
5.3 Independence of the Local Electronic Structure on Impurity Coordination: Vanadium Doped Gold Clusters . . . 55
5.4 Local Electronic Structure of Chromium Doped Gold Clusters . . . 59
5.5 Summary . . . 61

6 The Anderson Impurity Model in Finite Systems 63
6.1 Testing the Anderson Impurity Model: A study of a Chromium Impurity in Gold-Clusters . . . 63
6.2 Modification of the Anderson Impurity Model for Finite Systems 71
6.3 Influence of the Host Material: Chromium Doped Copper Clusters . . . 76
  6.3.1 Geometries of Chromium Doped Copper Clusters . . . 76
  6.3.2 Electronic and Magnetic Properties of Chromium Doped Copper Clusters . . . 79
6.4 Summary . . . 84

7 Epilogue 85
7.1 Summary . . . 85
7.2 Outlook . . . 86

List of Publications 89

List of Figures 91

List of Tables 92

Bibliography 93

8 Appendix 109
8.1 Coordinates of CrCu_n^+ Clusters . . . 109

Acknowledgements 113

Chapter 1

Introduction

The interaction of localized impurity states with non-magnetic host materials is a long standing problem in solid state physics. It leads to complex many body phenomena such as Friedel oscillations [2, 3] or the Kondo effect [4], which is the at first sight counter-intuitive increase of the resistivity at low temperatures. The properties of magnetic impurities, such as transition metals or rare earths, in non-magnetic hosts have therefore been subject of intense research for the last 50 years. Especially the $3d$ transition metals are a particularly interesting class of material. Their valence electrons can neither be classified as fully localized nor as itinerant. This has significant consequences on their electronic and magnetic properties.

Considerable advances in studying the aforementioned many-body effects have been made by applying photoemission, x-ray magnetic circular dichroism (XMCD), and scanning tunneling spectroscopy to adatoms [5–8], clusters on surfaces [9], or well defined quantum dots [10, 11]. This allows to study and tune basic parameters such as the on-site Coulomb repulsion, which is the Coulomb interaction of electrons in the same localized orbital, or the coupling to the electron bath of the host. Up to now, such techniques have been applied to atomic scale systems only on surfaces or in bulk metals. In these systems one can study the interplay between impurity and host material by introducing different kinds of impurities or by varying the electronic density of the free electron gas, provided by the host material [5, 6]. In contrast, the study of single impurities in size-selected clusters allows to characterize the interaction with a finite electron gas, *i.e.*, with a well defined number of electrons occupying a highly discretized density of states. This approach will be followed in this thesis by using doped gold clusters (TMAu_n^+, $\mathrm{TM} = \mathrm{Sc}, \mathrm{Ti}, \mathrm{V}, \mathrm{Cr}$) as model systems that combine considerable local magnetic moments carried by the $3d$ electrons of the single dopant atom with a finite free electron gas formed by the host cluster. Isolated, doped gold clusters have been studied in great detail by density functional theory calculations [12–21] and experiment: their electronic and geometrical structure as well as their stability have been probed by photoelectron [21, 22], infrared photodissociation [23, 24], and laser photofragmentation [25–29] spectroscopy, as well as electron diffraction [30]. In this work the development of the dopant electronic and magnetic structure as a function of the host cluster size is studied by x-ray absorption and XMCD spectroscopy of size-selected gas phase clusters combined with density functional theory calculations. Applying these techniques paves the way to addressing elementary problems of solid state physics that call for the use of methods probing the local electronic and magnetic properties of an impurity rather than the global electronic structure of a system. Such problems are, *e.g.*, the question how the electronic structure of a finite non-magnetic host system and a single magnetic impurity are interrelated. Under which circumstances is the impurity's magnetic moment quenched and when does it survive? Can the size of the impurity's magnetic moment be understood based on bulk models? Furthermore, many-body effects, like the Kondo effect can be expected to change upon going from extended systems to systems containing only a few particles. In this sense, the present work can be regarded as a first step in observing a Kondo effect in finite systems.

This thesis is structured as follows: In chapter 2 next to x-ray absorption and XMCD spectroscopy, basic theoretical models and methods such as density functional theory and the Anderson impurity model are introduced. In chapters 3 and 4 experimental and computational details are given. Chapter 5 contains a discussion of the electronic structure of transition metal doped gold clusters. It is shown that the electronic structure sensitively depends on the nature of the dopant and quantum confinement in the host material as well as their interplay. Following the periodic table of elements, differences in the dopant-host interaction are discussed considering remarkably different behavior of ScAu_n^+, TiAu_n^+ and VAu_n^+ clusters. The experimental and theoretical findings additionally suggest a common ground in the binding mechanism. In chapter 6, a yet closer look will be given to the magnetic properties of chromium doped gold clusters. It will be shown that by shell closure in the two dimensional free electron gas of the gold host that governs the minimization of the impurity-host interaction, a nearly atomic spin magnetic moment of $5\,\mu_\mathrm{B}$ can survive in CrAu_2^+ and CrAu_6^+. A discussion of the size dependence of the spin magnetic moment in terms of the Anderson impurity model [1] reveals deeper insight into the interaction of the impurity atom with a highly discretized density of states. Therefore, the influence of the discrete nature of the host density of states was studied in tight binding approximation revealing a break down of the Anderson impurity model in the description of finite

systems. By exchanging the host material from gold to copper the dominance of the energy gap in the host density of states for the impurity's spin magnetic moment could be demonstrated.
Finally, concluding remarks can be found in chapter 7.

Chapter 2

Fundamentals

In this chapter an introduction into the spectroscopic as well as into basic theoretical methods will be given. In the first three subsections the benefits and limitations of x-ray absorption, x-ray magnetic dichroism and ion yield spectroscopy will be discussed. In the following sections theoretical approaches to treat the electronic structure will be introduced. Focus will be laid on the notoriously difficult correlated electron systems, by discussing density functional theory (DFT) and DFT+U methods and introducing the Anderson impurity model.

2.1 Spectroscopic Methods

2.1.1 X-ray Absorption Spectroscopy

An ensemble of atoms exposed to x-ray photons will attenuate the incoming photon beam according to the Lambert-Beer law

$$I(x, E) = I_0 \cdot e^{-\mu(E)\cdot x}. \tag{2.1}$$

Here x is the distance the light traveled in the medium and $\mu(E)$ is the absorption coefficient that depends linearly on the absorption cross section σ and the number of atoms n. At certain energies peaks can be found in the absorption that have their origin in dipole transitions with finite oscillator strength between core levels and unoccupied valence states. In x-ray absorption the energy of these transitions is characteristic since the core level binding energy strongly depends on the atomic number Z. This allows a local and element specific investigation even of compound systems. In addition to resonant transitions, photoemission of core electrons gives rise to the well known absorption edges. The absorption cross section above the continuum threshold decreases

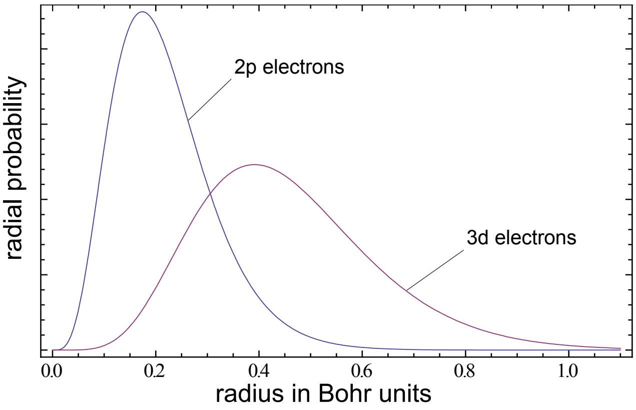

Figure 2.1: Radial probability of one-particle $2p$ and $3d$ wave functions shown for atomic number $Z = 23$.

monotonically since the overlap of continuum and core level wave functions drops with increasing energy.

The absorption signal I_{XAS} is determined by the transition probability which can be expressed by Fermi's Golden rule:

$$W_{fi} = \frac{2\pi}{\hbar} | \langle \phi_f | T | \phi_i \rangle |^2 \cdot \rho(E_f) \cdot \delta(E_f - E_i - \hbar\omega) \propto \sigma \propto I_{XAS}. \tag{2.2}$$

Here $\phi_{i,f}$ are the many-body initial and final state wave functions, respectively, T is the operator mediating the transition which in this case is the dipole operator[1] and $\rho(E)$ is the density of states. The delta function ensures the conservation of energy. The absorption process is often described in a single particle approximation, since the many body wave functions are usually unknown. Thus, equation 2.2 simplifies to

$$I_{XAS} = | \langle \phi_f | T | \phi_i \rangle |^2 \cdot \rho(E) \approx | \langle \phi_i \bar{c} \epsilon | T | \phi_i \rangle |^2 \cdot \rho(E) = | \langle c | T | \epsilon \rangle |^2 \cdot \rho(E) = M^2 \rho\left(E\right).$$

Here ϵ and c are the wave-functions of the excited electron and core hole, respectively. Since the matrix element M varies only very slowly with energy [31, 32], x-ray absorption in principal measures the density of states of the unoccupied energy levels.

This simple picture reaches its limit for the L-edge absorption of $3d$ transition metals. This is evident from the very complex multiplet structure in their x-ray absorption spectra [32, 33]. The comparable mean radii of $2p$ and $3d$ electrons, *cf.* figure 2.1, lead to a strong Coulomb interaction of the core hole created in the x-ray absorption process and the emitted photoelectron leading to the breakdown of the single particle approximation.

---

[1] In dipole approximation the explicit form of T is given by $T = \sum_q \mathbf{e_q} \cdot r$ (q direction of polarization, r position, $\mathbf{e}$ unit vector).

2.1.2 X-ray Magnetic Circular Dichroism Spectroscopy

The x-ray magnetic circular dichroism spectroscopy (XMCD) can be used to study the spin and orbital momentum resolved magnetic properties of a sample.

XMCD spectroscopy can be described in a two step model invented by Stöhr [35]. In a first step, a circular polarized photon transfers its angular momentum $\pm\hbar$ in an absorption process to the photoelectron. Assuming the photoelectron stems from a spin-orbit split $2p$ state[2] ($2p_{3/2}$ and $2p_{1/2}$) part of the angular momentum can be transferred to the spin degree of freedom via spin-orbit coupling. The spin polarization of the photoelectrons created in an absorption process is opposite for light with left and right helicity, respectively. Additionally, spin and orbital momentum are coupled parallel ($2p_{3/2}$) and anti parallel ($2p_{1/2}$) at the two absorption edges ($L_{2,3}$) leading to an inversion of photoelectron spin polarization for both helicities at the two edges ($L_{2,3}$). The transition probabilities are given by the transition matrix elements which are also displayed in figure 2.2.

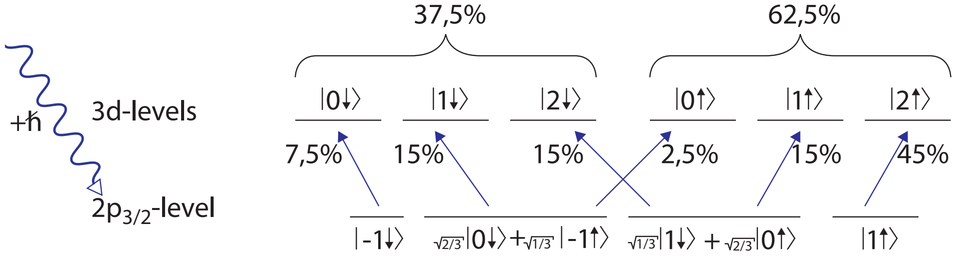

Figure 2.2: Excitation at the L_3-edge with a photon of positive helicity. The given probabilities for the individual transitions result from Clebsch-Gordon coefficients. The figure is adapted from [34].

In the second step the spin polarized photoelectron beam, created in the first step, is used to probe the spin polarization of the exchange split valence

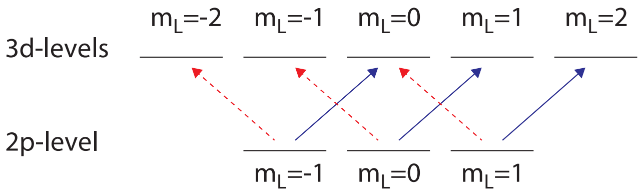

Figure 2.3: Shown are the accessible m_L subsets in a dipole transition for left (dotted line) and right (solid line) handed photons. The figure is adapted from [34].

---

[2] In reality, there is no spin-orbit splitting of the $2p$ levels in the initial state.

states resulting in different absorption cross sections for both helicities. Sensitivity to the orbital moment is given by the dipole selection rule $\Delta m = \pm 1$ for circular polarized light, as illustrated in figure 2.3. Since different m_L subsets are probed with left and right circular polarized light, an unequal occupation among these subsets leads to a dichroic absorption signal.

2.1.3 XMCD Sum Rules

Quantitative determination of the expectation value of orbital $\langle L_z \rangle$ and spin $\langle S_z \rangle$ moment along the quantization axis z necessitates the introduction of XMCD sum rules [36–38] relating them to the measured XMCD asymmetry. In a dipole transition $cl^n \rightarrow c^{-1}l^{n+1}$ between a core state with orbital momentum c and a valence state with orbital momentum l occupied by n electrons, the XMCD sum rules in their general form read[36, 37]

$$\frac{\int_{j_+ + j_-} (\tau^+ - \tau^-) dE}{\int_{j_+ + j_-} (\tau^+ + \tau^- + \tau^0) dE} = \frac{1}{2} \frac{l(l+1) + 2 - c(c+1)}{l(l+1)(4l + n - 2)} \langle L_z \rangle \tag{2.3}$$

and

$$\begin{aligned} \frac{\int_{j_+} (\tau^+ - \tau^-) dE - \frac{c+1}{c} \int_{j_-} (\tau^+ - \tau^-) dE}{\int_{j_+ + j_-} (\tau^+ + \tau^- + \tau^0) dE} &= \\ \frac{l(l+1) - 2 - c(c+1)}{3c(4l + 2 - n)} \langle S_z \rangle &+ \\ \frac{l(l+1)[l(l+1) + 2c(c+1) + 4] - 3(c-1)^2(c+2)^2}{6cl(l+1)(4l + 2 - n)} \langle T_z \rangle & \end{aligned} \tag{2.4}$$

Here $\tau^{+,-,0}$ are absorption spectra taken with helicity parallel and anti-parallel to the sample magnetization and linear polarized light. E is the energy. The core spin split states are denoted $j_{+,-} = c \pm 1/2$ respectively.

The magnetic dipole term $\langle T_z \rangle$ vanishes in our case due to angle averaging of the randomly oriented sample [39]. Thus the total magnetic moment μ_{total} is given by the sum of spin μ_S and orbital μ_L magnetic moment

$$\mu_{total} = \mu_S + \mu_L = 2n_h \frac{\mu_B}{\hbar} \langle S_z \rangle + n_h \frac{\mu_B}{\hbar} \langle L_z \rangle ,$$

μ_B being the Bohr magneton, $\hbar = h/2\pi$ the reduced Planck constant and n_h the number of vacancies in the $3d$ state.

The limitations of the applicability of XMCD sum rules are discussed in detail

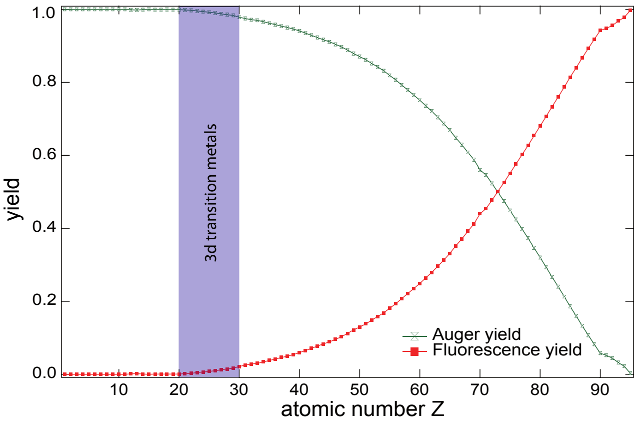

Figure 2.4: Comparison of fluorescence and Auger yield at the $L_{2,3}$ edges as a function of the atomic number Z taken from [46]. The Auger process is the dominant relaxation channel for the $3d$ transition metals.

in a series of papers [40–44]. Nonetheless, some of the assumptions involved in the derivation of the XMCD sum rules will be given here.

If the orbital angular momentum c of the core level differs from zero, transitions into valence states with orbital momentum $c \pm 1$ are allowed in a dipole transition. As can be seen from equations 2.3 and 2.4 the XMCD sum rules differ for the two transitions. Moreover, these transitions cannot be separated in an x-ray absorption experiment. However, since $2p \rightarrow 4s$ transitions contribute only up to 5 % to the $L_{2,3}$-edges absorption of $3d$ metals they can be neglected. This means that despite this first limitation, XMCD sum rules are still applicable.

In the derivation of the XMCD sum rules the initial and final states were restricted to be pure configurations. This cannot be expected at least for the highly excited final state. However, Thole *et al.* showed that the sum rules still hold in case of mixed configurations [36].

The spin XMCD sum rule implies the separation of j_+ and j_- states. In case of L-edge absorption of the $3d$ transition metals this is only satisfied if the $2p$ spin orbit splitting is larger than the $3d$ bandwidth. Obviously, the spin XMCD sum rule is inapplicable for the early and middle $3d$ transition metals because of the strong overlap of $2p_{3/2,1/2} \rightarrow 3d$ transitions. The break-down of the spin XMCD sum rule has already been shown for atomic manganese deposited on potassium [45].

2.1.4 Ion Yield Spectroscopy and Electronic Relaxation Processes

After x-ray absorption the cluster is highly excited and can in principle relax via radiative and non-radiative channels, namely fluorescence and Auger, Coster-Kronig or Super-Coster-Kronig processes. The fluorescence probability is given by the dipole matrix element $\langle c|r|v\rangle \propto E^3 \approx Z^6$ ($|c\rangle$ core state, $|v\rangle$ valence state), while the probability of the aforementioned non-radiative processes depend on the wave-function overlap. For a given pair of states the overlap does not vary strongly with the atomic number Z. Hence, which process is dominant strongly depends on the atomic number Z and the states involved. The fluorescence and Auger yield at the $L_{2,3}$-edges are shown in figure 2.4 indicating a negligible contribution of fluorescence to the total yield in case of $L_{2,3}$-edge absorption of $3d$ transition metals. Therefore electron or ion yield spectroscopy is the method of choice for the investigation of $3d$ transition metal L-edge absorption. Upon deposition of $500 - 900\,eV$ in the absorption process the system relaxes via Auger cascades leaving the cluster highly charged. If a critical charge at a given cluster size is exceeded, Coulomb repulsion will lead to fragmentation [47]. The yield of photofragments created in the absorption process is proportional to the cross section [48] and will here be used as the x-ray absorption signal.

2.2 Correlated and Itinerant Electrons

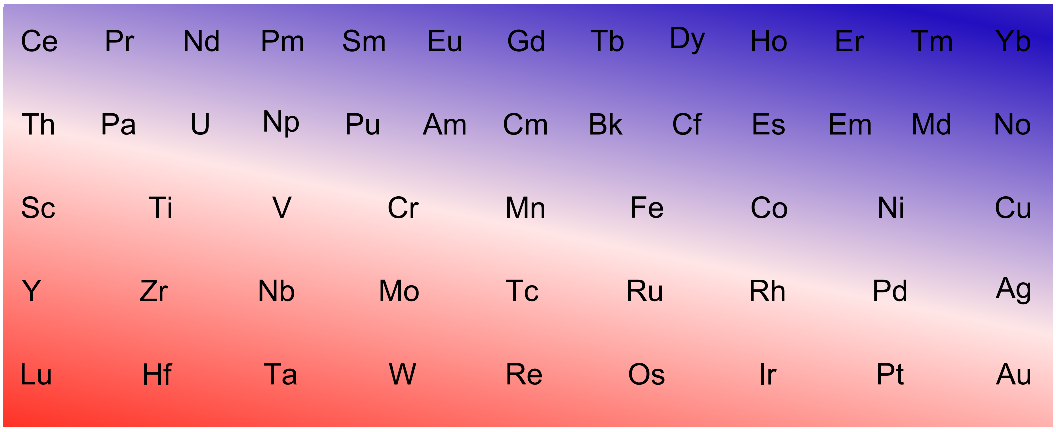

Ce	Pr	Nd	Pm	Sm	Eu	Gd	Tb	Dy	Ho	Er	Tm	Yb
Th	Pa	U	Np	Pu	Am	Cm	Bk	Cf	Es	Em	Md	No

Sc	Ti	V	Cr	Mn	Fe	Co	Ni	Cu
Y	Zr	Nb	Mo	Tc	Ru	Rh	Pd	Ag
Lu	Hf	Ta	W	Re	Os	Ir	Pt	Au

Figure 2.5: In the Kmetko-Smith diagram the periodic table is arrange by the localization of the valence orbitals. Since itinerant and correlated behavior is closely related to localization, magnetic metals with atomic-like valence orbitals can be found in the upper right (blue background color) whereas non-magnetic metals can be found in the lower left (red background color) corner of the diagram. The diagonal of the diagram is the cross-over region where itinerant and correlated behavior can be found simultaneously. The diagram is adapted from [49].

In the late 1920s and early 1930s Bloch [50] and Wilson [51] among others developed an one-electron theory for bulk materials. Within this theory non-interacting electrons move in the periodic charge background of the crystal as

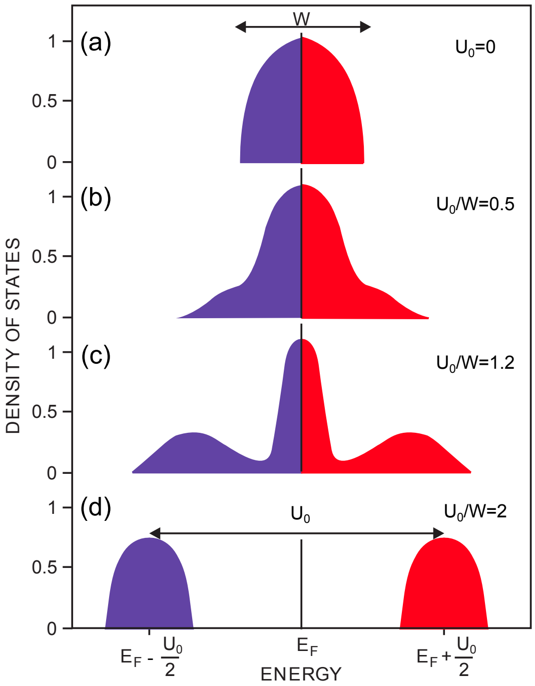

Figure 2.6: Mott transition: Density of states as a function of U_0/W adapted from [56]. (a) Non interacting Fermions forming a band of width W (b) Weakly interacting Fermions: A quasi-particle peak forms at E_F. The system can be well described within Fermi liquid theory. (c) Weakly correlated electronic systems: Coexistence of Hubbard bands and quasi-particle peak. (d) Strongly interacting electrons: Spectral density of the quasi-particle peak is completely transferred to the lower and upper Hubbard bands separated by the on-site Coulomb interaction U_0.

plane waves and occupy energy bands up to the Fermi energy, *cf.* figure 2.6 (a). Depending on the the location of the Fermi energy the material is a metal or an insulator. Electrons which are well described within this theory are called itinerant. However, it was quickly realized that this simple theory fails in describing transition metal compounds and rare earths. Hubbard [52, 53] and Mott [54] showed that the one-electron theory will fail if charge fluctuations are suppressed by large values of the on-site Coulomb interaction U_0, *cf.* section 2.4, as compared to the one-electron band width W. Since the mobility of electrons moving through the lattice is hindered by the Coulomb interaction with electrons occupying localized orbitals, these electrons are called correlated. If $U_0 \gg W$, the on-site Coulomb repulsion splits the valence band and result in a Mott-Hubbard insulator as was pointed out by Mott and Peierls in 1937 [55]. In between these two extremes two other regimes exist as depicted in figure 2.6 (b) and (c). If correlation is still small the interacting system can be described as an ensemble of non-interacting quasi-particles exhibiting some collective excitations. In case of comparable U_0 and W, Hubbard bands and quasi-particle peak coexist making the theoretical description very challenging.

The itinerant and correlated behavior of electrons is closely related to the degree of localization of the valence electrons. The valence electrons can be considered localized if their mean radius is small compared to inter-atomic distances in the material, thus the Coulomb interaction among electrons in

these orbitals is large. On the other hand, the valence orbitals overlap and form bands if their radius is comparable to equilibrium bond distances in the system. Then the electrons exhibit itinerant character.
By arranging the periodic table by localization of the valence orbitals, the Kmetko-Smith diagram [57] can be obtained which is shown in figure 2.5. In the upper right magnetic metals with atomic-like valence shells can be found whereas in the lower left corner non-magnetic metals are located. The crossover regime is the diagonal of the diagram where valence electrons exhibit itinerant as well as correlated behavior, *cf.* figure 2.6. Correlated materials exhibit a wealth of interesting phenomena such as high temperature superconductivity [58], giant magneto resistance [59, 60], large effective electron mass (heavy fermions) [61] and many more [62]. Doubtless, the diagram shown in figure 2.5 is oversimplified and does not reflect the whole complexity of the physics in bulk materials. Yet, the point I want to emphasize is that the systems which will be investigated throughout this thesis consist of elements very close to the diagonal of the Kmetko-Smith diagram and thus are expected to exhibit itinerant as well as localized behavior.

2.3 Density Functional Theory

In quantum physics a system is solely described by its wave function Ψ, which can in principle be calculated by solving the Schrödinger equation. In Born-Oppenheimer approximation the Schrödinger equation for a non-relativistic Coulombic system consisting of N electrons at positions $\mathbf{r}_i$ and with spin χ_i and M ionic cores is given by [3]:

$$\begin{aligned}\left(T + V + \tilde{V}\right) \Psi\left(\mathbf{r}_1, \mathbf{r}_2, \ldots, \mathbf{r}_N, \chi_1, \chi_2, \ldots, \chi_N\right) \\ = E\, \Psi\left(\mathbf{r}_1, \mathbf{r}_2, \ldots, \mathbf{r}_N, \chi_1, \chi_2, \ldots, \chi_N\right).\end{aligned} \tag{2.5}$$

Here T is the N-particle kinetic energy

$$T = \sum_{i=1}^{N} -\frac{\hbar^2}{2m} \nabla_i^2. \tag{2.6}$$

The Coulomb interaction of M ionic cores at positions $\mathbf{R}_k$ possessing a nuclear charge Z_k and N electrons is described by the external potential

$$V = \sum_{i,k=1}^{N,M} \frac{Z_k e^2}{|\mathbf{r}_i - \mathbf{R}_k|}. \tag{2.7}$$

---

[3] Here I use the convention: $\frac{1}{4\pi\epsilon_0} = 1$

The most intriguing contribution to the total energy is the electron-electron interaction

$$\tilde{V} = \sum_{i,i'=1\, i\neq i'}^{N} \frac{e^2}{|\mathbf{r}_i - \mathbf{r}_{i'}|}. \tag{2.8}$$

Here arises the main challenge in atomic and condensed matter physics. The many-body wave-function Ψ depends on $3N$ spatial and N spin coordinates. Since $\tilde{V}$ couples the spatial coordinates they cannot be treated separately. Therefore, solving the Schrödinger equation for a many-electron system is not only very difficult and computationally demanding, but also exceeds storage space available today even for small systems.

Tackling the many-body problem without directly involving the many-body wave-function Ψ is at the heart of density functional theory (DFT). Only a short introduction to DFT will be given here, detailed information can be found in excellent review articles [63, 64] or monographs [65–68].

In 1964 *Hohenberg and Kohn* proved that there is a bijective mapping of the ground state many-body wave-function Ψ and electron density $n(\mathbf{r})$ [69]. Consequently, the expectation value of every observable and therefore in particular the ground state energy can be expressed as a functional of the density $n(\mathbf{r})$:

$$E\left[n\right] = \langle \Psi\left[n\right] | \mathcal{H} | \Psi\left[n\right] \rangle = \int V(\mathbf{r}) n(\mathbf{r}) d^3\mathbf{r} + F\left[n\right]. \tag{2.9}$$

By construction the functional $F\left[n\right] = T\left[n\right] + \tilde{V}\left[n\right]$ is universal, *i.e.*, not explicitly depending on the external potential V. The Hohenberg-Kohn theorem proves that the density $n(\mathbf{r})$ can be used as the basic variable reducing the many-body problem tremendously. The functional 2.9 exhibits a minimum for the ground state density under the constraint $\int n(\mathbf{r})d^3\mathbf{r} = N$:

$$E_0\left[n\right] = min_{n(\mathbf{r})} E[n]. \tag{2.10}$$

Thus the variational principle can be stated as:

$$\delta \left\{ E[n] - \mu \left(\int n(\mathbf{r}) d^3\mathbf{r} - N \right) \right\} = 0, \tag{2.11}$$

where the Lagrangian multiplier μ takes care of the constraint of constant particle number N.

In practical calculation the functional $E[n]$ will be expressed as

$$E[n] = T_s[n] + \int V(\mathbf{r}) n(\mathbf{r}) d^3\mathbf{r} + E_{Hartree}[n] + E_{xc}[n], \tag{2.12}$$

as proposed by Kohn and Sham [70]. The functional $T_s[n]$ is the kinetic energy functional of non-interacting electrons and $E_{Hartree}$ the classical Coulomb interaction of two charge distributions:

$$E_{Hartree}[n] = \frac{e^2}{2}\int\int \frac{n\left(\mathbf{r}\right)n\left(\mathbf{r}^{'}\right)}{\left|\mathbf{r}-\mathbf{r}^{'}\right|}d^3\mathbf{r}d^3\mathbf{r}^{'}. \tag{2.13}$$

The functional $E_{xc}[n]$ collects all the dynamical and static exchange and correlation effects and can by definition be expressed as:

$$E_{xc}[n] = F[n] - T_s[n] - E_{Hartree}[n]. \tag{2.14}$$

Application of the variational principal yields

$$\frac{\delta T_s[n]}{\delta n\left(\mathbf{r}\right)} + V_{KS} = \mu, \tag{2.15}$$

V_{KS} being an effective potential, which is called Kohn-Sham potential

$$V_{KS} = V(\mathbf{r}) + \frac{e^2}{2}\int \frac{n\left(\mathbf{r}^{'}\right)}{\left|\mathbf{r}-\mathbf{r}^{'}\right|}d^3\mathbf{r}^{'} + \frac{\delta E_{xc}[n]}{\delta n(\mathbf{r})}. \tag{2.16}$$

Equation 2.15 describes an auxiliary system of non-interacting particles moving in an effective potential V_{KS}. The Schrödinger equation

$$\left(-\frac{\hbar^2}{2m}\nabla^2 + V_{KS}(\mathbf{r})\right)\phi_i = \epsilon_i\phi_i \tag{2.17}$$

of this auxiliary system yields single particle wave-functions ϕ_i that reproduce the density $n(\mathbf{r})$ of the original system

$$n(\mathbf{r}) = \sum_i^{occ}|\phi_i|^2. \tag{2.18}$$

Equations 2.16-2.18 are known as the Kohn-Sham equations and have to be solved self-consistently. Solving the Kohn-Sham equations would yield the correct ground state density, were it not for the exchange-correlation functional $E_{xc}\left[n\right]$, which is in general not known exactly, but has to be approximated. Several approximations were introduced for $E_{xc}[n]$, the most common are the local density approximation (LDA) and the generalized gradient approximation (GGA). These approximations yield accurate descriptions of a wealth of systems. However, they fail in describing even very fundamental properties of strongly correlated electronic systems. Notorious examples are the transition metal oxides FeO an CoO for which they fail to reproduce the antiferromagnetic ground states, as well as the band gaps predicted for MnO and NiO [73–

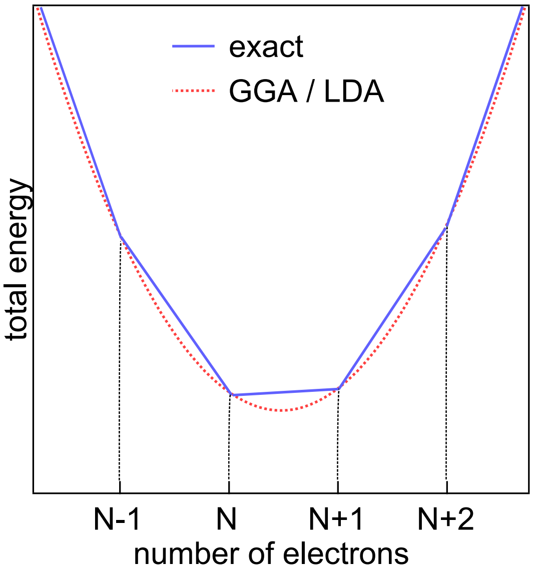

Figure 2.7: Schematic illustration of the total energy as a function of occupation numbers. The exact functional exhibits derivative discontinuities at integer electron numbers [71]. The GGA and LDA approximations underestimate the total energy for fractional occupations. This can partly be compensated by introducing an additional Hubbard term to the XC functional [72].

75]. Many problems that standard approximations to $E_{xc}[n]$, such as LDA or GGA, have, can be overcome by correcting for the well known, spurious self-interaction error that plagues most commonly employed xc-functionals. However, most self-interaction corrected methods [76] are computationally very demanding. Alternatively, semiempirical modifications of LDA and GGA, like DFT+U method can be employed. This will be described in the next section.

2.4 Self-Consistent Calculation of the On-site Coulomb Repulsion U in a DFT+U Framework

The introduction of an Hubbard like energy U, which is the Coulomb repulsion among localized electrons, to the exchange-correlation functional [77–79] constitutes a semi-empirical method to compensate for the self interaction error inherent in the highly localized $3d$ and $4f$ orbitals of transition metals, *cf.* figure 2.7. In general it is implemented in the following way:

$$E_U = \frac{U}{2} \sum_{l,\chi} Tr \left[\mathbf{n}_{l,\chi}(1 - \mathbf{n}_{l,\chi}) \right] . \tag{2.19}$$

The electrostatic Coulomb energy U is the energy necessary to add an additional electron with opposite spin to a localized orbital. The matrix $\mathbf{n}_{l,\chi}$ gives the occupation of the localized orbitals at site l with spin χ. The energy U

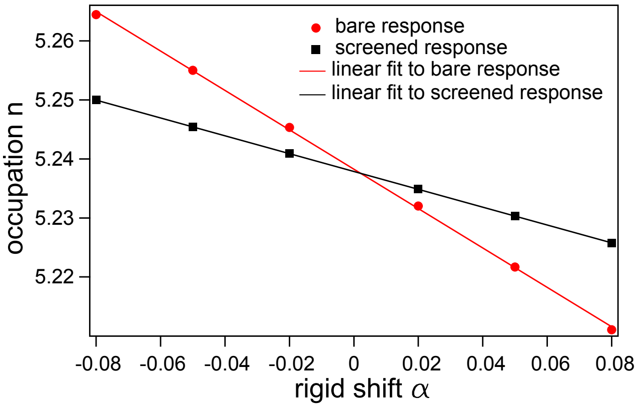

Figure 2.8: Linear response function for the screened and bare system. The rigid potential shifts $\Delta V = \sum_l \alpha_l P^l$ induce a change in occupation n. The difference of the slopes gives the onsite Coulomb repulsion U.

depends on the system and is normally fitted to experimental data, strongly limiting the predictive power of such a theory. Hence, it is highly desirable to calculate the energy U from first principles. This is non-trivial, since the direct Coulomb interaction is partially screened by delocalized electrons. Therefore simply calculating the respective Coulomb integral will fail.
Several approaches are proposed in the literature [72, 77, 80–85], here I stick to the linear response method introduced by Cococcioni *et al.* [72, 84, 85]. The approach starts by calculating the total energy as a function of the occupation of the localized orbitals

$$E\left[\{q_l\}\right] = min_{n(\mathbf{r}),\alpha_l}\left\{E[n(\mathbf{r}) + \sum_l \alpha_l(n_l - q_l)]\right\}. \tag{2.20}$$

The constraints on the site occupations n_l are taken care of by the Lagrangian multipliers α_l. The curvature of the above function contains in principle the fully screened on-site Coulomb repulsion. However, additionally change of the occupation induces re-hybridization effects that are even present in non-interacting system. These effects yield non-vanishing contributions to the curvature of the energy $E^{KS}\left[\{q_l\}\right]$ and therefore have to be subtracted. Thus the on-site Coulomb repulsion U is given by

$$U = \frac{\partial^2 E\left[\{q_l\}\right]}{\partial q_l^2} - \frac{\partial^2 E^{KS}\left[\{q_l\}\right]}{\partial q_l^2}. \tag{2.21}$$

Equation 2.21 can be recasted [72] applying a Legendre transform as

$$U = \frac{\partial \alpha_l^{KS}}{\partial q_l} - \frac{\partial \alpha_l}{\partial q_l} = \left(\beta_0^{-1} - \beta^{-1}\right), \tag{2.22}$$

where β_0 and β are the density response functions:

$$\beta^0_{lm} = \frac{\partial^2 E^{KS}}{\partial\alpha_l \partial\alpha_m} = \frac{\partial n_l}{\partial\alpha^{KS}_m} \tag{2.23}$$

$$\beta_{lm} = \frac{\partial^2 E}{\partial\alpha_l \partial\alpha_m} = \frac{\partial n_l}{\partial\alpha_m} \tag{2.24}$$

The α_l induce a rigid potential shift $\Delta V = \sum_l \alpha_l P^l$ (P^l are generalized projectors onto localized orbitals) at the localized orbitals, leading to a change of occupation. An example calculation, performed within the QUANTUM ESPRESSO 5.0 code [86], is shown in figure 2.8. The difference of both slopes gives the on-site Coulomb repulsion U self-consistently.

2.5 Anderson Impurity Model

The Anderson impurity model [1, 61] was introduced to describe the interaction of a single magnetic impurity embedded in a non magnetic host material based on a simple model Hamiltonian given in second quantization as

$$\mathcal{H} = \mathcal{H}_{\mathbf{k}} + \mathcal{H}_d + \mathcal{H}_U + \mathcal{H}_{\mathbf{k}d}. \tag{2.25}$$

The energy of the free electron gas of the non magnetic host is given by

$$\mathcal{H}_{\mathbf{k}} = \sum_{\mathbf{k},\chi} \epsilon_{\mathbf{k}} c^\dagger_{\mathbf{k},\chi} c_{\mathbf{k},\chi} = \sum_{\mathbf{k},\chi} \epsilon_{\mathbf{k}} n_{\mathbf{k},\chi}, \tag{2.26}$$

where $c_{k,\chi}$ and $c^\dagger_{k,\chi}$ are the annihilation and creation operators. The energy of the unperturbed localized levels of the magnetic impurity is given by

$$\mathcal{H}_d = E\, c^\dagger_d c_d = E\, n_d, \tag{2.27}$$

while the unscreened on-site Coulomb repulsion U_0 among localized electrons in the same orbital is treated as

$$\mathcal{H}_U = U_0 n_{d,\uparrow} n_{d,\downarrow}. \tag{2.28}$$

The last term in equation 2.25 describes the interaction of the localized states with the free electron gas

$$\mathcal{H}_{\mathbf{k}d} = \sum_{\mathbf{k},\chi} V_{dk} \left(c^\dagger_{\mathbf{k},\chi} c_{d,\chi} + c^\dagger_{d,\chi} c_{\mathbf{k},\chi} \right), \tag{2.29}$$

by introducing a hybridization matrix V_{dk}.

A schematic illustration of the Anderson model is shown in figure 2.9 as-

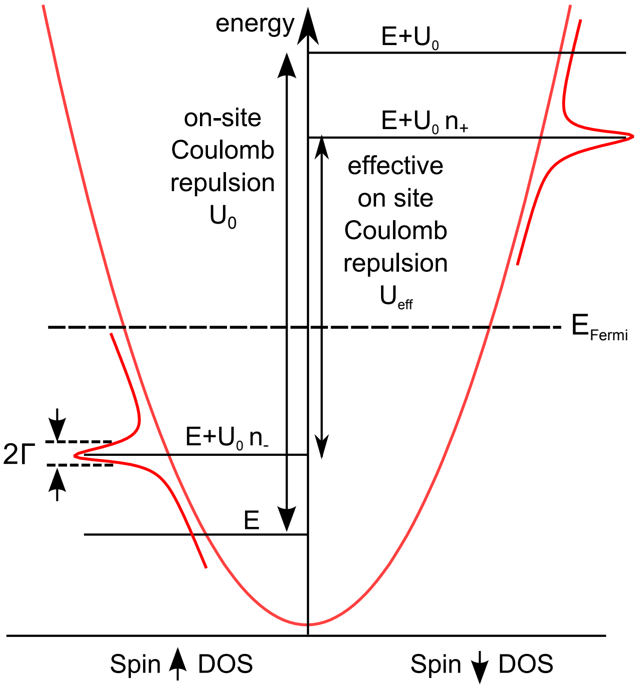

Figure 2.9: Schematic illustration of the Anderson impurity model for the magnetic case and maximal spin polarization $U_0 \gg \Gamma$ [1]. Two electrons in the same localized state are separated by the energy U_0. Hybridization with the parabolic density of states of the non-magnetic host causes a broadening 2Γ of the localized states and reduction of U_0 to an effective value U_{eff}. The system becomes non-magnetic if $U_{\text{eff}} \approx \Gamma$.

suming the simple case of a single non-degenerate impurity state. If in a first step hybridization of the localized orbitals with host electron gas states is neglected, adding an electron to a localized level $\phi_d(\mathbf{r})$ results in a state at energy $E + U_0$, U_0 being the on-site Coulomb repulsion among the localized electrons. The sample becomes magnetic if U_0 pushes the state $E + U_0$ above the Fermi level E_F.

However, in real systems interaction will be present resulting in virtual bound states at energies $E + U_0 \cdot n_-$ and $E + U_0 \cdot n_+$, *cf.* figure 2.9. Here, $n_\pm$ are the occupation numbers of the single impurity majority and minority spin levels. Hybridization of the localized orbitals with the host electronic states yield a considerable broadening 2Γ of the localized state. This in turn can lead to a reduction of the spin polarization $(n_+ - n_-)$, since a certain amount of the Lorentzian shaped density of states $\rho\,(E_d)$ of the localized spin up orbital is smeared above and in case of the spin down orbital below the Fermi energy. This reduces the energetic separation U_{eff} of the virtual states to $U_{\text{eff}} = U_0\,(n_+ - n_-)$.

Whether the system is magnetic or non-magnetic sensitively depends on the ratio of U_0 and Γ. A transition between these two states is predicted by the Anderson model at a ratio of U_0 and Γ which is equal π, if we assume a symmetrical arrangement of the impurity levels around the Fermi energy [1]. In figure 2.10, the occupation numbers of the majority and minority impurity

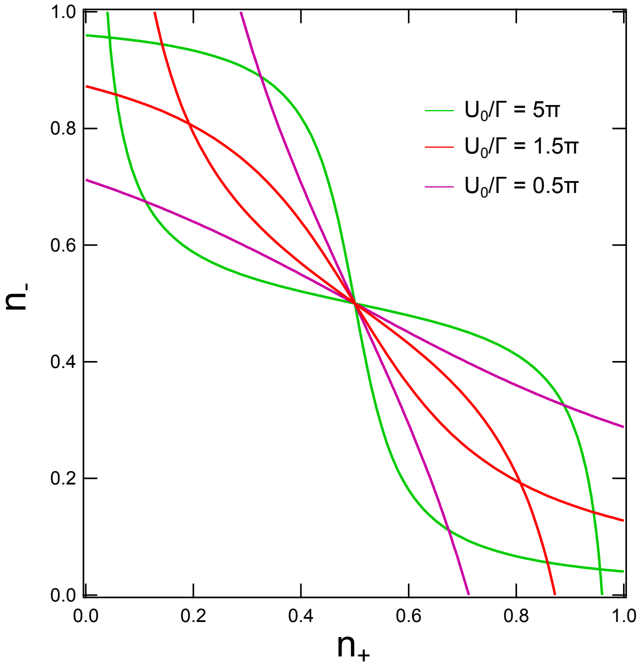

Figure 2.10: Occupation numbers for majority and minority impurity spin levels. Self consistent solutions can be found at the intersections of the curves. Spin polarization can only be found for values $U_0/\Gamma > \pi$, whereas the system is non magnetic for $U_0/\Gamma = 0.5\pi$.

spin levels is plotted versus each other for three different values of U_0/Γ. Stable solutions can be found at the intersections. As can be seen in the figure only for the cases where U_0/Γ is larger than π spin polarized solutions can be found, whereas for the value of $U_0/\Gamma = 0.5\pi$ the system is non-magnetic.

To further clarify the nature of the virtual bound states, the situation has to be explained in the framework of a scattering process [2, 3, 87]. The unfilled d and f orbitals of transition metals and rare earths exhibit a large centrifugal barrier and are therefore trapped or localized at the impurity site. Still the barrier is not attractive enough to form a real bound state. If the impurity states lie within the conduction band of the host material, free electrons with momentum $\mathbf{k}$ can resonantly scatter at the impurity potential and form a sharp resonance. Thus, the free conduction electrons can tunnel through the centrifugal barrier to the impurity state, reside there for a long but finite time and in the end tunnel back into the conduction sea of electrons with a momentum $\mathbf{k}'$. Since the electron stays only a finite time at the impurity site, the impurity state is called a virtual bound state.

2.6 Kondo Effect

Since the Anderson impurity model is closely related to the Kondo model and furthermore the present study is a first step towards the investigation of a

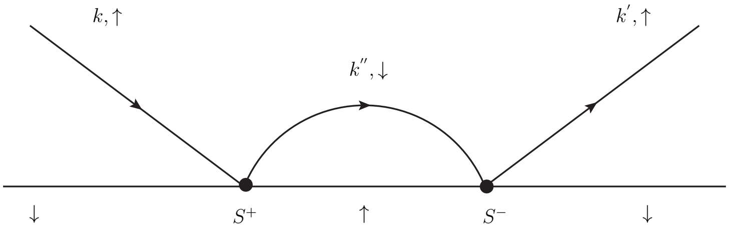

Figure 2.11: Second order scattering process leading to the Kondo effect: A conduction electron in state $\mathbf{k}, \uparrow$ scatters at the magnetic impurity with spin $\downarrow$ under spin flip transition into the intermediate state $\mathbf{k}'', \downarrow$ and impurity spin $\uparrow$. A second scattering process leads to the final state $\mathbf{k}', \uparrow$ and impurity spin $\downarrow$.

Kondo effect in finite systems, the Kondo effect will be briefly discussed here. For a detailed description I refer the reader to the original work and excellent reviews on the subject [4, 61, 88].

The Kondo effect describes transport anomalies, like an increase in resistivity at low temperatures found in non-magnetic metals sparsely doped with magnetic impurities, first observed in 1934 by de Haas *et al.* in FeAu [89]. Hence, there has to be an additional contribution to the scattering of conduction electrons beyond electron-phonon and defect scattering, which increases the resistivity at low temperatures.

In case of small hybridization strength V_{dk} and large U_0, *i.e.* the local moment regime, the Anderson model can be transformed by the use of the Schrieffer-Wolff transformation [90] to the *sd*-model Hamiltonian [61], which has the form

$$\mathcal{H}_{sd} = \sum_{\mathbf{k},\mathbf{k}'} J_{\mathbf{k},\mathbf{k}'} \left(S^+ c^\dagger_{\mathbf{k},\downarrow} c_{\mathbf{k}',\uparrow} + S^- c^\dagger_{\mathbf{k},\uparrow} c_{\mathbf{k}',\downarrow} + S_z \left(c^\dagger_{\mathbf{k},\uparrow} c_{\mathbf{k}',\uparrow} - c^\dagger_{\mathbf{k},\downarrow} c_{\mathbf{k}',\downarrow} \right) \right). \quad (2.30)$$

The spin ladder operators are defined as $S^\pm = S_x \pm iS_y$ and $J_{\mathbf{k},\mathbf{k}'}$ is the exchange coupling.

Allowing only low energy excitations $\mathbf{k}, \mathbf{k}' \approx \mathbf{k_F}$ in the system, *i.e.* particularly forbid excitations into the upper local moment state, the exchange coupling can be expressed as follows [90]:

$$J_{\mathbf{k_F},\mathbf{k_F}} = J_0 = |V_{dk_F}|^2 \frac{U_0}{E_d \left(E_d + U_0 \right)} < 0.$$

Since J_0 is negative, conduction electron and local impurity spin couple antiferromagnetically. The formation of this singlet state was first described by Kondo [4]. This formation of a singlet state in the low energy regime can be understood as a higher order scattering processes as depicted in the Feynman diagram in figure 2.11. The scattering process involves a spin flip of the impurity and conduction electron. An incoming electron $\mathbf{k}, \uparrow$ is scattered under spin flip into an intermediate state $\mathbf{k}^{''}, \downarrow$. Another spin flip scattering leads to the final state of electron $\mathbf{k}^{'}, \uparrow$.

Perturbation theory in third order of the exchange coupling J_0 of the localized spin and the spin of itinerant electrons treating this spin flip scattering process [4], yields a contribution to the resistivity of the form $\ln(T/T_K)$. The temperature T_K is the Kondo temperature which defines the energy scale for the singlet formation. This leads to the anomalous resistivity increase at low temperatures as observed experimentally.

It should be mentioned that the transition to the Kondo regime as a function of temperature is not a phase transition but a continuous cross over, since the cloud of conduction electrons screening the local impurity spin grows as the temperature decreases.

Chapter 3

Experimental Setup

The following chapter will give an overview of the experimental techniques applied. The data presented throughout this thesis was taken using two different setups. Since a detailed description of the setup used to obtain linear x-ray absorption spectra, which was designed by me, can be found in the literature [48, 91], focus will be brought to the second setup enabling us to perform XMCD spectroscopy on mass selected clusters. This setup, a modification of the first one, was designed by Andreas Langenberg [92] and is shown in figure 3.1. Clusters were produced in a magnetron gas aggregation source and transmitted with an adjacent radio frequency ion guide to a quadrupole mass filter. Transfer of the mass selected cluster beam into a radio frequency ion trap situated in a high field magnet is accomplished by high transmission ion optics. The low target density of a gas phase sample and the low absorption cross sections for inner shell excitations are overcompensated by using an ion trap and intense synchrotron radiation. Detection of the ion yield, resulting from inner shell excitation, is achieved by time-of-flight mass spectrometry. All inner shell spectra were taken at the synchrotron radiation facility BESSY II, currently operated by the Helmholtz association. A short introduction to synchrotron radiation is given in section 3.5.

3.1 Magnetron Sputtering Cluster Source

Clusters were produced in a standard magnetron gas aggregation source developed in the *Haberland/von Issendorff* group. Production of binary clusters is achieved by co-sputtering of two metal targets by introducing 4 mm drillings on a reference circle of 27 mm radius in the upper target, which is normally the host material. The size of the drillings depend on the ratio of the sputter yields of both metals and the desired amount of doping. High purity argon

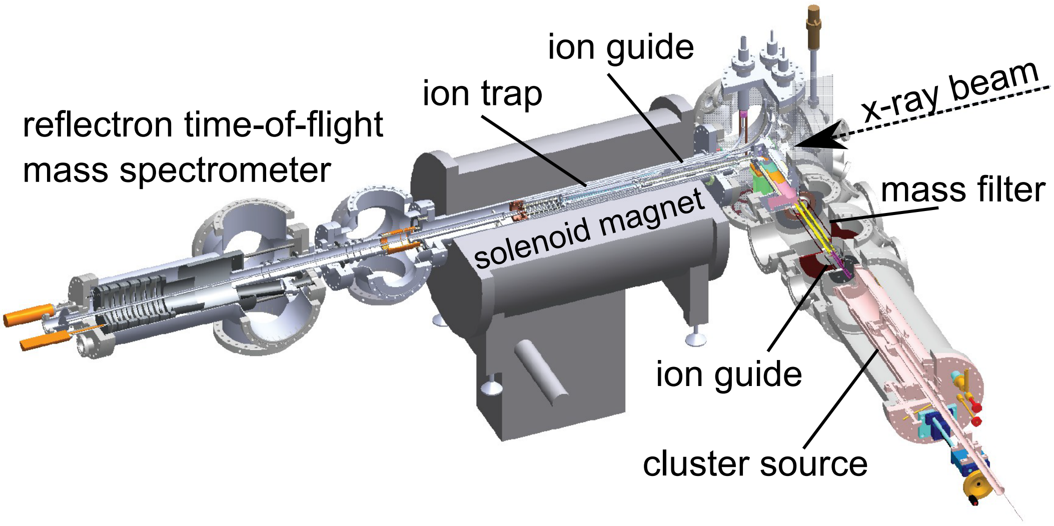

Figure 3.1: Schematic view of the setup for XMCD spectroscopy on free mass selected clusters [34]. Clusters were produced in a magnetron gas aggregation source and subsequently mass selected in a quadrupole mass filter. The mass selected cluster beam is transferred by several ion optics into a quadrupole ion trap cooled to liquid He temperature and situated in a 5T solenoid superconducting magnet. Synchrotron radiation is coupled in co-axially to the trap axis. Ion yield spectroscopy is performed using a reflectron time-of-flight spectrometer.

is used for sputtering, the plasma discharge is stabilized by a magnetic field. Clusters grow by aggregation in a helium atmosphere. The aggregation volume is cooled to liquid nitrogen temperature. Since cooling conditions are very mild in the aggregation process, preferentially ground state structures are formed.

By adjusting the argon and helium flow, the aggregation length and the pressure as well as the sputtering power, the size distribution of the clusters can be shifted in a wide range, from monomers up to clusters containing several hundreds of atoms. For a very detailed description of the source I refer the reader to references [48, 93].

3.2 Radio Frequency Ion Guide and Quadrupole Mass Filter

Adjacent to the cluster source a radio frequency ion guide is mounted, transmitting the cluster beam to a quadrupole mass filter, through a differential pumping stage. Mass selection is then performed in a commercial quadrupole

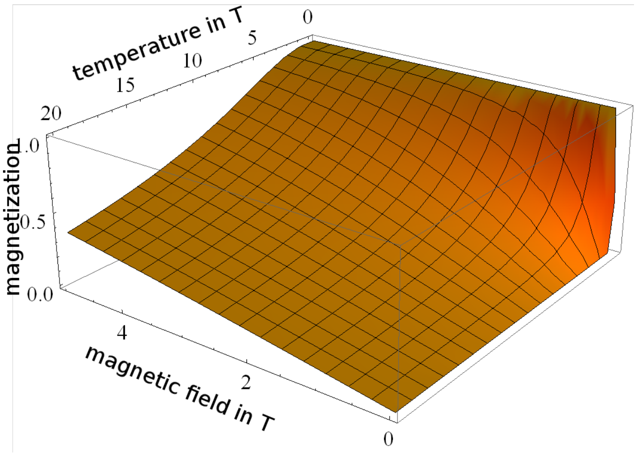

Figure 3.2: Magnetization as a function of temperature and external magnetic field shown for a particle with $J = S = 5/2$. Magnetization follows the Brillouin function. At a typical temperature of about 15 K and a maximum magnetic field of 5 T magnetization is about 45 %.

mass filter [1] featuring high transmission at a resolution of up to $m/\Delta m = 1200$. Typical currents of the mass selected cluster beam are $10 - 100$ pA. The divergent mass selected cluster beam is focused by an ion lens. Additionally, an electric field transverse to the cluster propagation direction can be applied to correct the ion trajectories in the stray field of the high field magnet. Subsequently the cluster beam is bended by a 90 ° static quadrupole deflector. The cluster beam is transmitted to the ion trap situated in the homogeneous part of the magnetic field by a quadrupole ion guide. By collisions with residual gas the cluster beam is compressed to the ion guide axis before entering the magnetic field, which forces the ions to precess. Therefore a maximum overlap of cluster ion and synchrotron radiation beam is ensured. Details can be found in the master thesis of *M. Niemeyer* [34] and reference [39].

3.3 Radio Frequency Ion Trap and Magnet

The low cross section of the inner shell absorption and a dilute gas phase sample necessitate the accumulation of target density in an ion trap in order to perform XAS and XMCD spectroscopy [48]. Since the basic principles of the operating mode of the ion trap are discussed thoroughly in the literature [34, 48, 91, 94] a detailed description will not be given here. Instead technical details affecting the magnetization of the sample will be brought into focus.

As an example the magnetization of particles with a magnetic moment of $5\,\mu_\mathrm{B}$ as a function of the external magnetic field and the temperature is shown in figure 3.2. In this example a magnetization of about 45 % is obtained in a

---

[1] Extrel QMS equipped with 9.5 mm electrodes and operated at a frequency of 880 kHz. A mass range of $10\,^{\mathrm{amu}}/_{\mathrm{e}}$ up to $4000\,^{\mathrm{amu}}/_{\mathrm{e}}$ is accessible.

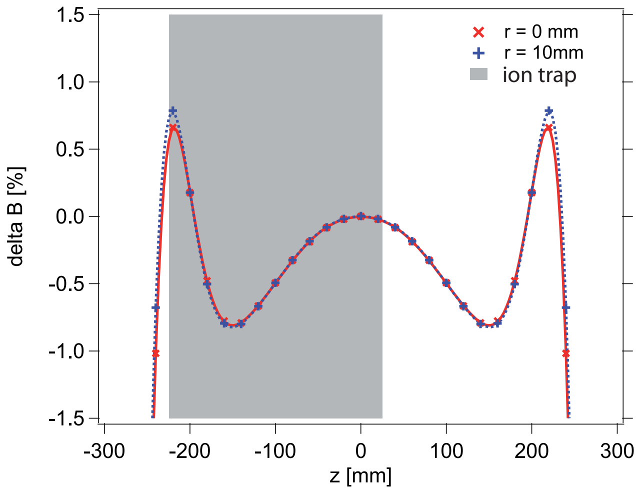

Figure 3.3: Variation of the magnetic field at 5 T along the magnets symmetry axis [95]. The trap is aligned so that the magnetic field variation is less than 1 %, as shown by the solid line (magnetic field on axis) and the dotted line (magnetic field 10 mm off axis).

5 T magnetic field and at a typical operating temperature of 15 K. To achieve magnetization of the sample, the trap is placed in the homogeneous part of the magnetic field of a solenoid superconducting magnet and cooling of the sample is accomplished by using a helium buffer gas coupled to a liquid helium reservoir. The variation of the magnetic field along the magnet axis is shown in figure 3.3. As can be seen the trap is not placed in the center of the magnet, but in an area where the magnetic field varies less than 1%. The trap is moved as close as possible to the focus of the x-ray beam, which is only limited by the presence of a vacuum chamber hosting the static deflector and several supply feedthroughs for the experiment, *cf.* figure 3.1.

The design of the liquid helium reservoir is shown in figure 3.4. The radio frequency (rf) and direct current (dc) electrodes are coupled to a double walled tube containing the liquid helium. This tube is shielded against infrared radiation by a second double walled tube cooled to liquid nitrogen temperature, which is thermally isolated by ceramic spacers against the inner liquid helium tube and the vacuum chamber. As already mentioned cooling of the gas phase sample itself is achieved by a helium buffer gas. The temperature was controlled using two temperature sensors[2] mounted on the helium reservoir and the dc electrodes, respectively. However, the temperature reading of the probes can in principle deviate from the true cluster temperature due to rf heating and imperfect coupling to the helium reservoir. For that reason the probes were calibrated by taking magnetization curves of large iron clusters, which was shown in detail in [34, 39]. To obtain temperatures T as low as $T = 10 - 20\,\mathrm{K}$ a partial pressure of about $10^{-4} - 10^{-3}\,\mathrm{mbar}$ is required [93,

---

[2] Cernox sensor, model: CX-1050-SD-HT-1.4L-SMOD-4-QT36-4

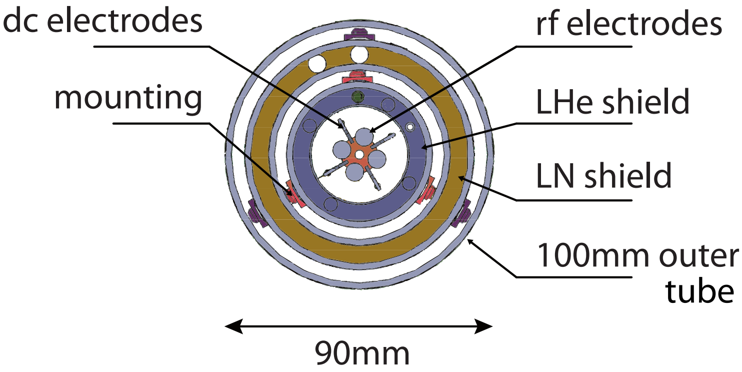

Figure 3.4: Sectional view of the ion trap [34]. The rf electrodes confine the clusters radially. The dc electrodes create a electric field pushing the clusters towards the exit aperture. Cooling is achieved by a helium buffer gas coupled to the liquid helium reservoir, which is shielded against infrared radiation by a liquid nitrogen cooling shield.

96] inside the ion trap.

During x-ray absorption measurements a considerable number of helium atoms is ionized, although the cross section of direct photoionization is rather small at the transition metal L-edge photon energies. This is overcompensated by the high partial pressure present in the trap. The helium ions, that are trapped very efficiently by the magnetic field, suppress the cluster density and furthermore spark discharges in the trap's electric fields. Therefore, an additional dipole rf field is applied to the trap's electrodes tuned to the cyclotron resonance $\omega_{cyclotron} = e \cdot B/2m$ of helium at the given magnetic field strength. In this way helium ions can efficiently be removed from the trap.

3.4 Reflectron Time-of-Flight Mass Spectrometer

Ion yield spectra were recorded using a modified reflectron time-of-flight mass spectrometer. In a pulsed electric field particles of different masses gain the same amount of energy. The mono-energetic particles spatially disperse in a field free region according to their mass-to-charge ratio. Hence, by measuring the time of flight, ion yield spectra can be obtained.

The initial space and velocity distribution of the particles was corrected by using two acceleration stages and a reflector. This standard reflectron time-of-flight mass spectrometer [97–99] was modified by three additional einzel-lenses that adjust the ion trajectories which are disturbed by the stray field of the high field magnet.

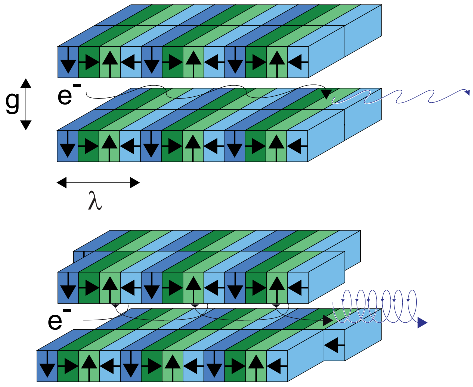

Figure 3.5: Sketch of an undulator and electron bunch trajectories taken from [34]. Light emitted by the electrons within the undulator can interfere constructively enhancing the synchrotron radiation intensity. By tuning the gap g the energy of the radiation can be varied. By tuning the shift in a split undulator circular and elliptical radiation can be generated.

3.5 Synchrotron Radiation and Undulator Beam-Lines

Only a very short description of synchrotron radiation will be given here since excellent reviews are available in the literature [100–102]. All x-ray absorption experiments presented throughout this thesis were recorded at the third generation synchrotron radiation facility BESSY II. Synchrotron radiation arises from acceleration of charged relativistic particles (here electrons).
Electrons with an energy of 1.7 GeV circulate in a storage ring, which consists of straight segments and deflecting dipole magnets. Electron trajectories were corrected by sextupole and octupole magnets and energy losses are compensated in micro wave resonators. Whenever passing a dipole magnet synchrotron radiation is emitted according to the Maxwell equations. By Lorentzian transformation from the reference system of the electron to the laboratory frame of reference the Hertzian dipole characteristic of the radiation is modified in such a way that radiation is mainly emitted in the direction of electron motion. Higher radiation intensities were generated by using un-

	U49-2-PGM	UE52-SGM
energy range	85-1600 eV	90-1500 eV
resolving power	25000 (85-500 eV) 15000 (500-1500 eV)	> 4000
flux	10^{13} photons/s (85-500 eV) 10^{12} photons/s (500-1500 eV)	> 10^{12} photons/s
polarization	horizontal	variable
divergence	2 mrad × 2 mrad	6 mrad × 1 mrad

Table 3.1: Technical specification of the undulator beam lines U49-2-PGM [103] and UE52-SGM.

dulators inserted in the straight segments of the storage ring. Undulators are periodical magnetic structures with a variable gap, *cf.* figure 3.5. Linear polarized radiation emitted by electrons on a sinusoidal trajectory can interfere constructively enhancing the intensity by a factor of N (N number of magnet pairs in the undulator). When introducing a shift in a split undulator, as shown in the lower panel of figure 3.5, electrons on spiral trajectories emit elliptical or circular polarized light depending on the undulator shift. The degree of polarization is well defined and about 90 %.

The undulator radiation is coupled to a beam line where the spectral purity of the radiation is further improved by plain or spherical grating monochromators. The resolving power and transmitted intensity strongly depends on the beam line. All experiments were carried out at U49-2-PGM [103] and UE52-SGM beam lines, for technical details see table 3.1 and reference [104].

Chapter 4

Experimental and Computational Details

In this chapter details on the data acquisition and analysis as well as some preparatory calculations are presented. Purpose of the first section is to get a detailed overview of the preparation procedure before taking x-ray absorption or x-ray magnetic circular dichroism spectra and the data acquisition cycle. Details of the data analysis can be found in the second section of this chapter, focusing on background subtraction and normalization procedures. In the last section some preparatory calculations are presented, which aim to establish parameters for further calculations.

4.1 Data Acquisition

Before recording x-ray absorption spectra three preparatory steps were always performed. Firstly, the cluster ion yield in the mass region of interest is optimized, whereas all ion optics are operated in transmission mode. A typical mass spectrum is shown in panel (a) of figure 4.1. Subsequently, the mass selection is switched on and transmission is optimized for the cluster of interest. Typically, the ion yield drops by a factor of two in selection mode, as can be seen from panel (b) of figure 4.1.

The second step - accumulating target density - is achieved by operating the trap in storage mode by tuning the trap parameters to efficiently store the selected cluster. In the last preparative step, the x-ray beam is coupled in and the trap parameters are adjusted in such a way that the ion yield of fragments induced by x-ray absorption is maximal, which can be seen in panel (d) of figure 4.1. Hereby the trapping efficiency of the parent cluster is eventually reduced.

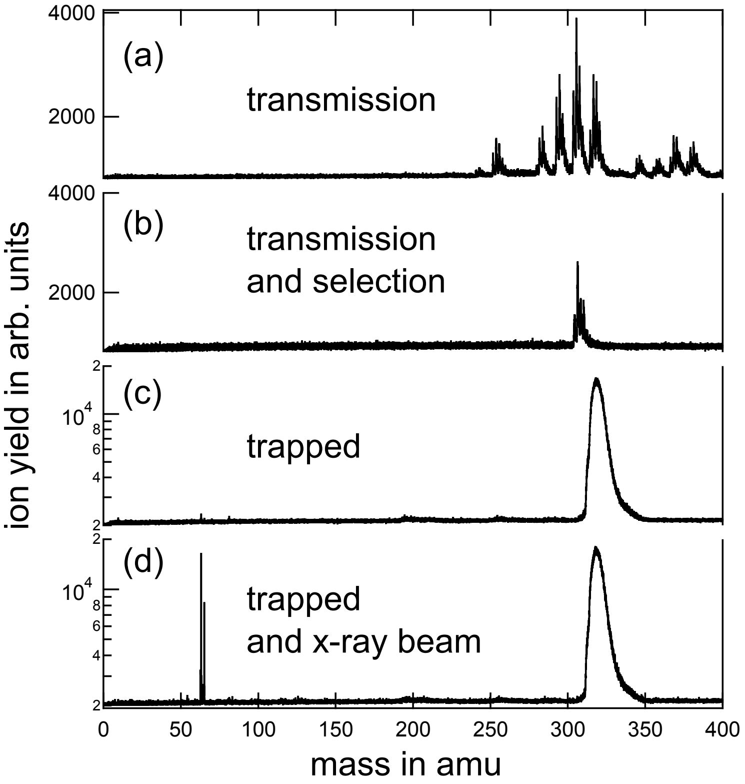

Figure 4.1: Mass spectra taken in preparation for recording x-ray absorption spectra of $CrCu_4^+$. Panel (a) shows a mass spectrum optimized for the mass region of interest. Panel (b) shows the very same mass range but with the quadrupole mass filter in selecting mode. The ion yield of $CrCu_4^+$ is reduced by about 50 %. Target density is accumulated by storing the selected cluster, *cf.* panel (c). Panel (d) shows a mass spectrum with additional x-ray beam induced fragments.

X-ray absorption spectra were then obtained by recording the ion yield of photo-induced fragments, *cf.* panel (d) of figure 4.1, as a function of the photon energy. A schematic view of the data acquisition is given in figure 4.2. While recording the ion yield, several quantities were simultaneously collected such as synchrotron and beam-line parameters as well as photon flux measured using a GaAsP diode, *cf.* figure 4.2. When setting a new photon energy the x-ray beam is blocked with a beam shutter.

In order to be able to subtract a background, x-ray absorption spectra are recorded from well below the resonances up to about 20 eV above resonant excitations. In most of the cases, the energy resolution was chosen to be 250-625 meV at the resonances to resolve multiplet structures. At every energy point mass spectra were averaged for 8-12 s at frequencies of 100-500 Hz. Afterwards, a x-ray absorption spectrum with opposite photon helicity is recorded. Taking at least an additional pair of x-ray absorption spectra ensures reproducibility of the measurement. Depending on the signal to noise ratio, up to six pairs of x-ray absorption spectra were taken.

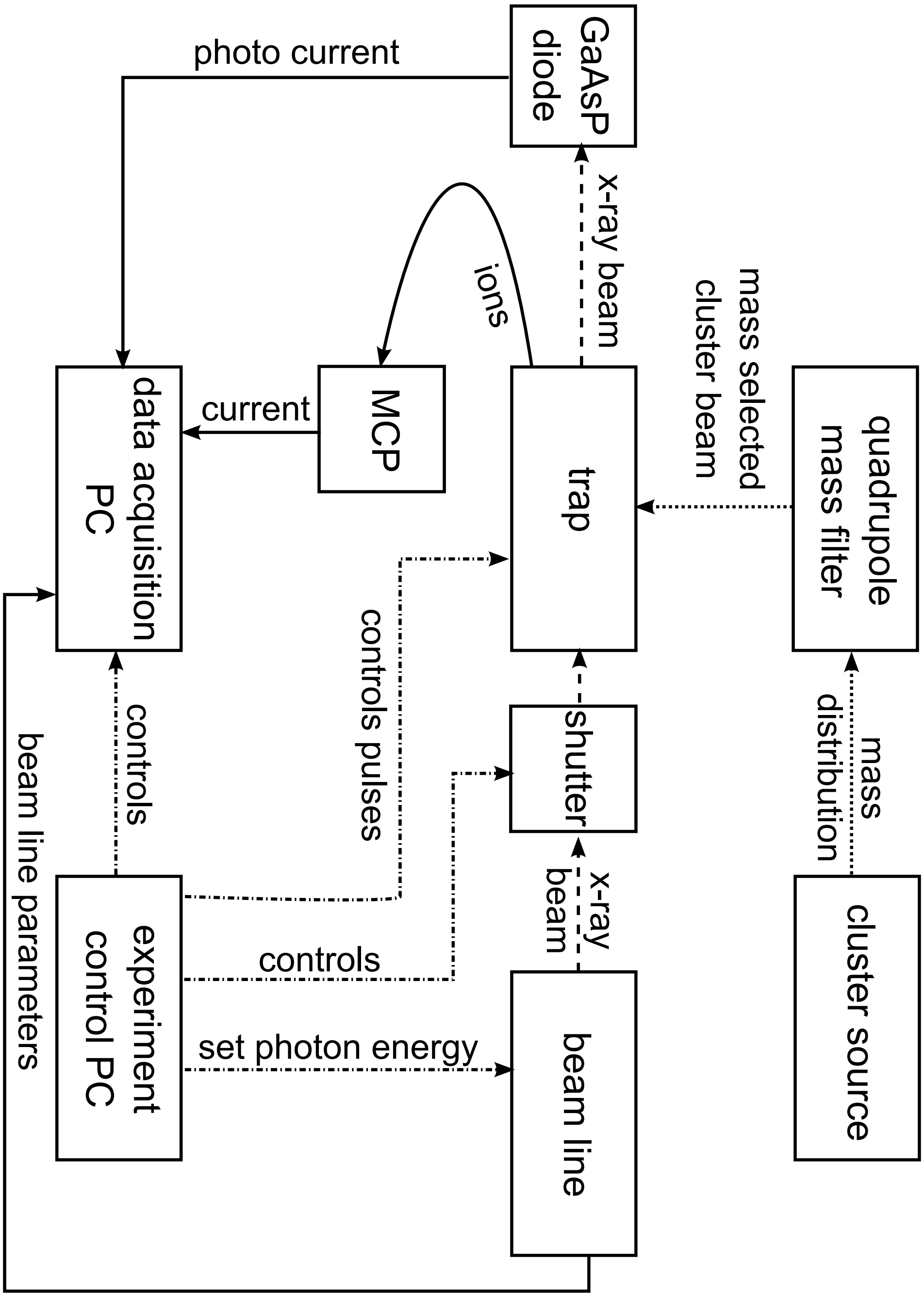
cluster source
mass distribution
quadrupole mass filter
mass selected cluster beam
trap
x-ray beam
GaAsP diode
ions
MCP
current
photo current
data acquisition PC
controls
controls pulses
shutter
x-ray beam
beam line
beam line parameters
experiment control PC
controls
set photon energy

Figure 4.2: Schematic view of the data acquisition, *cf.* sketch of the experimental setup figure 3.1.

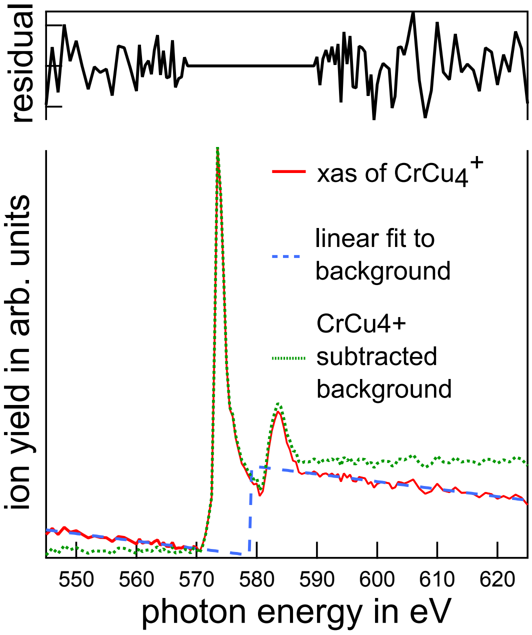

Figure 4.3: The background of a x-ray absorption spectrum (solid red line) is fitted below and above the absorption edge as a linear function (dashed blue line) with the same slope. The residuum of the fit is shown in the upper panel, the straight line indicates the region which was not included in the linear fit. The x-ray absorption spectrum without background is shown as dotted green line.

4.2 Data Analysis

As mentioned in the previous section, x-ray absorption spectra were obtained as the photon energy dependent ion yield of photo induced fragments. The dominant photo fragments are Au_1^+ in case of doped gold and Cr_1^+ and Cu_1^+ in case of chromium doped copper clusters, respectively. In the x-ray absorption spectra of small clusters the ion yield of doubly charged photo fragments becomes dominant. All ion yield spectra were normalized to the incident photon flux obtained by measuring the photo current of a GaAsP diode with known quantum efficiency.

The background, which mainly originates from direct photo ionization of weaker bound electrons [1], is fitted as a linear function below and above the resonances with the constraint of identical slopes and is subsequently subtracted from the x-ray absorption spectrum, *cf.* figure 4.3. The direct photoionization of the x-ray absorption spectra was normalized to unity. The XMCD asymmetry as well as the sum spectra shown in figure 4.4 were subsequently obtained as the average of all possible combinations of x-ray absorption spectra taken with positive and negative helicity. For comparison all XMCD spectra were normalized to the number of absorbers and $3d$-holes. These numbers can be inferred from the integral of the x-ray sum spectra after subtracting contributions from direct photoionization and resonant excitations into higher orbitals

---

[1] Direct photo ionization at chromium and copper M-edges and gold N and O edges [105].

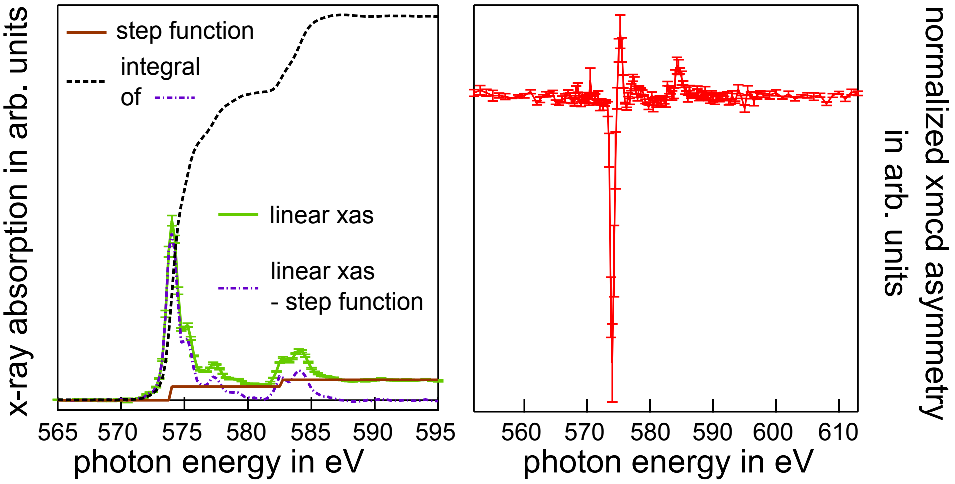

Figure 4.4: Data processing exemplary shown for $CrAu_2^+$. In the left panel linear XAS, step function, to account for transitions other than $2p \rightarrow 3d$, and integral of linear XAS (previously the step function was removed) is shown. In the right panel the normalized XMCD asymmetry is shown. The error is obtained as the standard error of the mean value.

allowed by dipole selection rules. The corresponding step functions were directly placed at resonant excitation energies of $2p_{3/2,1/2} \rightarrow 3d$ transitions, which can be seen in figure 4.4 and was shown to be reasonable procedure [32]. The intensity ratio of the step functions was set to 2/3 according to the degeneracy of the $2p_{3/2,1/2}$ levels. A normalized XMCD spectrum is shown in the right panel of figure 4.4.

4.3 Computational Details

Most of the calculations were carried out using the QUANTUM ESPRESSO 5.0 code [86]. In QUANTUM ESPRESSO 5.0 the calculations are based on plane waves exploiting the periodicity of a bulk material. In practice this is done by periodically repeating a super cell. Since properties of an isolated cluster should be calculated here, the cell has to be large enough so that the periodic images of the cluster do not interact with each other, but as small as possible to limit the computational cost. This is even more challenging because of the long-range Coulomb interaction of cationic clusters. Therefore, prior to the calculations the convergence with respect to cell size and kinetic energy wave function cutoff was tested. In all calculations only one k-point (the Γ point) was used for the k-point sampling because no dispersion is expected for the finite systems investigated throughout this thesis.

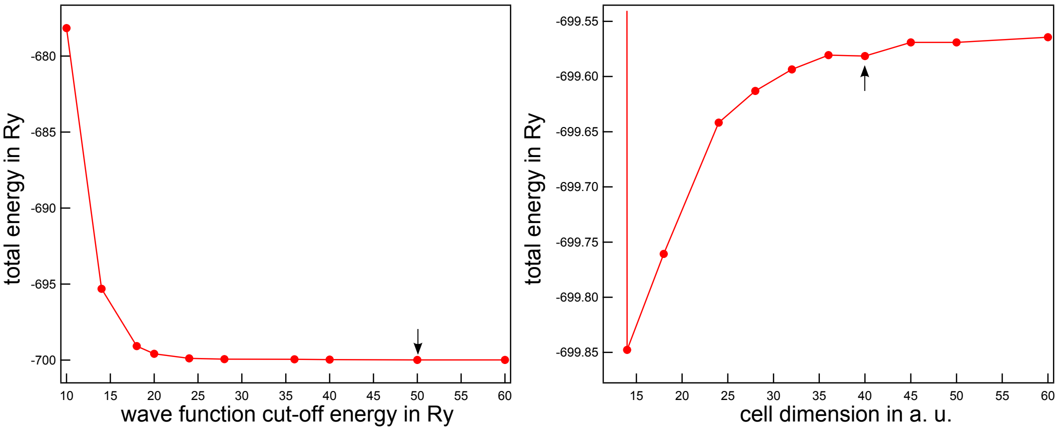

Figure 4.5: Convergence test for CrAu_n^+: Total energy shown as a function of cell size and wave function kinetic energy cut-off. Optimal values used for subsequent calculations are indicated by an arrow.

The total energy as a function of the cell size for CrAu_6^+ is shown in the right panel of figure 4.5. The arrow indicates the cell size used in all following calculations, since here the total energy starts to oscillate, which is typical for the energy convergence in plane wave codes. In the left panel of figure 4.5 the total energy as a function of the kinetic energy wave function cut-off is shown. Again the arrow indicates the value used for all following calculations. This value of 50 Ry for the kinetic energy wave function cut-off was chosen since the change in total energy dropped below 50 meV, which is the accuracy of the calculations presented here.

The search for ground state structures in case of CrCu_n^+ clusters was done using the TURBOMOLE 6.2 program suite. Here a basis set of triple-ζ quality (def2-TZVP) was used in all calculations. This is known to yield good quantitative results for $3d$ transition metals [106].

All calculations were carried out by employing the PBE approximation [107] to the exchange-correlation functional.

Chapter 5

Electronic Structure of Early $3d$ Transition Metal Impurities in Non-Magnetic Gold Clusters

In this chapter the electronic structure of doped gold clusters will be studied by systematically exchanging the dopant atom and varying the cluster size. This was done in order to vary the number of $4s$ and local $3d$ electrons of the impurity as well as the number of delocalized electrons in the host material. The local electronic structure and details in the binding strongly depend on the nature of the dopant atom. For example, starting from the early transition metal scandium a slight odd-even effect in the electronic structure is evident. This effect becomes very pronounced in titanium doped gold clusters. In contrast, the electronic structure of the impurity is almost independent of the number of gold atoms in vanadium doped gold clusters. In chromium doped gold clusters the impurities electronic structure is dominated by shell closure in the gold host.

Linear x-ray absorption spectra presented throughout this chapter are taken with an energy resolution of 125 meV, which enables us to resolve the multiplet structure present in the x-ray absorption of all investigated clusters. The multiplet structure is very characteristic for the symmetry of the environment, the occupation of the $3d$ states as well as their hybridization due to bonding. This sensitivity makes x-ray absorption spectroscopy a finger print method [31, 108]. Although the energy resolution in principle allows us to resolve individual transitions, the high density of states at the Fermi level and the multiplet structure causes overlap of the life time broadened lines [109].

In addition density functional theory calculations were performed for all clusters investigated throughout this chapter. Established ground state structures [12] were re-optimized and the total density of states (DOS) as well as projected density of states (PDOS), obtained from projecting the density of states onto atomic orbitals, were calculated. These are used to analyze the electronic structure and to interpret the experimental x-ray absorption data.

We follow the periodic table and start with a discussion of scandium doped gold clusters.

5.1 Local Electronic Structure of Scandium Doped Gold Clusters

In figure 5.1 the linear x-ray absorption spectra of mass selected ScAu_n^+ clusters in a size range of $n = 1 - 6$ are presented. Additionally, the spectrum of atomic Sc^+ is shown [32]. The x-ray absorption spectra of ScAu_1^+ and Sc^+ feature almost identical spectral shapes, which indicates a very similar local electronic structure. The ground state electronic configuration of Sc^+ is $[\mathrm{Ar}]3d^1 4s^1$, hence it can be expected to find one $3d$-electron localized at the scandium site in ScAu_1^+ and that bonding is mediated by the $4s$ electron.

Localization of the $3d$-orbital can indeed be observed from a comparison of the total and the scandium d-projected density of states, *cf.* figure 5.2. Here the state close to the Fermi energy (highlighted by the box) has almost pure scandium d-character, which points to a complete localization of this state at the scandium site.

In case of ScAu_2^+ the spectral signature becomes very narrow and exhibits only two main lines comparable to the x-ray absorption spectrum of atomic calcium cation [32]. This hints at a local $3d^0$ configuration of the scandium atom in ScAu_2^+, which is confirmed by the scandium d-projected density of states shown in figure 5.2 where no localized $3d$-electron can be found. Furthermore the $3d$-spin polarization obtained from a Löwdin population analysis [110, 111] is $0\,\mu_\mathrm{B}$, *cf.* figure 5.3, which is in perfect agreement with the assumption of a local $3d^0$ configuration due to delocalization.

The described observations for $\mathrm{ScAu}_{1,2}^+$ can be generalized to larger clusters. Indeed, odd numbered ScAu_n^+ clusters always feature pronounced multiplet signatures in their x-ray absorption spectra while even numbered clusters have more symmetric and narrow spectral features. Although the odd-even effect is less pronounced for larger ScAu_n^+ clusters it clearly survives up to $n = 6$ as can be seen for example from the difference of $3d$ spin up and down occupation shown in figure 5.3. The $3d$-electron in odd numbered ScAu_n^+ clusters $(n > 1)$ hybridizes more strongly with the gold electronic states as compared to ScAu_1^+, since the coordination of the scandium impurity increases linearly with the cluster size.

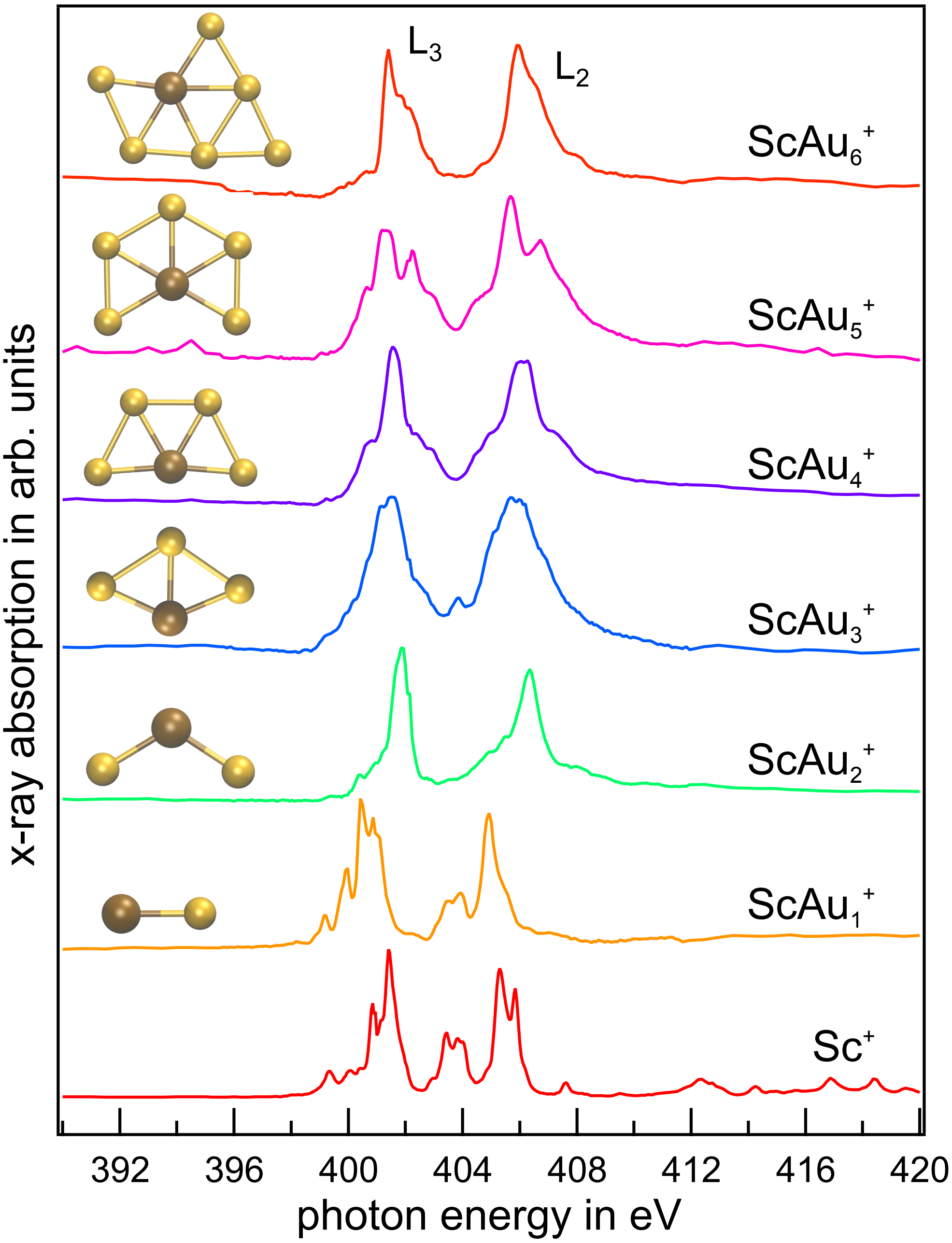

Figure 5.1: Linear x-ray absorption spectra of scandium doped gold clusters at the $L_{2,3}$ edges of scandium. The spectral signature changes drastically as a function of the cluster size. There is some resemblance of the x-ray absorption spectrum of ScAu_1^+ and Sc^+ indicating a localized $3d$-electron in ScAu_1^+. Additionally shown are the ground state structures, taken from [12] and re-optimized.

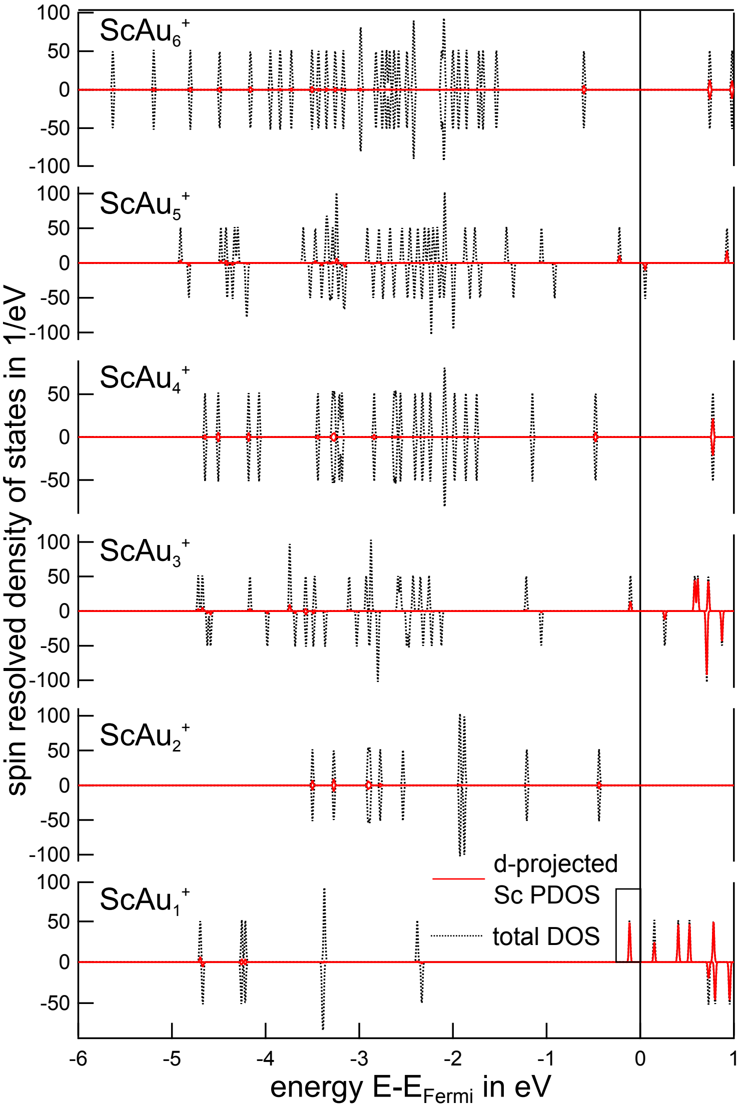

Figure 5.2: Spin resolved total and scandium d-projected density of states shown for ScAu_n^+, $n = 1 - 6$. Positive and negative values of the density of states represent spin-up and spin-down states, respectively.

Since the mean radius of the 3d-orbitals in atomic scandium, which is about 1.6 Å, is quite large compared to an inter-atomic separation of about 2.5 Å in ScAu_n^+ clusters, one could expect the participation of the 3d-electron in bonding for all cluster sizes. Furthermore 3d and 4s states in scandium may benefit from sd-hybridization since they are energetically almost degenerate [112]. From these observations a strong hybridization with the gold electronic states might be expected independent of the cluster size. However, the 3d-electron remains localized at least to some extend in odd numbered cluster. Hence, it can be deduced that it is energetically favorable to delocalize an even number of electrons. This will be discussed in more detail in the following section, since the odd-even effect in the electronic structure is more pronounced

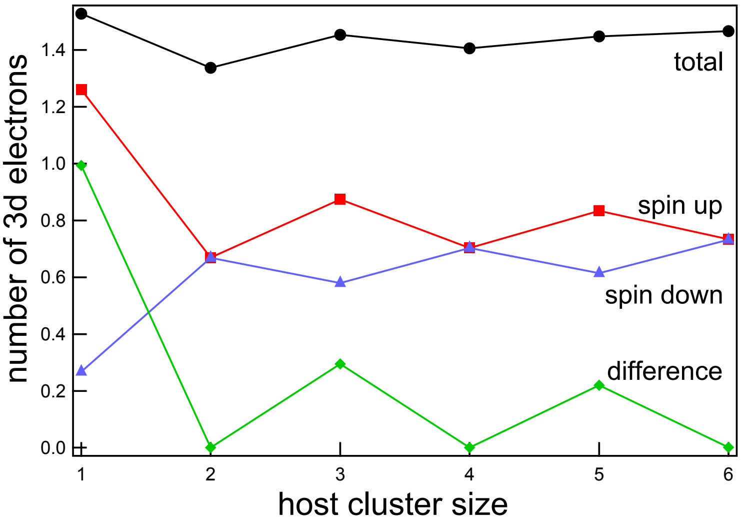

Figure 5.3: Population analysis of the scandium $3d$-orbitals in ScAu_n^+ clusters using a Löwdin population analysis. The total $3d$-occupancy exhibits a slight odd-even effect, while it is pronounced for the difference in spin-up and spin-down occupation.

in TiAu_n^+ clusters, due to the more compact $3d$-orbitals and opening of the $3d$-$4s$ gap along the $3d$ transition metal series [112].

5.2 Odd-Even Effects in the Electronic Structure of Titanium Doped Gold Clusters

In figure 5.4 linear x-ray absorption spectra of titanium-doped gold clusters at the $L_{2,3}$ edges of titanium are presented in a size range of $n = 1 - 9$. At first glance there is a strong odd-even effect visible in the x-ray absorption of TiAu_n^+ clusters. The planar, odd numbered TiAu_n^+ clusters (up to $n = 5$) exhibit almost identical spectral signatures. The x-ray absorption signal of these clusters nicely resembles the x-ray absorption spectrum of an isolated titanium cation ([Ar]$3d^2 4s^1$), *cf.* the Hartree-Fock calculation shown in figure 5.4. This finding suggests that both $3d$ electrons in odd numbered TiAu_n^+ clusters remain localized at the titanium site to a large extend and do not participate in bonding.

Even numbered TiAu_n^+ clusters have very similar spectral shapes among each other as well, although a slightly increasing broadening of the spectral features with increasing cluster size can be observed.

However, in contrast to odd numbered TiAu_n^+ clusters, no similarity to the x-ray absorption spectrum of atomic titanium can be found. As already mentioned, x-ray absorption locally probes the unoccupied density of states, therefore changes in the symmetry or the unoccupied density of states due to bonding or fractional electron transfer to or away from $3d$ states would result in a deviation from the atomic spectral shape. Indeed, a small odd-even variation

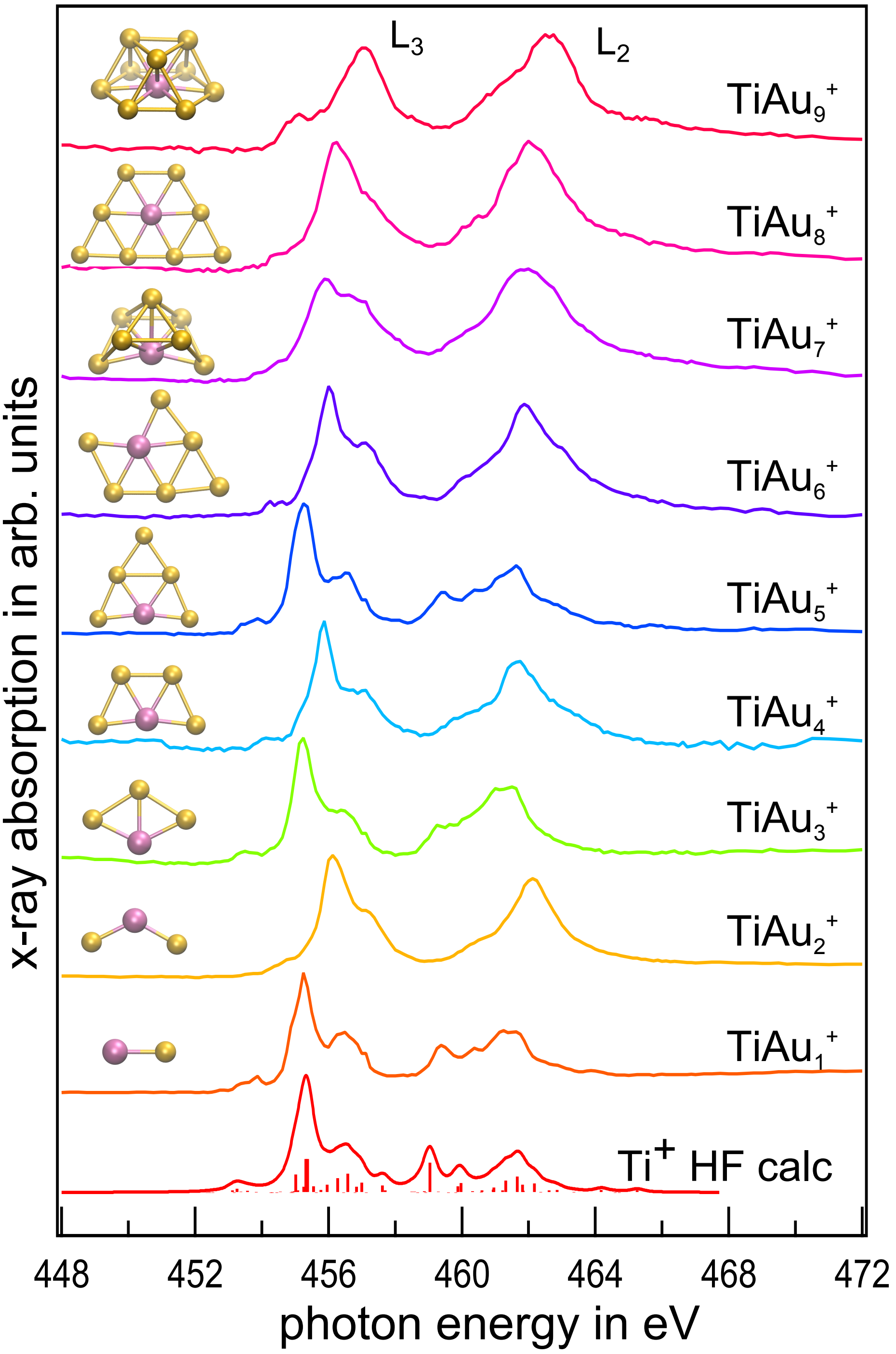

Figure 5.4: Linear x-ray absorption spectra of titanium doped gold clusters at the $L_{2,3}$ edges of titanium. The spectral signature of odd numbered TiAu_n^+ in a size range of $n = 1 - 5$ show a strong resemblance with an atomic Hartree-Fock calculation of the XAS of Ti^+. Furthermore, a second set of similar spectral shapes are found for even numbered TiAu_n^+ clusters in a size range of $n = 2 - 8$. Additionally shown are the ground state structures, taken from [12].

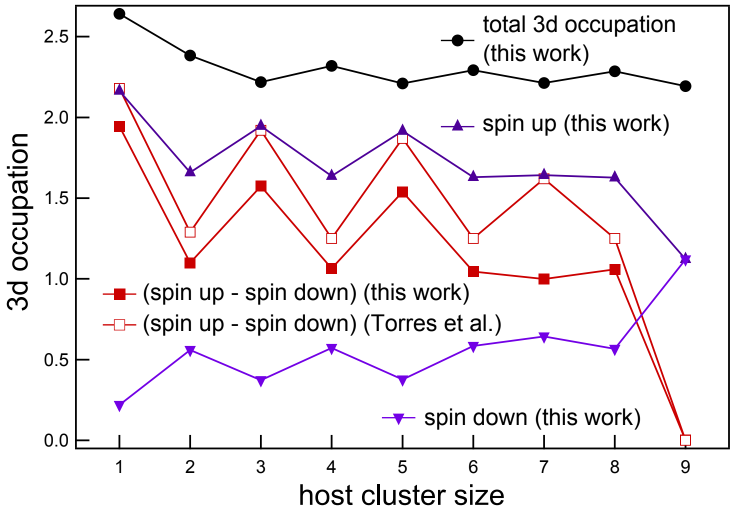

Figure 5.5: Total and spin resolved $3d$ occupation derived from a Löwdin (this work) and Mulliken (Torres *et al.* [12]) population analysis of TiAu_n^+ clusters. A small odd-even effect in the total $3d$ occupation is evident.

of the $3d$ occupancy exists, as can be seen from the total and spin resolved $3d$ occupation presented in figure 5.5, which is derived from a Löwdin population analysis [110, 111]. Still, both odd and even numbered TiAu_n^+ clusters have about two $3d$ electrons, with a variation in $3d$ occupancy smaller than 10 %. Such a small effect might not result in the different spectral signatures for odd and even numbered TiAu_n^+ clusters.

To shed some more light on the odd-even aspect the density of states, shown in figure 5.6, will be analyzed. Again, the occupied density of states is very similar among odd and even numbered TiAu_n^+ clusters, respectively. In figure 5.6 the total density of states and the titanium d-projected density of states is displayed for the whole series of TiAu_n^+ clusters, $n = 1 - 9$. From a comparison of the DOS and the PDOS the amount of hybridization of the titanium $3d$ states can be deduced. There is a severe difference between odd and even numbered TiAu_n^+ clusters, as can be seen from the figure. In case of even numbered TiAu_n^+ clusters only one non-hybridized $3d$ state remains, whereas for odd numbered TiAu_n^+ clusters there are two almost non-hybridized $3d$ states present. In contrast to these well localized states near the Fermi level (highlighted by the boxes), in even numbered TiAu_n^+ clusters the second $3d$ electron strongly hybridizes with the sd-states of gold well below the Fermi level, *cf.* figure 5.6.

The finding of two atomic-like $3d$ electrons in odd numbered TiAu_n^+ clusters, which do not participate in bonding, is in very good agreement with the experimental x-ray absorption spectra. Since the titanium atom in odd numbered TiAu_n^+ has an almost undisturbed atomic-like $3d^2$ electron configuration, these clusters nicely resemble the atomic x-ray absorption spectrum of titanium, *cf.* figure 5.4.

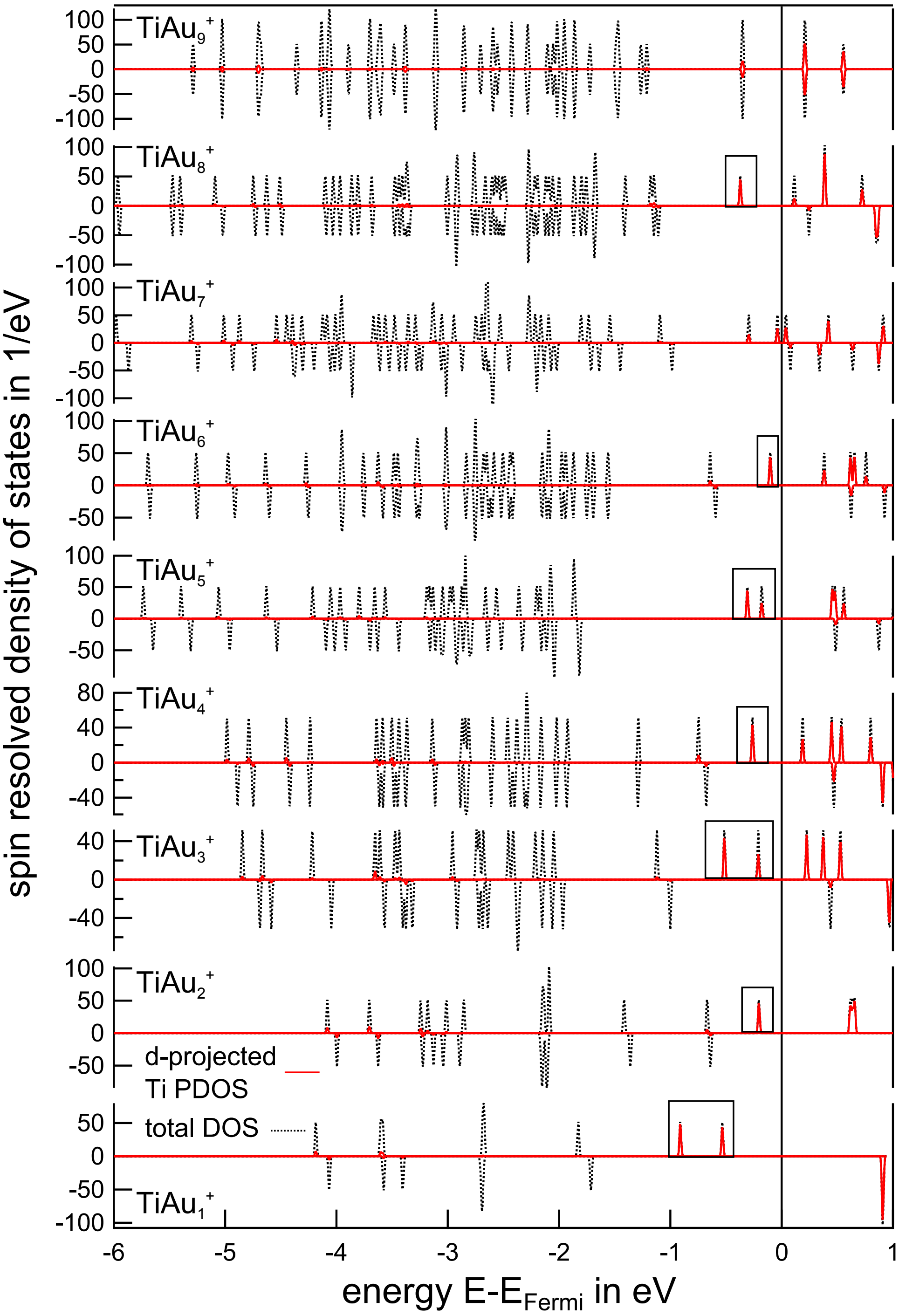

Figure 5.6: The total density of states (black dotted line) and the 3*d*-projected titanium density of states (red solid line) of TiAu$_n^+$ are shown. While odd numbered TiAu$_n^+$ clusters exhibit two states at the Fermi level of almost pure 3*d* character, even numbered TiAu$_n^+$ clusters exhibit only one of these states. In case of even numbered TiAu$_n^+$ clusters the second 3*d* electron is strongly hybridized with the gold *sd* states. Positive and negative values of the density of states represent spin-up and spin-down states, respectively.

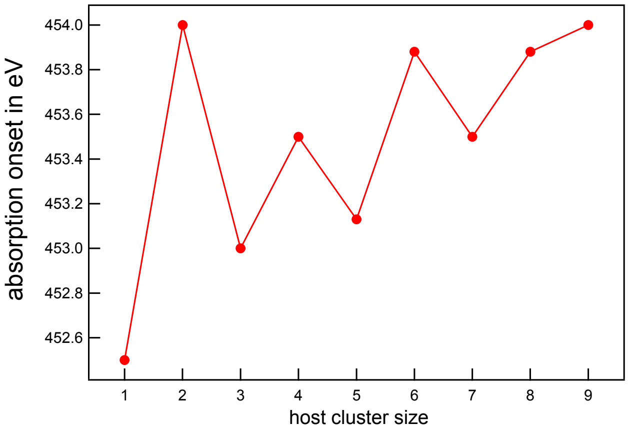

Figure 5.7: The absorption onset of $TiAu_n^+$ clusters as function of size suggests strong $3d$-electron localization for odd numbered $TiAu_n^+$ clusters compared to even numbered ones.

The stronger localization of the $3d$ electrons in odd numbered $TiAu_n^+$ clusters is also supported by the size dependent x-ray absorption onset shown in figure 5.7. Here, odd numbered $TiAu_n^+$ clusters with two localized $3d$ electrons exhibit an absorption onset at lower excitation energy than even numbered $TiAu_n^+$ clusters with one localized and one hybridized and therefore delocalized $3d$ electron state. As was shown for pure transition metal clusters, a shift of the absorption onset towards lower excitation energy indicates a stronger localization of the $3d$ electrons [113, 114].
Additionally, the difference in occupation of titanium $3d$ spin-up and spin-down states is shown in figure 5.5, obtained from a Löwdin [110, 111] (this work) and Mulliken [115] population analysis (Torres *et al.* [12]). The difference of about 0.2 electrons between the Löwdin and Mulliken population analysis is not surprising, since both methods are strongly basis set dependent [116]. The size dependent trend, however, is, apart from the case of $TiAu_7^+$, that will be discussed below, similar. It shows that odd numbered $TiAu_n^+$ clusters exhibit larger spin polarizations than even numbered clusters. This finding indicates that only localized, but not itinerant electrons contribute to the spin polarization. One can compare this behavior with what one would expect from a very simple model of molecular bonding, namely the Heitler-London model [117]. In this model, participation in bonding results in low spin states which enhance the stability of the molecule by effective screening of the Coulomb interaction among the ionic cores. In odd numbered $TiAu_n^+$ clusters where two localized $3d$ electrons are present the local spin magnetic moment is about $2\,\mu_B$, whereas in even numbered $TiAu_n^+$ clusters the delocalized electron participating in bonding does not contribute to the local spin polarization, hence even numbered $TiAu_n^+$ clusters exhibit a local spin magnetic moment of about $1\,\mu_B$. However, there is a discrepancy in the local spin moment of $TiAu_7^+$ obtained in this work and the work of Torres *et al.* [12].

The deviation from the odd-even pattern in TiAu_7^+ is probably caused by a geometrical 2D → 3D transition, increasing the mean coordination of the titanium atom and therefore maximizing the titanium-gold bonding. This in turn results in a reduction of the local spin moment as found in our population analysis. This hypothesis is additionally supported by the size dependent absorption onset shown in figure 5.5. Although the absorption onset in TiAu_7^+ is reduced compared to the neighboring cluster sizes, the absolute value is comparable to even numbered TiAu_n^+ clusters and significantly enhanced with respect to the value for small odd numbered TiAu_n^+ clusters. Therefore a similar delocalization of the $3d$ electrons as in even numbered TiAu_n^+ clusters can be expected, which is consistent with our DFT calculations. This is strong evidence that the structure of TiAu_7^+ presented here, is indeed the the structure present in our experiment.

The origin of the strong odd-even effect in TiAu_n^+ clusters is still unclear. It might have its origin in electron pairing effects in the free electron gas formed in the host cluster, as observed in pure gold clusters [118–120].

To further elucidate this question, we neglect the $3d$ electrons of titanium for now. There are then $n + 1$ delocalized electrons in the TiAu_n^+ system, n electrons stem from the $6s$-orbitals of gold while one electron is contributed by the $4s$-orbital of titanium. Hence, there is an odd (even) number of delocalized electrons present in case of even (odd) numbered TiAu_n^+ clusters. It seems energetically favorable for even numbered TiAu_n^+ clusters to delocalize one $3d$ electron, since the $3d^2 4s^1 \rightarrow 3d^1 4s^2$ promotion energy of about $3\,\mathrm{eV}$ [121] is overcompensated by the gain from kinetic energy reduction and reduction of intra-atomic Coulomb interaction by delocalization. This is very different for odd numbered TiAu_n^+ clusters: Here a delocalized titanium $3d$ electron would have to populate a free electron gas state higher in energy, since the jellium states are already doubly occupied.

Thus, titanium in TiAu_n^+ clusters serves as an electron donor providing exactly the right number of electrons to stabilize the free electron gas bond in the gold host cluster, without a strong overall disturbance of the gold cluster geometry. All the ground state structures of TiAu_n^+ ($n = 1 - 9$) clusters posses identical symmetry as the ground state structures of neutral gold clusters [122, 123], except for TiAu_7^+ and TiAu_9^+.

Moreover, there is a second effect beneath the strong odd-even effect. From the density of states presented in figure 5.6 it can be seen that the free electron gas states (mainly all states which do not exhibit titanium $3d$-character) are more strongly bound in case TiAu_1^+ and TiAu_5^+ as compared to the other cluster sizes. This may originate from shell closure in a two dimensional potential well in these to systems with two and six delocalized electrons, respectively.

In summary, all these results suggest that one always finds an even number of delocalized electrons in TiAu_n^+ clusters.

5.3 Independence of the Local Electronic Structure on Impurity Coordination: Vanadium Doped Gold Clusters

In figure 5.8 the linear x-ray absorption spectra of vanadium doped gold clusters together with their ground state geometries [12] are presented in the size range of $n = 1 - 7$.

Apart from VAu_2^+ which will be discussed later, clusters of sizes $n = 1 - 5$ exhibit almost identical spectral shapes. Because of large life-time broadening due to additional electronic relaxation channels (Coster-Kronig and Super-Coster-Kronig transitions) the L_2-edge is not as well resolved as the L_3-edge. The similarity of the mentioned spectral shapes is therefore especially striking at the L_3-edge. The similar spectral shapes indicate that these clusters have the same local electronic structure. Therefore the bonding mechanism of vanadium to the gold host has to be the same or at least very similar for clusters with 1 and 3-5 gold atoms. At first glance this is somehow surprising, since here the coordination of the vanadium impurity increases linearly with the cluster size. Therefore it could be expected that the interaction strength increases with the cluster size.

An *atomic* Hartree-Fock calculation shows, that the x-ray absorption spectra of the small VAu_n^+ clusters do not resemble the electronic structure of the vanadium cation with its $3d^4 4s^0$ ground state configuration. Since the vanadium cation offers no $4s$-electron for bonding, in contrast to scandium and titanium, at least some of the vanadium $3d$-states are expected to hybridize with the host materials electronic states. However, even more likely is the promotion of a $3d$ electron into the far more extended $4s$ orbital which then forms a molecular orbital with the host electronic states. This can be assumed to be energetically favorable since the $3d^4 4s^0 \rightarrow 3d^3 4s^1$ promotion energy is with 320 meV [124] rather small. However, since the x-ray absorption spectra do not resemble a pure local $3d^3 4s^1$ electron configuration and the local environment is very different in VAu_n^+ clusters $n = 1 - 7$, vanadium $3d$ orbitals have to be involved in the bonding, at least partly.

The similar x-ray absorption spectra for all VAu_n^+ clusters, $n = 1 - 5$, suggest that the number of $3d$-electrons is almost identical. That this is indeed the case can not be easily seen from the density of states, *cf.* figure 5.10, but from the Löwdin population analysis, which is shown in figure 5.9. The total number of $3d$-electrons is about 3.5 for all investigated cluster sizes, except

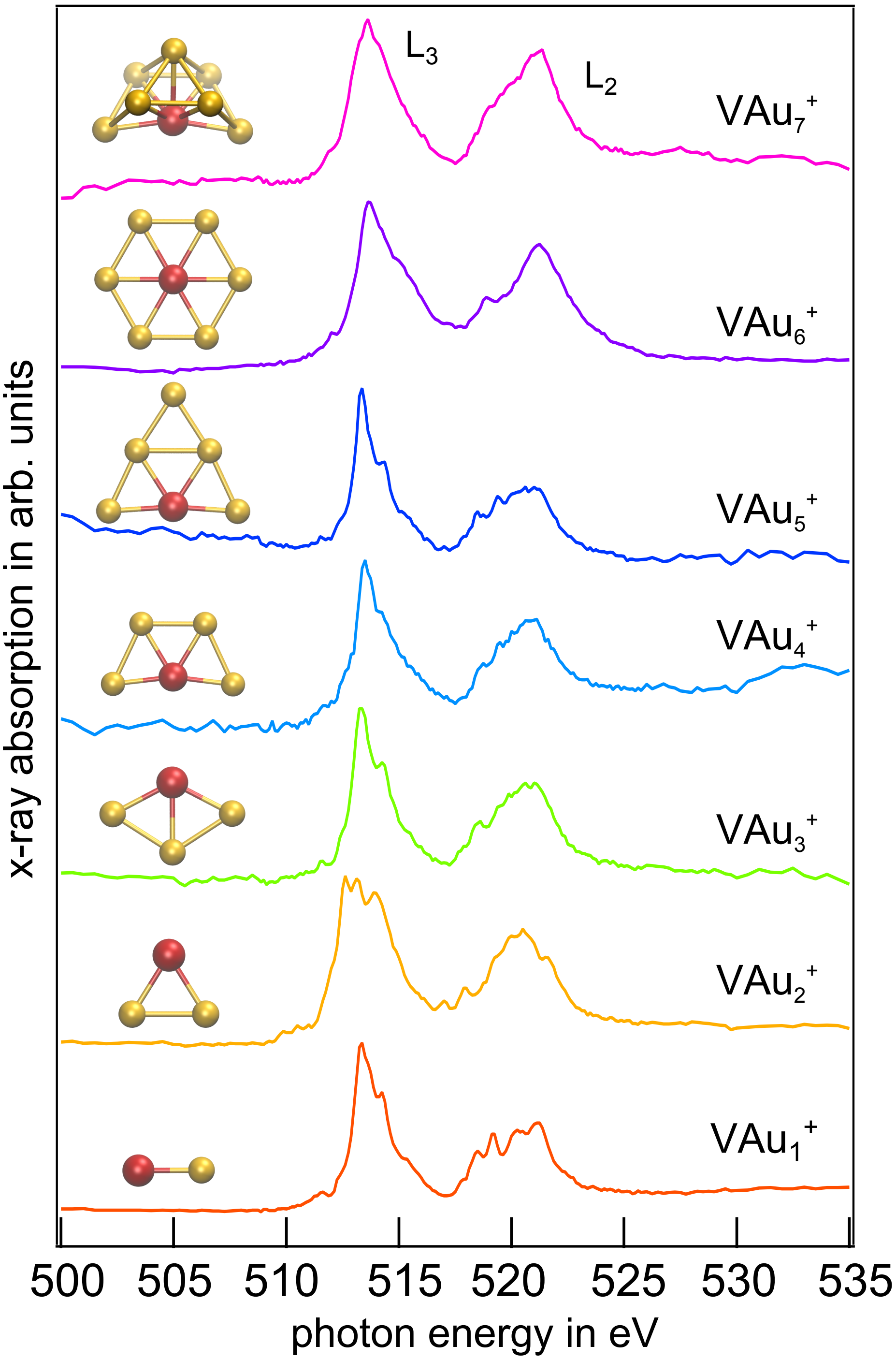

Figure 5.8: Linear x-ray absorption spectra of vanadium doped gold clusters at the $L_{2,3}$ edges of vanadium. The spectral signature remains almost unchanged as a function of the cluster size, although dramatic structural changes are present, as can be seen from the ground state structures (taken from [12]).

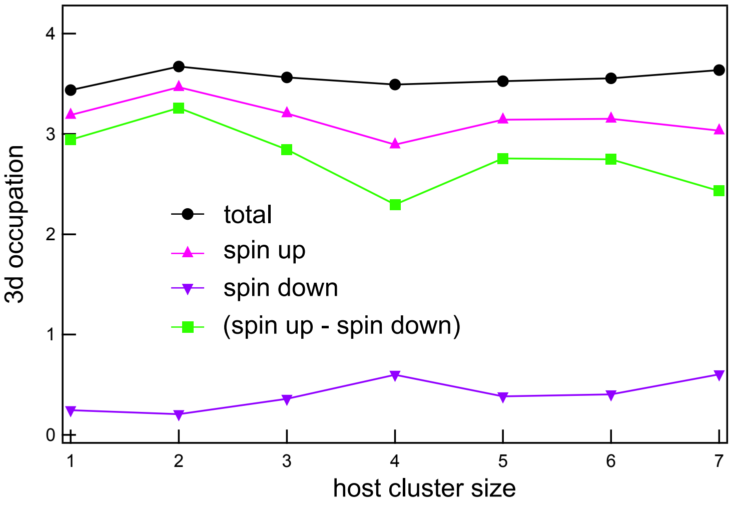

Figure 5.9: Total and spin resolved $3d$ occupation of VAu_n^+ clusters in a size range of $n = 1 - 7$. The occupation numbers are obtained from a Löwdin population analysis. The total number of $3d$ electrons varies only very weakly with the cluster size pointing to almost identical local electronic structure of the vanadium atom in VAu_n^+ clusters. Only the VAu_2^+ cluster exhibit a slightly enhanced $3d$ occupation.

for the VAu_2^+ which exhibits a slightly enhanced number of $3d$-electrons. This in turn explains the deviation of the spectral shape for the VAu_2^+ cluster.
However, vanadium-doped gold clusters are qualitatively different from ScAu_n^+ and TiAu_n^+ clusters since they are missing the pronounced odd-even effect in their electronic structure. In order to feature an even number of delocalized electrons in even numbered VAu_n^+ clusters, the vanadium atom would have to delocalize a second $3d$-electron. Again this involves an energy cost which can be estimated by the promotion energy. Since it is larger than 5 eV [124] delocalization of a second $3d$ electron seems to be improper. Therefore localization of three $3d$-electrons is stabilized and results in considerable spin magnetic moments of about $3\,\mu_\mathrm{B}$ at the vanadium site, *cf.* figure 5.9.
Contrary to the rather simple size dependence of the electronic structure for the smaller clusters, the sudden change in the spectral shape from cluster size five to six is somehow puzzling. Neither changes in the local $3d$-occupation nor a 2D→3D transition, the factors that were responsible for the changes in the spectral shapes of scandium and titanium doped gold clusters, emerge in VAu_n^+ clusters.
A possible reason might be that the structure depicted in figure 5.8 is not the one experimentally present. However, it is unlikely that the clusters produced in the cluster source are not the the ground state species, because of the very mild cooling conditions present in the source, which was shown to produce preferably the geometrical ground state structures [125]. As the potential energy surface of metal clusters is very complex even for small cluster sizes, it seems more likely that the theoretically predicted structure [12] does not represent the ground state geometry of VAu_6^+.

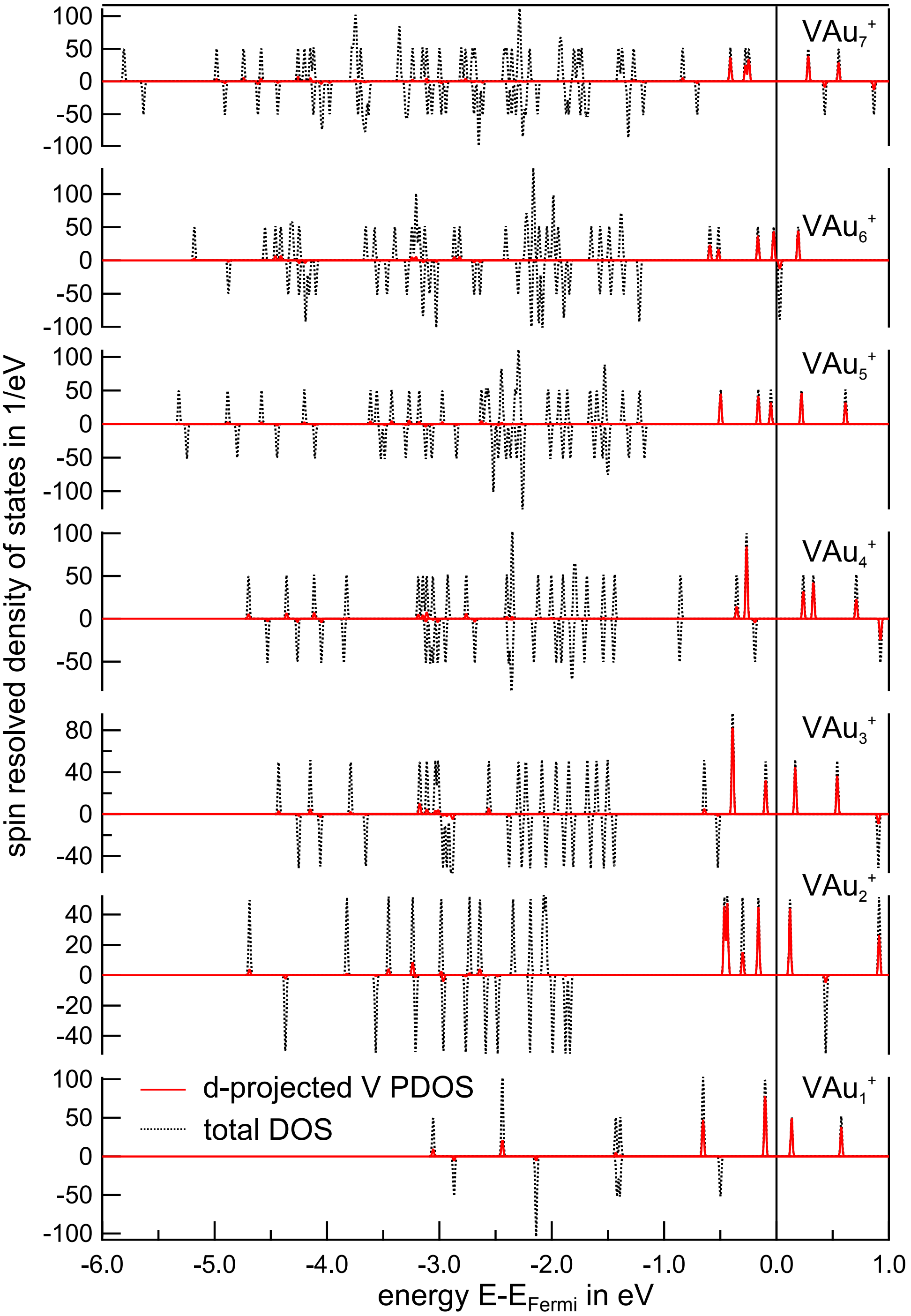

Figure 5.10: Density of states of VAu_n^+ clusters, $n = 1 - 7$. Positive and negative values of the density of states represent spin-up and spin-down states, respectively.

5.4 Local Electronic Structure of Chromium Doped Gold Clusters

In figure 5.11 linear x-ray absorption spectra of chromium doped gold clusters at the $L_{2,3}$ edges of chromium are presented in a size range of $n = 1 - 8$. They were obtained as described in section 4.2. As already discussed, x-ray absorption can be used as a fingerprint method. As can be seen from figure 5.11, the spectral signature changes drastically with the host cluster size, indicating changes in occupation of the $3d$ states or the symmetry of the environment. The x-ray absorption spectra of three clusters attract particular attention: CrAu_n^+, $n = 2, 6, 8$. Here a strong resemblance with the spectra of atomic Cr^+ can be found [32], also evident from a comparison to an atomic Hartree-Fock calculation of Cr^+ [126, 127], *cf.* dotted lines in figure 5.11 (direct photoionization was not taken into account in the calculation). Hence, in these cases the $3d$-electrons of chromium seem to be mainly undisturbed by the gold host matrix or, put differently, do not participate in bonding. Additionally the spectral shapes, *cf.* figure 5.11, indicate that the $3d$ electrons are strongly localized in CrAu_n^+, $n = 2, 6, 8$. As already pointed out, increasing localization of $3d$ electrons yield a shift of the absorption onset towards lower photon energy as was shown by us [114] for pure transition metal clusters. Therefore the shift of the absorption onset towards lower energy compared to the neighboring cluster sizes, as plotted in figure 5.12, is consistent with the assumption of strong localization of the $3d$ electrons in $\mathrm{CrAu}_{2,6,8}^+$.

The interaction of the host with the chromium impurity in these particular systems is strongly suppressed by shell closure in the free electron gas of the gold host cluster. Shell closure is found for two and six electrons in a two dimensional and eight electrons in a three dimensional potential well. Indeed, the gold hosts in $\mathrm{CrAu}_{2,6,8}^+$ feature appropriate shapes, *i.e.* two dimensional structures in CrAu_2^+, CrAu_6^+ and a three dimensional structure in CrAu_8^+, as can be seen from the structures depicted in figure 5.11. Therefore, in $\mathrm{CrAu}_{2,6,8}^+$ the chromium impurity is less strongly bound to the host as compared to the other cluster sizes, as will be discussed in detail in the next chapter.

However, there is also a striking similarity among the x-ray absorption spectra of $\mathrm{CrAu}_{1,5,7}^+$, *cf.* figure 5.11. Actually, this again can be understood in shell closure in a free electron gas, assuming chromium delocalizes one electron. In order to do so, chromium has to delocalize one $3d$ electron, due to its cationic ground state configuration $3d^5 4s^0$ missing a $4s$ electron. This in turn leads to the deviation of the spectral signature from a local $3d^5$ configuration. Since the $3d^5 4s^0 \rightarrow 3d^4 4s^1$ promotion energy is about 1.5 eV [121] it can be assumed that it is feasible to delocalize that one $3d$ electron. This is especially true if

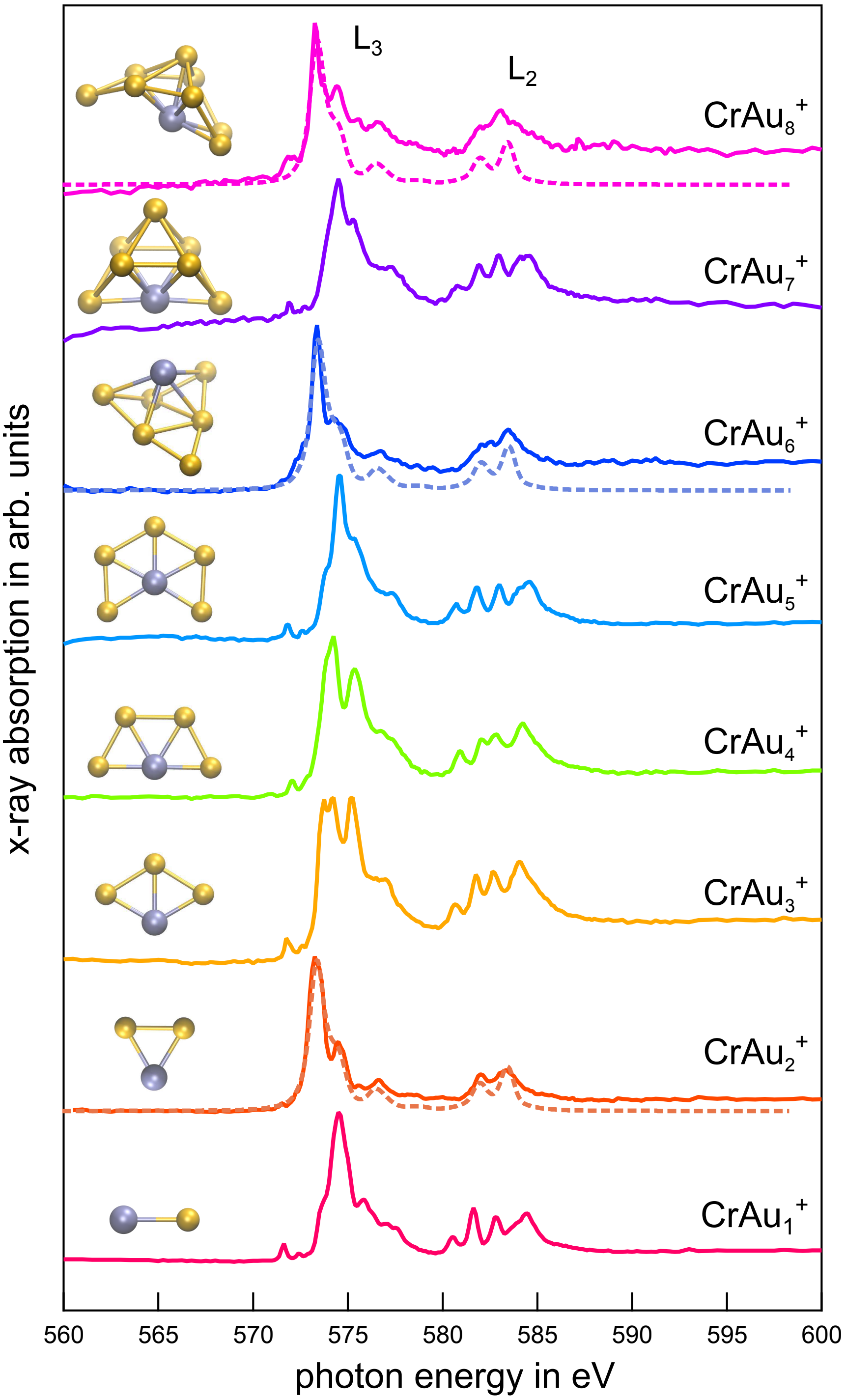

Figure 5.11: Linear x-ray absorption spectra of chromium doped gold clusters at the $L_{2,3}$ edges of chromium. The spectral signature changes drastically as a function of the cluster size. Still, strong resemblance with the atomic XAS can be seen for $\mathrm{CrAu}_{2,6}^+$ by comparison to an atomic Hartree-Fock calculation of Cr^+ (dotted line). Additionally shown are the ground state structures, taken from [12].

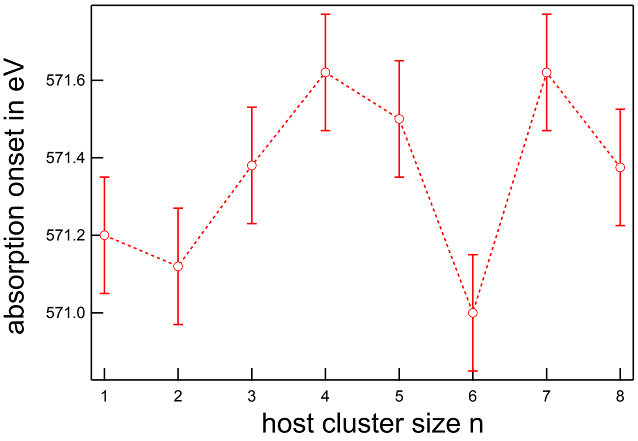

Figure 5.12: Size dependent absorption onset in the x-ray absorption of CrAu_n^+. Strong localization of the $3d$ electrons in $\mathrm{CrAu}_{2,6,8}^+$ is reflected in a shift towards lower energy compared to the neighboring cluster sizes.

the energy gain by delocalizing one electron is large, which can be expected in these cases, since it results in shell closure in the free electron gas with two, six and eight electrons, respectively.
The x-ray absorption spectra of CrAu_n^+ $n = 3, 4$ are almost identical and differ from those of the other CrAu_n^+ clusters.

5.5 Summary

Albeit the very different size dependence in the x-ray absorption spectra of TMAu_n^+ (TM=Sc,Ti,V,Cr), a common ground in the bonding mechanism of the impurity to the host can be deduced. Whenever possible the TMAu_n^+ systems tend to delocalize an even number of electrons at least partly mediating the bond. This however depends on an interplay of the host size and the impurity nature. While the gold host cluster contributes n electrons, the number of electrons contributed by the impurity depend not only on its cationic ground state configuration, *e.g.*, the presence of a $4s$ electron, but also on the $3d^k4s^l \rightarrow 3d^{k-1}4s^{l+1}$ promotion energy. Hybridization with the gold sd-states is favored by the spatially extended $4s$ orbitals rather than the compact $3d$ orbitals. Therefore, in order to delocalize an electron the promotion energy must be rather small.
These particular boundary conditions make the size dependence in the electronic structure of transition metal (Sc,Ti,V,Cr) doped gold clusters so rich and lead to the different size dependencies of the spectral shapes.

Chapter 6

The Anderson Impurity Model in Finite Systems

In this chapter the Anderson impurity model will be put to test in finite systems. The influence of a discrete density of states of the host material on the impurity spin magnetic moment will be studied in the model system CrAu_n^+. Starting from the XMCD spectra as well as DFT calculations, the size dependence of the local spin moment of CrAu_n^+ clusters will be discussed: It turns out that the size dependence of the impurity magnetic moment essentially is in agreement with the Anderson impurity model. In order to obtain a more quantitative insight into the influence of the discretized density of states, represented by the host clusters highest-occupied–lowest-unoccupied molecular orbital (HOMO-LUMO) gap, the problem is modeled in a simple tight binding approximation indicating strong stabilization of the impurity spin magnetic moment in presence of an energy gap. The dominance of the HOMO-LUMO gap in stabilizing the impurities spin magnetic moment will be illustrated by exchanging the host material from gold to copper.

6.1 Testing the Anderson Impurity Model: A study of a Chromium Impurity in Gold-Clusters

In section 5.4 of the previous chapter the electronic structure of CrAu_n^+ was already discussed. It turned out that the chromium impurity in CrAu_n^+ $n = 2, 6$ features an undisturbed atomic-like $3d^5$ electronic configuration, while participation of the $3d$-electrons in bonding can be deduced from the spectral shapes of the x-ray absorption for the other cluster sizes.

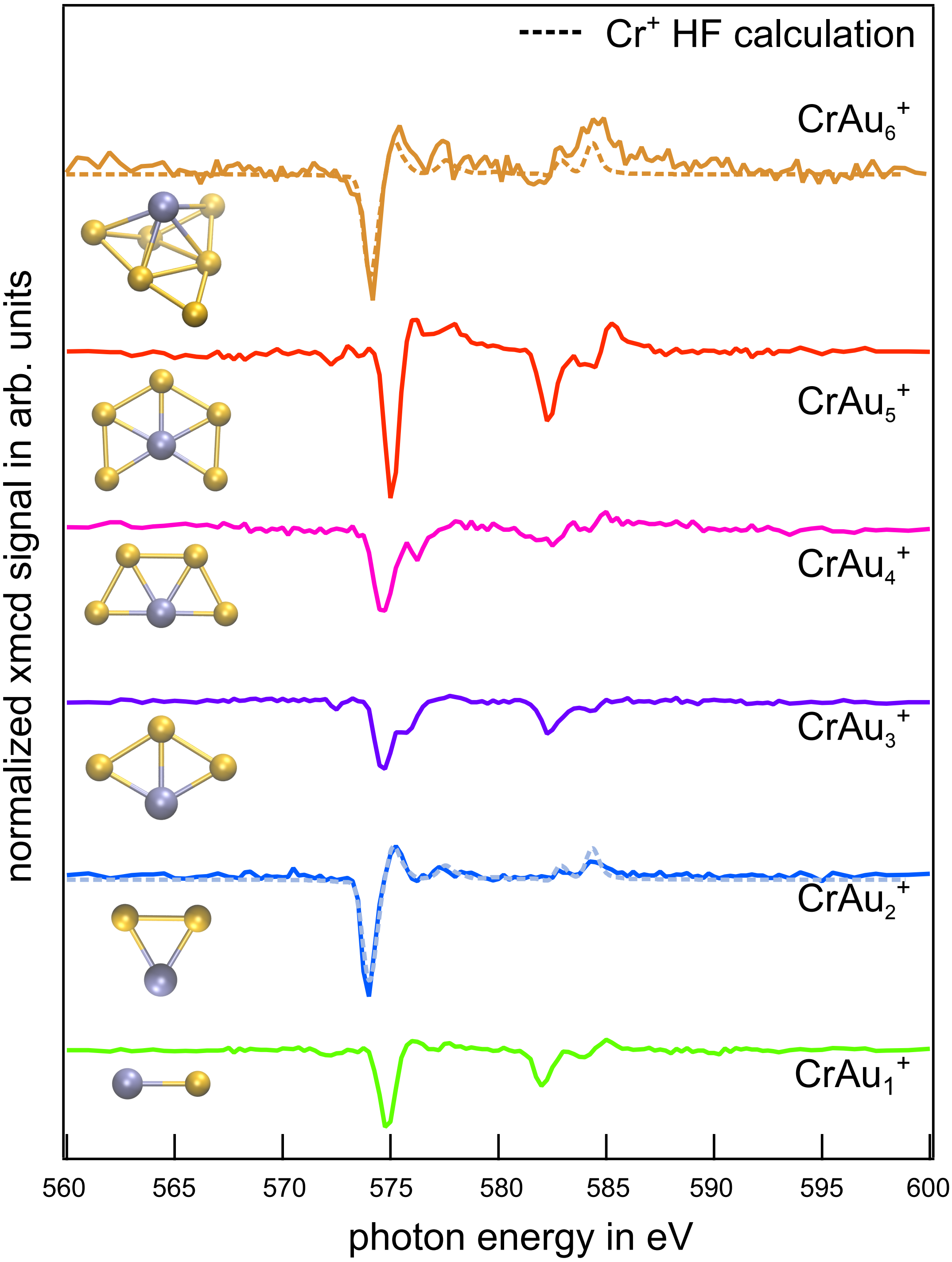

Figure 6.1: Normalized XMCD spectra of CrAu$_n^+$, $n = 1 - 6$. All spectra were taken with an energy resolution of 625 meV. Additionally, a calculated XMCD spectrum of Cr$^+$ is shown (dotted line). Structures of CrAu$_n^+$ depicted are taken from [12].

cluster	average nearest neighbor Cr-Au bond distance in Å	number of nearest neighbors
$CrAu_1^+$	2.60 Å	1
$CrAu_2^+$	2.72 Å	2
$CrAu_3^+$	2.70 Å	3
$CrAu_4^+$	2.71 Å	4
$CrAu_5^+$	2.71 Å	5
$CrAu_6^+$	2.88 Å	5

Table 6.1: Average nearest neighbor chromium-gold bond distance and number of nearest neighbors. Large distances or small number of nearest neighbors can be found for $CrAu_{2,6}^+$.

Solely from these observations, a high spin magnetic moment can be expected in $CrAu_{2,6}^+$ whereas a reduction of the spin magnetic moment should be found in the other cases, since participation of the $3d$ electrons in bonding should reduce the spin polarization.

However, the magnetic properties can be probed directly by performing x-ray magnetic circular dichroism spectroscopy. The XMCD spectra of $CrAu_n^+$ in a size range of $n = 1 - 6$ are shown in figure 6.1. Again, there is a strong resemblance of the XMCD spectra of the calculated atomic Cr^+ on the one hand and $CrAu_2^+$ and to a lesser extent for $CrAu_6^+$ on the other hand. Hence, an atomic spin moment of about $5\,\mu_B$ for $CrAu_{2,6}^+$ can directly be deduced from this comparison without using XMCD sum rules [36–38]. The application of XMCD sum rules that allow to determine spin magnetic moments is not possible, since $2p$-spin-orbit and multiplet splitting have the same order of magnitude in the case of the early $3d$ transition metal chromium, *cf.* section 2.1.3. The aforementioned atomic spin magnetic moment in $CrAu_{2,6}^+$ is also supported by DFT studies: In agreement with previous theoretical results [12] local chromium spin magnetic moments of $4.85\,\mu_B$ for $CrAu_2^+$ and $4.75\,\mu_B$ for $CrAu_6^+$ were found, as can be seen from panel (a) of figure 6.2.

The situation is different for the experimental spectra of $CrAu_{1,3-5}^+$, where no agreement with atomic Hartree-Fock calculations can be found. This suggests that the chromium $3d$ electrons participate in bonding, which leads to a reduction, but not to a quenching of the local spin moment. Non-vanishing orbital magnetic moments in $CrAu_{1,3-5}^+$, which are indicated by the negative sign of the XMCD spectra at the L_2 edges, further underline a deviation from the local $3d^5$ configuration of chromium in $CrAu_{1,3-5}^+$.

In a next step the validity of the Anderson impurity model [1] for $CrAu_n^+$ clusters will be tested. Therefore, a brief recapitulation of the size-dependence of the chromium-gold bond mechanism will be given here, because the inter-

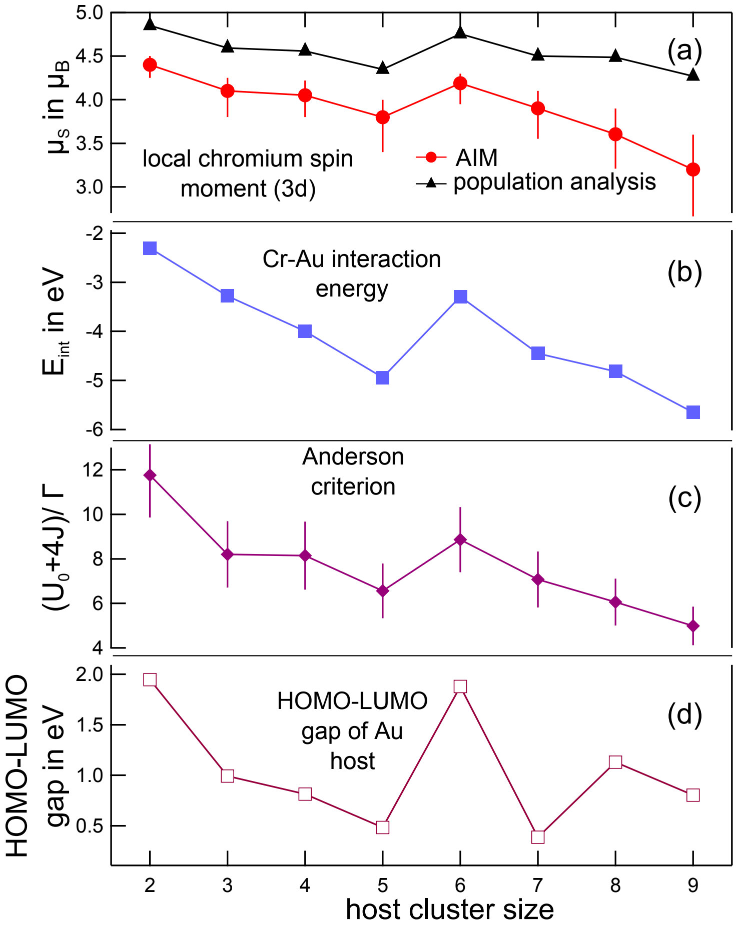

Figure 6.2: (a) Calculated local chromium spin moments μ_S of CrAu_n^+ from population analysis (black triangles) and spin moments deduced from the Anderson criterion (red bullets) presented in panel (c), (b) Cr-Au interaction energy E_{int}, (c) Anderson criterion $(U_0 + 4J)/\Gamma$, and (d) energy gap ΔE_{HL} of the gold host.

action strength of the impurity and host-material states is a crucial ingredient in the Anderson impurity model, which changes with cluster size.

The gold subunits of $\mathrm{CrAu}_{2,6}^+$, depicted in figures 5.11 and 6.1, are structurally close to pure Au_2 and Au_6 [119], *i.e.*, they remain nearly undistorted when adding the chromium impurity. In CrAu_{3-5}^+, in contrast, the number of Cr-Au bonds is maximized, and the gold host is strained and deformed as compared to its isolated, relaxed counterpart. The enhanced stability of $\mathrm{Au}_{2,6}$ stems from shell closure for two and six delocalized 6*s* electrons [119], which, in spite of strong *spd* hybridization [120], form a free electron gas confined in a two dimensional potential well [26]. Therefore, $\mathrm{Au}_{2,6}$ are known to feature large second differences in binding energy and HOMO-LUMO gaps ΔE_{HL} of about 2 eV [119]. Consequently, the chromium cation can be expected to interact more weakly in $\mathrm{CrAu}_{2,6}^+$ in comparison to the other cluster sizes. That this is indeed the case can be inferred from the chromium-gold interaction energy E_{int}, depicted in figure 6.2 (b). Here, E_{int} is calculated as

$E_{\mathrm{int}} = E\left(\mathrm{CrAu}_n^+\right) - E\left(\mathrm{Cr}^+\right) - E\left(\mathrm{Au}_n\right)$. The positive charge is mainly located at the chromium site, which can be deduced from a population analysis. This further supports the notion of electronic shell closure in the gold host of $\mathrm{CrAu}_{2,6}^+$. To obtain E_{int} and to extract the contribution of the chromium interaction with the gold cluster from the total energy, $E\left(\mathrm{Au}_n\right)$ is calculated in the same geometric configuration of Au_n as in CrAu_n^+. As expected, the weakest impurity-host interactions of 2.5 eV and 3.3 eV are found for CrAu_2^+ and CrAu_6^+, respectively.

In contrast to electronic shell closure, the coordination of the impurity atom only has a minor effect, *cf.* table 6.1. It does lead to a slight decrease of the spin magnetic moment with increasing coordination number for $n = 2$ to $n = 5$ (two-dimensional), and $n = 6$ to $n = 9$ (three-dimensional) clusters. Nonetheless, chromium in CrAu_6^+ exhibits a larger spin magnetic moment than in CrAu_3^+, although it is higher coordinated in the former, as can be seen in figures 6.1 and 6.2 (a) and from table 6.1.

We now turn to analyzing the results in terms of the Anderson impurity model [1]. In its original formulation, *cf.* section 2.5, it describes the interaction of a single orbital magnetic impurity embedded in a free electron gas. Within this model, the size of the magnetic moment of the impurity atom sensitively depends on the interplay of the on-site Coulomb repulsion (direct Coulomb interaction of two electrons in the same localized orbital) and the width 2Γ of the localized state. The width is determined by the amount of hybridization with the free electron gas states of the host and by the total density of states at the Fermi level [1]. In the absence of interaction with the free electron gas, the impurity states E and $E + U_0$ are separated by the bare Coulomb interaction U_0 that preserves the local magnetic moment if U_0 pushes the state $E + U_0$ above the Fermi level. In the case of interaction, virtual states are formed at energies $E + U_0 \cdot n_-$ and $E + U_0 \cdot n_+$, where $n_\pm$ are the occupation numbers of the impurity atom's majority and minority state. The separation of the virtual levels is reduced to an effective value $U_{\mathrm{eff}} = U_0\left(n_+ - n_-\right)$ by hybridization of the localized impurity states with free electron gas states, which also leads to an increasing width 2Γ of the virtual states [1]. Here, $\left(n_+ - n_-\right)$ is the magnetic moment of the localized state, which depends on the ratio of U_0 and Γ.

A generalization of the Anderson impurity model for a five-fold degenerate impurity state, as for $3d$-elements, predicts a transition from a magnetic to a non-magnetic impurity state for $(U_0 + 4J)/\Gamma \leq \pi$, where J is the intra-atomic exchange [128].

Therefore, quantitative insight into the impurity-host interaction can be acquired from analyzing the Anderson criterion $(U_0 + 4J)/\Gamma$. To this end,

size	1	2	3	4	5	6	7	8	9
U_0 in eV	1.68	4.00	3.15	2.91	2.92	3.80	3.26	3.43	3.46
Γ in eV	0.56	0.66	0.84	0.82	0.94	0.85	0.99	1.18	1.45

Table 6.2: Calculated on-site Coulomb repulsion U_0 and width 2Γ obtained as the weighted standard deviation of d-projected density of states of the chromium impurity.

U_{eff} was calculated in a self consistent scheme for the multi-orbital systems CrAu_n^+, which then takes the form $U_{\mathrm{eff}} = (U_0 - J)\,(n_+ - n_-)$ [72, 85]. The effective on-site Coulomb repulsion U_{eff} is derived from the slope of the linear response of the occupation number of the $3d$ impurity states to a rigid potential shift introduced at the impurity site, for details see section 2.4 or [72]. Since U_{eff} is obtained from *ab initio* calculations, the Coulomb interaction among the impurity $3d$ electrons, and all screening and hybridization effects, are intrinsically accounted for. Hence, U_0 can be determined from $U_0 = U_{\mathrm{eff}}/\,(n_+ - n_-) + J$ and is listed in table 6.2. The atomic exchange interaction of chromium $J_{\mathrm{Cr}} = 1\,\mathrm{eV}$ [127] is weakly screened, therefore J is expected to only slightly depend on the cluster size and to be of the order of 0.5-1 eV [129]. The half width Γ, *cf.* table 6.2, of the localized impurity states is obtained from the weighted standard deviation of the d-projected density of states of the impurity, which is shown in figure 6.3. The resulting values for the Anderson criterion $(U_0 + 4J)/\Gamma$, using a mean value for the exchange $J \pm \Delta J = (0.75 \pm 0.25)$ eV, are shown in figure 6.2 (c).

As can be seen the Anderson criterion for a magnetic impurity state is well satisfied throughout the whole size range, which is in perfect agreement with the non-vanishing XMCD signal for CrAu_n^+ presented in figure 6.1. In particular, a large value of the $(U_0 + 4J)/\Gamma$ is found for $\mathrm{CrAu}_{2,6}^+$, where, as was already shown, the interaction of the impurity with the host is reduced in comparison to the other cluster sizes. Although $U_0 + 4J$ exhibits a pronounced size dependence, the size-dependence of the Anderson criterion is dominated by the width of the virtual bound state, which can be related to the host clusters HOMO-LUMO gap ΔE_{HL}, *i.e.* the gap of Au_n in the geometry of CrAu_n^+, *cf.* figure 6.2. Since correlation effects are expected to be weak in the free-electron gas states of the gold host, ΔE_{HL} should be a good representation of the energy gap. In a very simple picture, the impurity state resides in the center of the host cluster's energy gap, and amount of hybridization, and therefore the width 2Γ, depends on the size of ΔE_{HL}. For example in CrAu_2^+ and CrAu_5^+, the experimentally investigated clusters with the largest and smallest magnetic moment, Γ increases from 0.66 eV to 0.94 eV whereas the energy gap ΔE_{HL} is reduced from 1.95 eV to 0.48 eV.

From the values $(U_0 + 4J)/\Gamma$ it is possible to calculate the impurity's spin magnetic moment within the Anderson impurity model by graphically solving

$$n_{\pm} = \frac{1}{\pi} \arctan\left[\frac{U_0 + 4J}{\Gamma}\left(n_{\mp} - 0.5\right)\right] + 0.5 \tag{6.1}$$

[1, 128]. As can be seen in panel (a) of figure 6.2, the size dependence of the spin magnetic moment obtained from population analysis, which is in accordance with the experimental data, shows a good qualitative and satisfying quantitative agreement with the spin magnetic moments deduced from the Anderson criterion. The deviation can mainly be attributed to the rough estimations of U_0, J and Γ. Still, the magnetic moments observed in CrAu_n^+ clusters are essentially in agreement with the Anderson impurity model. The non-linear relation in equation 6.1 also explains the small changes in the spin magnetic moments below 10 % for values of Anderson criterion $\gg \pi$, although interaction energy E_{int} and the energy gap ΔE_{HL}, strongly influencing $(U_0 + 4J)/\Gamma$, vary by more than a factor of two.

However, the good agreement of the experimental data with the Anderson impurity model is somehow surprising, since the discrete nature of the host density of states was expected to have a substantial influence on the spin magnetic moments. Presumably the good agreement is a result of the large values $(U_0 + 4J)/\Gamma$ resulting in almost full spin polarization. Therefore the presence of a gap only marginally influences the impurity spin magnetic moment. In contrast, the size of the impurity spin may benefit strongly from a gap in the host density of states in systems featuring small values $(U_0 + 4J)/\Gamma \approx \pi$. To get a more profound insight into the influence of a gap in the host density of states, the problem will be treated theoretically in the next section.

In summary, the experimentally observed size dependence of the XMCD spectra of mass selected chromium doped gold clusters are essentially well described within the Anderson impurity model. The size dependent variation of the spin magnetic moment can be linked to the hybridization strength of impurity and host density of states governed by the HOMO-LUMO gap of the host gold cluster. Electronic shell closure, resulting in large energy gaps ΔE_{HL} in the free-electron gas, reduces the interaction with the impurity and therefore results in spin magnetic moments of $5\,\mu_{\mathrm{B}}$ for $\mathrm{CrAu}_{2,6}^+$. This effect is a result of quantum confinement and unique to finite systems.

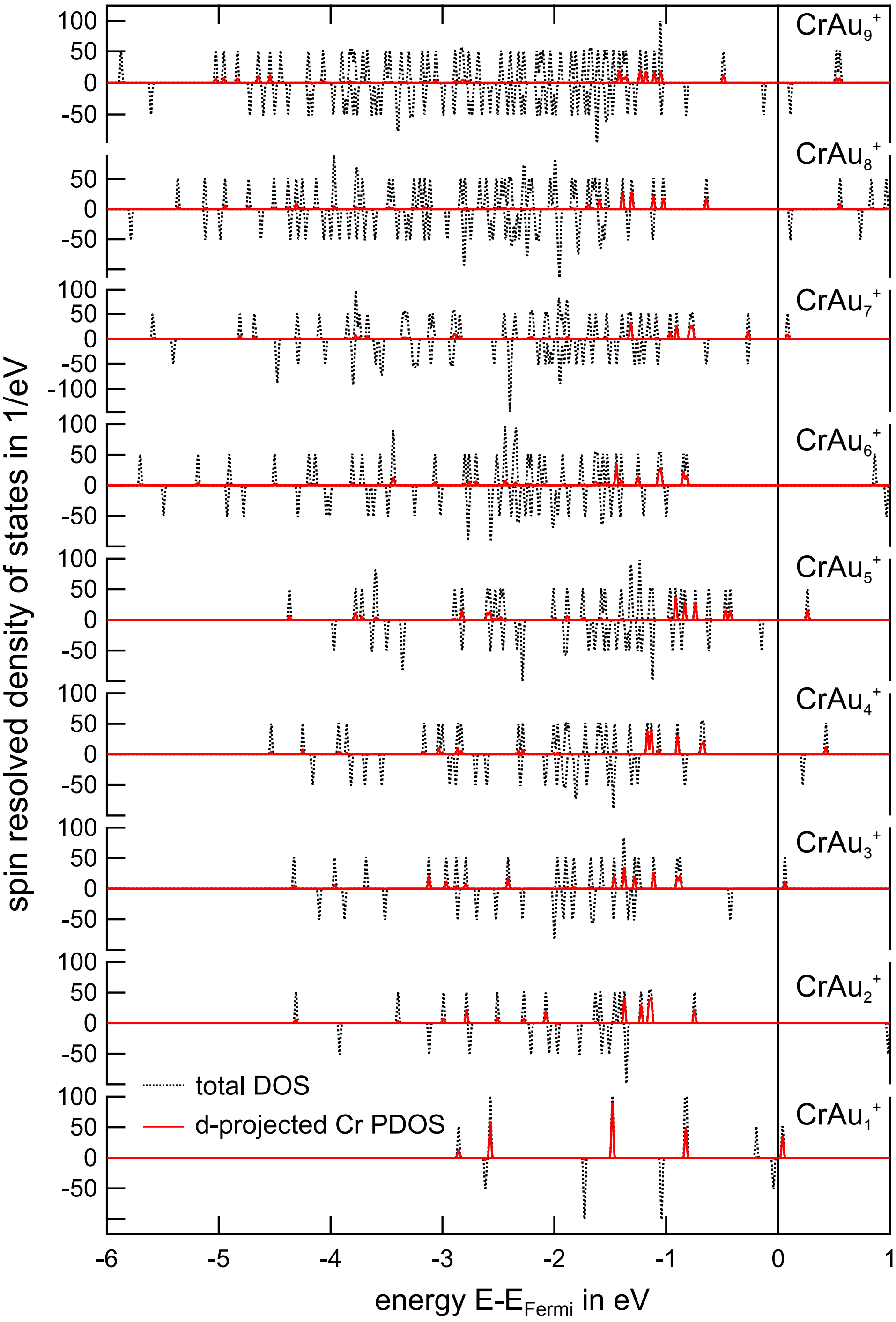

Figure 6.3: Total density of states (dotted black lines) and density of states projected onto chromium *d*-orbitals (red solid lines). Resemblance of XAS and XMCD spectra of $\mathrm{CrAu}_{2,6}^{+}$ originates in similar electronic structure obvious from the *d*-projected DOS. Positive and negative values of the density of states represent spin-up and spin-down states, respectively.

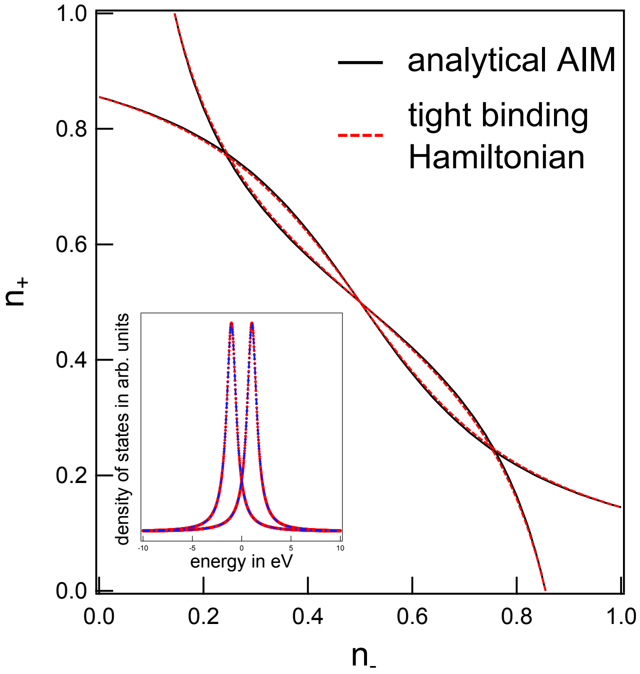

Figure 6.4: Comparison of the self-consistent solutions for the occupation numbers $n_{\pm}$ of spin-up and -down states, obtained analytically from the standard Anderson impurity model and the tight binding Hamiltonian, equation 6.2. Both models yield almost identical results. For details see the text. Inset: Density of states resulting from diagonalization of the tight binding Hamiltonian. The Lorentzian fit nicely matches the density of states.

6.2 Modification of the Anderson Impurity Model for Finite Systems

The Anderson impurity model in finite systems, also known as the Anderson box, has already been discussed intensively in the literature [130–139]. Still, none of these theoretical studies addressed the stabilization of the impurity spin magnetic moment by the discretized host density of states.

Here, this problem will be tackled by modeling the system using a tight binding Hamiltonian [140]. To this end, the following Hamiltonian will be diagonalized:

$$\mathcal{H}_{TB} = \begin{pmatrix} E_d & a & \cdots & a \\ a & E_{k,1} & 0 & 0 \\ \vdots & 0 & \ddots & 0 \\ a & 0 & 0 & E_{k,n} \end{pmatrix} \tag{6.2}$$

Here the localized impurity state E_d is coupled to a finite number of continuum states $E_{k,n}$ with a coupling strength a. The separate diagonalization for majority and minority spin states $E_d^{\pm}$ yields the spin resolved eigenvalues $\epsilon_i^{\pm}$ and eigenvectors $\phi_i^{\pm}$. The robustness of the model is tested by comparing the self-consistent solution of the occupation of the two spin states

$$n_{\pm} = \frac{1}{\pi} \arctan\left(\frac{U_0 \cdot (n_{\mp} - 0.5)}{\Gamma}\right) + 0.5 \tag{6.3}$$

within the standard Anderson impurity model [1] with the solution obtained from the tight binding Hamiltonian 6.2 by approximating the continuous band of the host by dense but discrete levels. The occupation number of the majority and minority spin states within the tight binding approximation was obtained by summation over the spin resolved density of states $\rho_{\pm}(E)$ as follows[1]:

$$\rho_{\pm}(E) = \sum_i \left|\phi_i^{\pm}\right|^2 \delta\left(E - \epsilon_i^{\pm}\right) \tag{6.4}$$

$$n_{\pm} = \int_{-\infty}^{E_F} \rho_{\pm}(E)\, dE \tag{6.5}$$

The results obtained by using a ratio of $U_0/\Gamma = 4.1$ in both cases, are almost identical as can be seen from figure 6.4. Additionally, the density of states obtained from the tight binding Hamiltonian has a Lorentzian shape as can be seen from the inset in figure 6.4. This is also what the standard Anderson model predicts. Hence, in the continuous band limit the model Hamiltonian 6.2 describes the system quite well and is equivalent to the analytical solution of the Anderson impurity model.

To study the influence of an energy gap in the host band, parameters U_0 and Γ were chosen such that the spin polarization of the impurity states vanish when interacting with the continuum states, *i.e.* $U_0/\Gamma < \pi$ in the Anderson impurity model. The relative energetic positions of impurity states and free electron gas states of the separated systems are sketched in the inset of panel (a) of figure 6.5. The self-consistent solution of spin-up and spin-down states shown in panel (c) of figure 6.5 indicates the vanishing impurity spin polarization, since the curves only cross at $n_+ = n_- = 0.5$. The absent spin polarization can also be seen from the degeneracy of the Lorentzian shaped spin-up and spin-down states formed as expected within the Anderson impurity model, *cf.* section 2.5.

However by introducing a small gap of 0.1 eV to the host density of states at the Fermi energy of the isolated host, *cf.* inset in panel (b) of figure 6.5, the majority as well as the minority spin density of states of the combined host-impurity system get poles at the Fermi energy, *cf.* panel (b) of figure 6.5. This finally leads to a non-vanishing impurity spin polarization as shown in panel (d), due to transfer of weight induced by the poles from minority spin density of states above the Fermi energy to the majority spin density of states below the Fermi energy. In addition, the curves for $n_{\pm}$ which form horizontal and vertical regions which suppress the quenching of the impurity spin moment. These curves no longer form inverse tangent functions as in the

---

[1] $\delta(E)$ is the delta function.

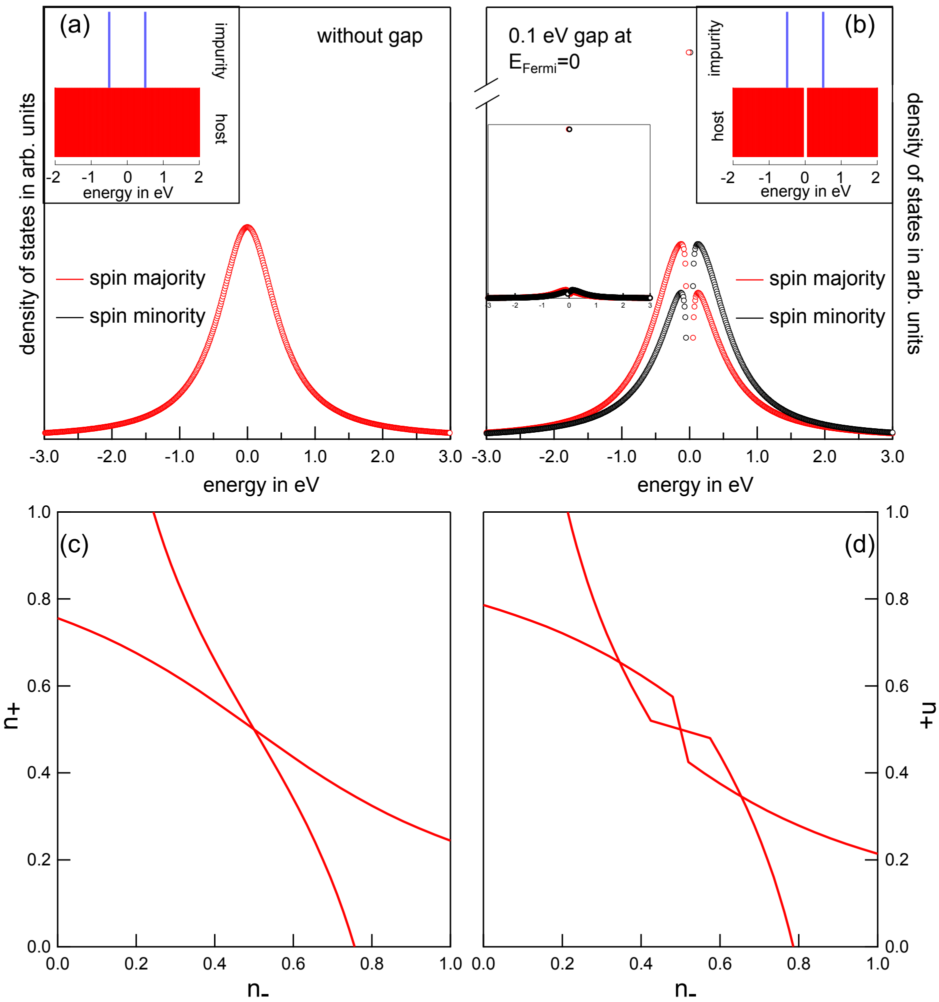

Figure 6.5: Upper panels: DOS obtained using the tight binding model Hamiltonian, equation 6.2, for an impurity interacting with a dense discrete host DOS without a gap (a) and with a gap (b). Parameters a and U_0 were kept constant. Lower panels (c) and (d) show the resulting self-consistent solution for the occupation numbers for spin-up and -down states. The impurity magnetization is restored when introducing a small gap in the host density of states, panel (d). Parameters used here: $a = 0.04\,\mathrm{eV}$, $U_0 = 1\,\mathrm{eV}$, 2000 states within a bandwidth of 20 eV.

standard Anderson impurity model.
Thus, the presence of a gap in the host density of states stabilizes the impurity's magnetic moment.

To obtain a more quantitative insight into the influence of the energy gap, the spin polarization as a function of the hosts energy gap is plotted in figure 6.6 keeping the coupling parameter a as well as the on-site Coulomb repulsion U_0 constant. As can be seen, the spin polarization adopts finite values as the

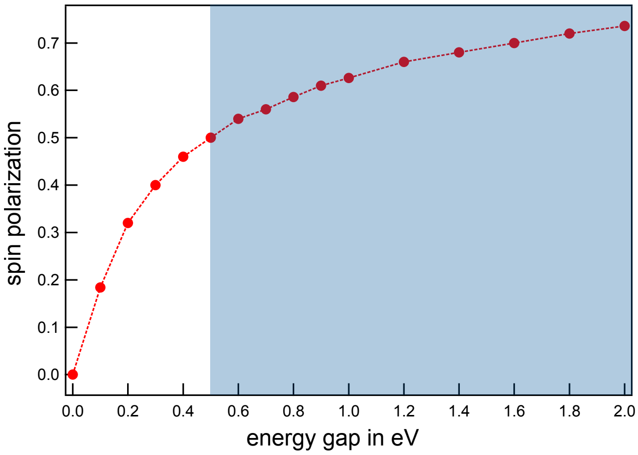

Figure 6.6: Spin polarization of the impurity as a function of the host's energy gap, keeping the coupling parameter $a = 0.08$ and the on-site Coulomb repulsion $U_0 = 2\,\text{eV}$ constant and using a host density of states of $50\,\text{states/eV}$.

hosts energy gap opens and increases rapidly. Interestingly, the spin polarization can be approximated to scale almost linearly with the host energy gap for gaps larger than $\approx 0.5\,\text{eV}$, *cf.* shaded area in figure 6.6.

In order to get a deeper insight into the influence of the hosts energy gap the spin polarization within the standard and modified Anderson impurity model will be studied as a function of the coupling strength a. This is shown in panel (a) of figure 6.7. As can be seen from the figure, only in case of very small coupling $a < 0.03\,\text{eV}$ the spin polarization is almost identical with and without the gap, whereas for larger a there is a profound deviation. Most strikingly for coupling parameters $a > 0.04\,\text{eV}$, where the spin polarization is lost in absence of an energy gap in the host materials density of states, but survives in the other case. This seems to be a quite robust effect, since even for a coupling strength a three times as large as necessary to quench the spin magnetic moment in the continuous band case, the spin is still finite in the presence of a gap.

The vanishing of the spin polarization can clearly be attributed to the strongly increasing width Γ of the virtual bound state as function of increasing coupling strength a, as depicted in figure 6.7 (b). The width was calculated as:

$$\Gamma = \frac{U_0(n_- - 0.5)}{\tan\left(\pi\left(n_- - 0.5\right)\right)},$$

following equation 6.3 and assuming charge neutrality $n_+ + n_- = 1$. In presence of a gap the Anderson description with a Lorentzian shaped virtual bound state breaks down as shown above, therefore a width Γ cannot be given in this case. Furthermore, the Anderson criterion marking the magnetic to non-magnetic transition is not valid anymore. As can be seen from figure 6.7 (c) the Anderson criterion calculated for the continuous band limit drops below π for values $a > 0.04\,\text{eV}$. Still, at these large coupling strengths which can

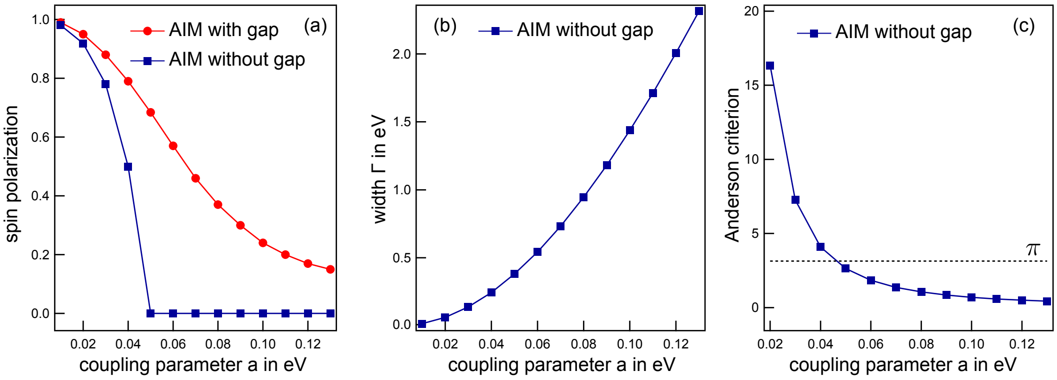

Figure 6.7: Comparison of the Anderson model and the modified version incorporating an energy gap in the host density of states ($U_0 = 1\,\text{eV}$ and $0.5\,\text{eV}$ energy gap). Panel (a): Spin polarization as a function of coupling strength a. Only for very small coupling parameters similar spin polarizations can be found. The spin magnetic moment is quenched for $a > 0.04\,\text{eV}$ in the continuous band case, whereas it survives in presence of a gap. Panel (b): Width of the virtual bound state. In absence of a gap the width increases strongly with a resulting in vanishing spin polarization for $a > 0.04\,\text{eV}$. Panel (c): Anderson criterion drops below π for coupling strengths $a > 0.04\,\text{eV}$ marking the magnetic-to-nonmagnetic transition.

be related to values $U_0/\Gamma < \pi$ in the continuous limit, the spin polarization survives in presence of a gap.

It can be expected that the influence of the gap is more pronounced for systems which are very close to the transition from magnetic to non-magnetic state in the continuous limit. Systems already exhibiting a large spin polarization in the bulk limit should be less affected by the presence of a gap in the host density of states. Still, the size of the spin magnetic moment of the impurity scales with the energy gap in the host density of states for a given coupling strength a, *cf.* figure 6.6. This is in good agreement with the experimental findings presented in the previous section 6.1, where a correlation of the magnitude of the chromium impurity spin magnetic moment and the HOMO-LUMO gap of the gold host was revealed.

Summing up, in the present section the influence of a gap on the impurity's spin magnetic moment was studied. It was shown that the presence of a gap stabilizes the impurity magnetic moment. This result is expected to hold even when the actual discrete nature of the density of states is taken into account.

6.3 Influence of the Host Material: Chromium Doped Copper Clusters

In this section experimental and theoretical results on chromium doped copper clusters will be discussed. Investigating this system will not enlarge our „stamp collection“, but helps to study the influence of varying hybridization on the magnetic moment. The use of copper as the host material is supposed to increase the hybridization of the chromium states and the host clusters free electron gas states. Enhanced hybridization is to be expected since the nearest neighbor bond distance in bulk copper is 2.56 Å [141] which is a contraction of about 10 % compared to bulk gold exhibiting a nearest neighbor bond distance of 2.88 Å [141]. Therefore a reduction of the spin magnetic moment can be anticipated.

Before studying the electronic and magnetic properties of CrCu_n^+ clusters, the next section is devoted to the ground state geometries of chromium doped copper clusters.

6.3.1 Geometries of Chromium Doped Copper Clusters

Since no structures are reported in the literature so far ground state structures for CrCu_n^+ $n = 1 - 6$ clusters have to be found for further detailed analysis. All calculations shown in this section were carried out in a DFT framework employing the PBE approximation [107] to the exchange-correlation functional as implemented in the program package TURBOMOLE 6.2 [142, 143]. The triple-ζ basis set with two polarization functions (def2-TZVPP) was used [106], which is known to yield quantitative robust results for chromium and copper [106]. Additionally, the resolution of the identity approximation [144] was used to further reduce the computational cost. The spin ground state was found by additionally introducing a thermal smearing. Here the occupation is calculated using a Fermi distribution function in every self-consistent cycle starting at a temperature of 300 K and cooling the system to 10 K in order to yield integer occupation numbers.

Different approaches were applied to generate candidate structures. In the small size regime up to a cluster size of $n = 3$ all possible arrangements of the atoms were used as candidate structures. In case of larger clusters three different methods were used: First, cluster geometries were derived from cationic copper clusters [122, 145, 146] by substitution of one copper atom by the dopant atom. Second, the gold host material in small doped gold clusters taken from literature [12] was replaced by copper. Third, a molecular dynamics simulation was performed, where the cluster freely moves at a constant temperature of 1200 K for about 10 ps. The computational effort in the molecular dynamics simulation was further reduced by using the smaller basis set def2-SVP [106]. Every 200 fs a structure snap-shot was taken and a geometry optimization was performed.

In addition, the dopant atom was placed at all non-equivalent positions in the candidate cluster which was thereupon re-optimized.

The ground state structures and the energetically next two isomers are shown in figure 6.8 together with their total spin moments. The coordinates can be found in the appendix section 8.1. As can be seen from the figure there is an early transition from two to three dimensional structures at $n = 3 \rightarrow n = 4$ different from chromium doped gold clusters, where the transition takes place at cluster sizes $n = 6-7$. Small gold clusters favor two dimensional structures because of an energy gain due to the reduction of the kinetic energy of relativistic electrons [147]. This is less important in copper and therefore three dimensional compact structures are preferred. It is obvious from figure 6.8 that the dopant atom tends to be coordinated as highly as possible. Still, the total spin magnetic moments are high: $4\,\mu_\mathrm{B}$ and $5\,\mu_\mathrm{B}$ for clusters with odd and even numbered host atoms, respectively.

The ground state structures presented here will be further analyzed in the next section.

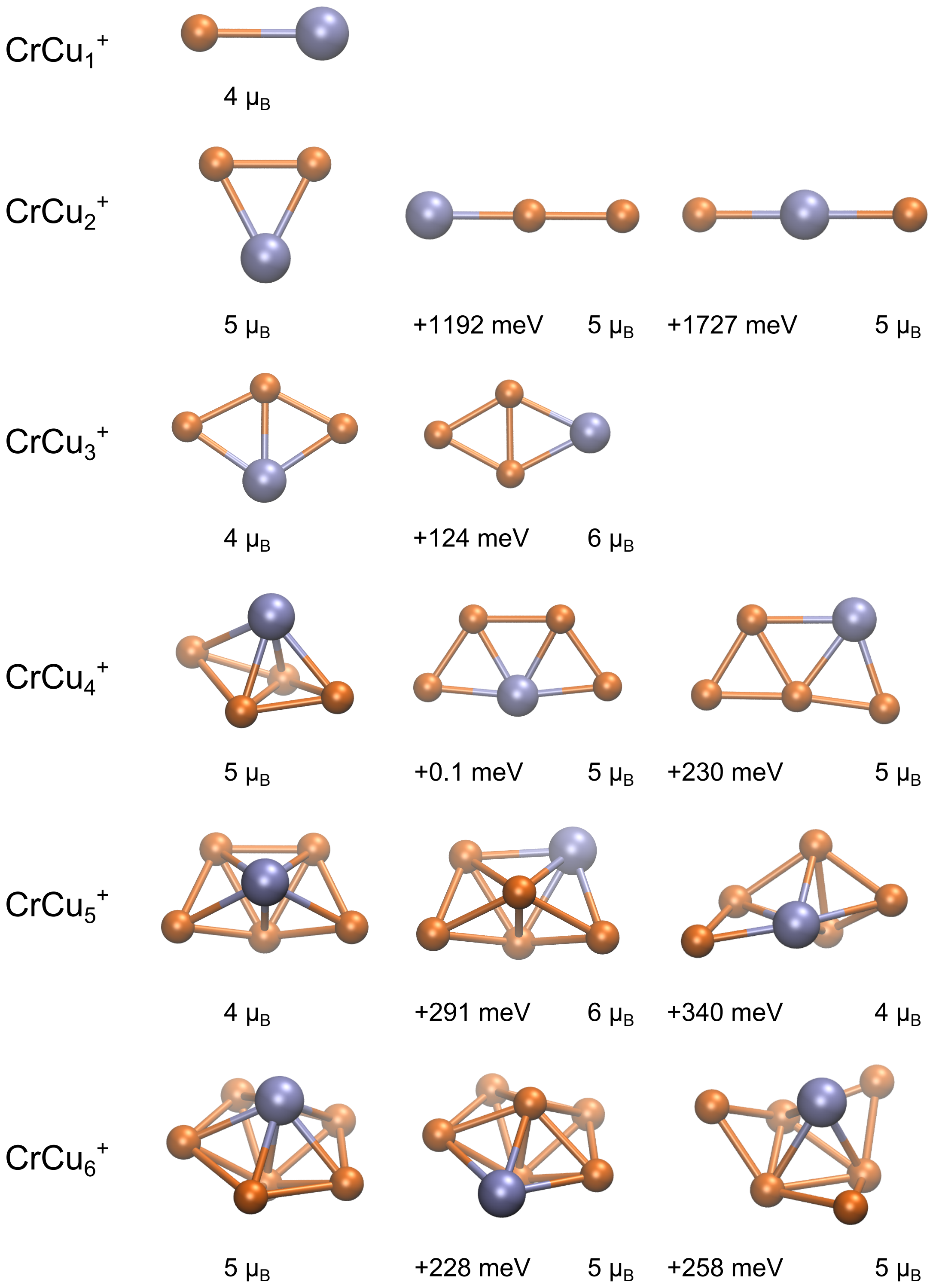
CrCu1+
4 μB
CrCu2+
5 μB
+1192 meV
5 μB
+1727 meV
5 μB
CrCu3+
4 μB
+124 meV
6 μB
CrCu4+
5 μB
+0.1 meV
5 μB
+230 meV
5 μB
CrCu5+
4 μB
+291 meV
6 μB
+340 meV
4 μB
CrCu6+
5 μB
+228 meV
5 μB
+258 meV
5 μB

Figure 6.8: Left column: Ground state geometries of CrCu_n^+ clusters in a size range $n = 1 - 6$. Chromium is shown in blue whereas copper is colored orange. Additionally shown are the two energetically lowest lying isomers. The energy is given relative to the ground state structure. The total spin moment of the clusters is also given.

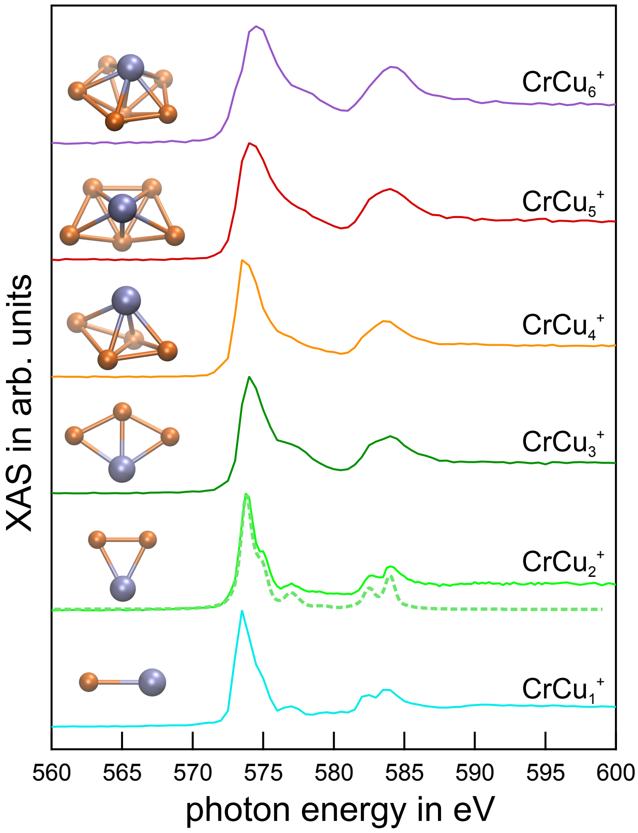

Figure 6.9: Linear x-ray absorption spectra at the $L_{2,3}$ edges of chromium of $CrCu_n^+$ in a size range $n = 1 - 6$. The energy resolution is quite low (625-1500 meV, see text for details). Additionally shown is a Hartree-Fock calculation of *atomic* Cr^+ XAS (dotted line).

6.3.2 Electronic and Magnetic Properties of Chromium Doped Copper Clusters

Linear x-ray absorption spectra of chromium doped copper clusters in a size range of $n = 1 - 6$ are presented in figure 6.9. The energy resolution is rather low compared to the x-ray absorption spectra presented in the previous sections. The energy resolution was set to 625 meV for $CrCu_2^+$, 1250 meV for $CrCu_{1,3-5}^+$ and 1500 meV for $CrCu_6^+$. Unfortunately, it was necessary to use such a low energy resolution, since the beam line was in bad condition at that particular beam time, delivering about three orders of magnitude less photons than in principle possible. Therefore the signal to noise ratio in the x-ray absorption of $CrCu_n^+$ is not improved compared to $CrAu_n^+$, although the background absorption by the host material is strongly suppressed in $CrCu_n^+$ by the relative energetic position of the chromium L-edges and the host material absorption edges in contrast to $CrAu_n^+$.

Multiplet structures could only be resolved in case of $CrCu_2^+$. A comparison to the calculated x-ray absorption spectrum of *atomic* Cr^+, *cf.* dotted line in figure 6.9, reveals a local $[Ar]3d^5$ configuration of the chromium in $CrCu_2^+$,

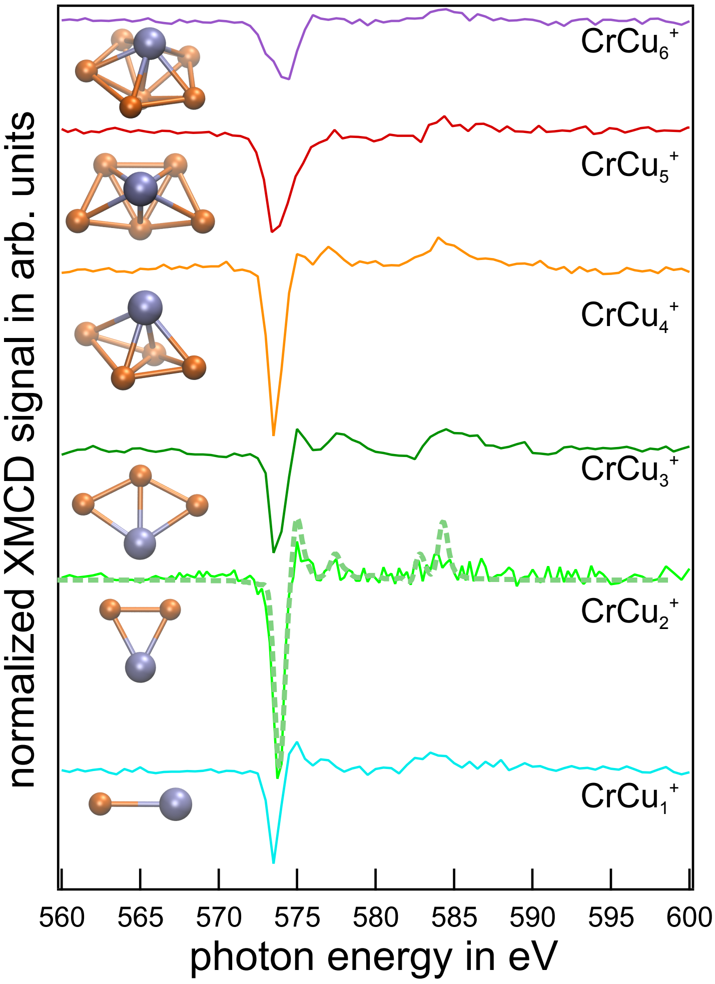

Figure 6.10: Normalized XMCD spectra at the $L_{2,3}$-edges of chromium of CrCu$_n^+$ in a size range of $n = 1-6$. A strong size dependence of the XMCD asymmetry is present. Additionally shown is a Hartree-Fock calculation of *atomic* Cr$^+$ XMCD (dotted line).

similar to the case of CrAu$_2^+$. A comparison to *atomic* Hartree-Fock calculations is not meaningful for the other cluster sizes because of the low energy resolution applied in recording the x-ray absorption spectra. Still, narrow line widths can be found in the x-ray absorption of CrCu$_{1,2,4}^+$, whereas a strong broadening is present in the x-ray absorption spectra of of CrCu$_{3,5,6}^+$. This in turn suggests a stronger hybridization of the chromium 3*d*-states with the host clusters electronic states in CrCu$_{3,5,6}^+$ than in CrCu$_{1,2,4}^+$. Hence, reduced spin magnetic moments should be found for CrCu$_{3,5,6}^+$. Because larger hybridization leads to a smaller separation of the virtual states formed in the system and to a transfer of electrons from majority to minority spin states, *cf.* section 6.1, this again results in a reduced spin magnetic moment.

In order to directly study the magnetic properties of chromium doped copper clusters XMCD spectroscopy was performed. The normalized XMCD spectra taken at a constant temperature of (20 ± 5) K are shown in figure 6.10. As

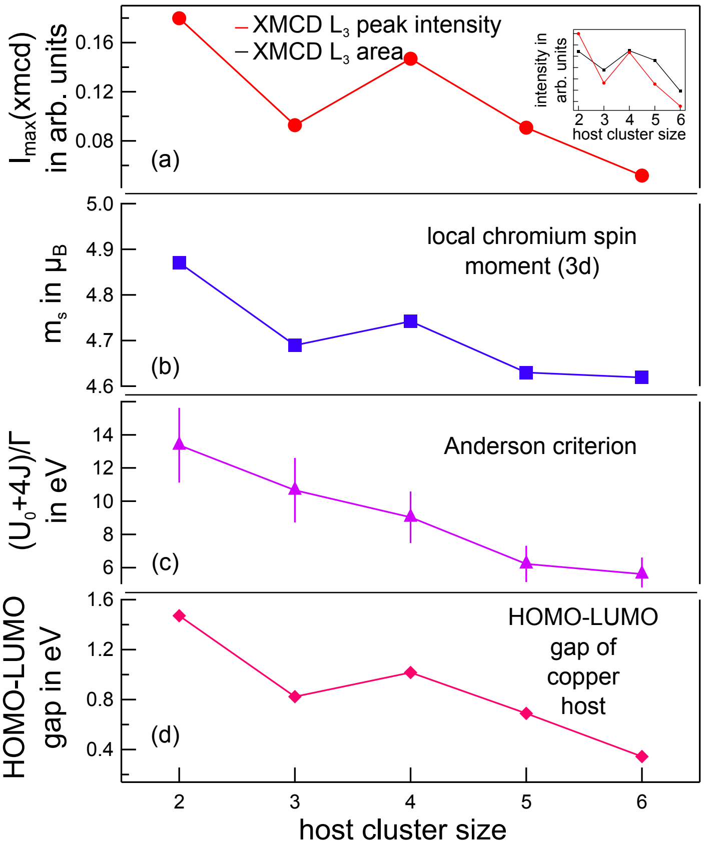

Figure 6.11: Panel (a): Maximum intensity at the L_3-edge of the XMCD asymmetry as a function of cluster size. In the inset a comparison of the maximum intensity and the area A (see text for details) is given, showing the same size dependent trend. Panel (b): Local chromium spin moments obtained from DFT+U calculations. Panel (c): $(U_0 + 4J)/\Gamma$ is larger than π for all cluster sizes and fulfill therefore the Anderson criterion for a magnetic impurity state [1]. Panel (d): The host clusters HOMO-LUMO gap exhibiting the same size dependence as the impurity spin magnetic moment.

in linear x-ray absorption a resemblance of the calculated XMCD signal of *atomic* Cr^+ and the XMCD spectrum of CrCu_2^+ exists, indicating a local spin magnetic moment of about $5\,\mu_\mathrm{B}$. Furthermore, a strong size dependence of the magnitude of the XMCD asymmetry can be found, *cf.* figure 6.10. The spin magnetic moment m_S is proportional to $m_S \propto A - 2 \cdot B$ [2], A being the area at the L_3 and B the area at the L_2 edge of the asymmetry signal. Since the area B is negligibly small in case of chromium doped copper clusters, the spin magnetic moment is mainly given by the area A. Here we can even use the maximum intensity at the L_3-edge of the XMCD asymmetry, since the area of the XMCD asymmetry at the L_3 edge is very narrow and because of the low energy resolution used the peak intensity mainly covers the whole area A. A comparison of the area A and the peak intensity at the L_3-edge of the XMCD signal is given in the inset of figure 6.11 exhibiting almost the same size dependent trend. As already expected from the line shapes in linear x-ray absorption, a large XMCD asymmetry signal, which is, in this particular case, proportional to the local chromium spin magnetic moment, can be found in

---

[2] This is basically the XMCD spin sum rule, *cf.* section 2.1.3.

cluster	average nearest neighbor Cr-Cu bond distance in Å	number of nearest neighbors
$CrCu_1^+$	2.74 Å	1
$CrCu_2^+$	2.58 Å	2
$CrCu_3^+$	2.57 Å	3
$CrCu_4^+$	2.64 Å	4
$CrCu_5^+$	2.65 Å	5
$CrCu_6^+$	2.63 Å	6

Table 6.3: Average nearest neighbor chromium-copper bond distance and number of nearest neighbors in $CrCu_n^+$.

case of $CrCu_{2,4}^+$.

A reasonable agreement in the size dependence of the calculated local chromium spin moments (within a DFT framework), obtained from projecting the total density of states onto chromium *d*-states, shown in panel (b) of figure 6.11, with the measured XMCD asymmetry, displayed in panel (a) of the same figure, can be found. In order to study the influence of the host material, the size dependence of the spin magnetic moment of $CrCu_n^+$ and $CrAu_n^+$ will be compared. By analyzing figures 6.2 and 6.11 it is immediately clear that the size dependent trend of the spin magnetic moment of $CrCu_n^+$ is very different from $CrAu_n^+$. The only agreement can be found for clusters exhibiting the same overall geometry, namely $CrCu_2^+$ and $CrCu_3^+$.

The spin magnetic moments as well as the Anderson criterion are almost identical for $CrCu_3^+$ ($m_S = 4.67\,\mu_\mathrm{B}$, $(U_0 + 4J)/\Gamma) = 10.7$) and $CrAu_3^+$ ($m_S = 4.59\,\mu_\mathrm{B}$, $(U_0 + 4J)/\Gamma) = 8.2$), *cf.* figures 6.2 and 6.11. The small deviation of the spin magnetic moments in $CrCu_3^+$ compared to $CrAu_3^+$ is, at first glance, remarkable, since the average bond distance in $CrCu_3^+$ is contracted by about 5 % compared to $CrAu_3^+$, *cf.* tables 6.1 and 6.3. The contraction of the bond distance entails a larger overlap of the impurity and host valence electron wave-functions and should scale exponentially. Therefore a larger hybridization would be expected in case of the chromium doped copper clusters. The same contraction of the Cr-Cu bond distances can be found in $CrCu_2^+$, again not altering the electronic and magnetic properties of the chromium atom in the $CrCu_2^+$ cluster compared to $CrAu_2^+$. This of course becomes manifest in their density of states which are compared in figure 6.12. As can be seen the chromium 3*d*-states are equally undistorted in both systems. The main difference is the relative energetic position of the chromium 3*d*-states and the *sd*-states of the host, which are basically changing positions.

As can be seen from figure 6.11, the impurity spin magnetic moment of $CrCu_n^+$

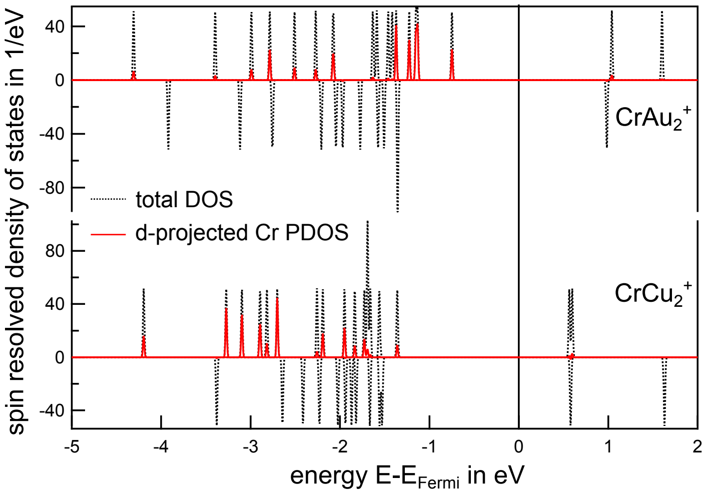

Figure 6.12: Comparison of the density of states of $CrCu_2^+$ and $CrAu_2^+$. The chromium $3d$-states exhibit a similar undistorted structure. The energetic position of chromium $3d$-states and host sd-states are interexchanged from $CrCu_2^+$ to $CrAu_2^+$.

scales with the HOMO-LUMO gap in the host density of states. This was already shown in section 6.1 for $CrAu_n^+$ clusters and in general for systems exhibiting a gap in section 6.2.

Hence, increasing the hybridization induced by *geometrical* changes, for example bond distance contraction, is of minor importance for the size dependence of the impurity's spin magnetic moment, at least in the parameter regime of $(U_0 + 4J)/\Gamma$ we are investigating here. The size dependence is rather dominated by electronic shell closure in the host material, determining the size of the HOMO-LUMO gap. For that reason one finds almost identical spin magnetic moments in $CrCu_2^+$ and $CrAu_2^+$. The two $4s$ electrons of the copper host form a two dimensional electron gas [148, 149]. This results in a large HOMO-LUMO gap, comparable to the case of $CrAu_2^+$, yielding a reduced width of the virtual bound state and therefore an almost identical value of $(U_0 + 4J)/\Gamma$, although the Cr-Cu bond distance is contracted by about 5 % compared to the Cr-Au bond distances.

This observation is in agreement with the line widths found in x-ray absorption and XMCD spectra as discussed above. The reduced (enhanced) spectral width in $CrCu_{2,4}^+$ ($CrCu_{3,5,6}^+$) originate from the sizable (small) HOMO-LUMO gaps in the host material density of states, *cf.* panel (d) of figure 6.11 (in agreement with [150, 151]).

The magnetic moments in $CrCu_n^+$ clusters in the investigated size regime clearly exceed $4\,\mu_B$, which is considerably larger than magnetic moments of $3\,\mu_B$ [152–154] predicted for chromium embedded in a bulk copper sample. The reduction of the moment in bulk copper can have multiple reasons. The most obvious is the reduction of spin due to stronger hybridization caused by the absence of a gap in bulk copper. Additionally, the coordination number of CrCu_n^+ clusters linearly increases with the cluster size and has a maximum value of 6 in CrCu_6^+. However, assuming a chromium impurity in fcc bulk copper to favor a substitutional site, its coordination number would be as high as 12. This increase in coordination in comparison to the small clusters probably results in a stronger hybridization of the chromium $3d$ states with the copper $4s$ derived band. This would in turn lead to a reduced chromium impurity spin polarization. Also the cationic nature of the clusters may enhance the spin moment. The excess charge in the bulk material could conceivably lead to a reduction of the spin polarization by placing the extra electron in the $3d$-states of the impurity, which would reduce the spin by $1\,\mu_\mathrm{B}$.

6.4 Summary

In this chapter the applicability of the Anderson impurity model to finite systems was studied experimentally and theoretically. The experimental data taken for chromium doped gold clusters are essentially in agreement with the standard Anderson impurity model, since the Anderson criterion is rather large in these systems. Therefore CrAu_n^+ clusters are far above the magnetic to non-magnetic transition threshold, so the discrete nature of the host density of states has only minor consequences. Still, it could be shown that the size of the HOMO-LUMO gap in the host influences the magnitude of the impurity spin magnetic moment. This was further studied using a tight binding model Hamiltonian. It could be shown that not only the description within the Anderson impurity model breaks down, but also that in a certain parameter regime the size of the gap in the host density of states scales almost linearly with the impurity spin magnetic moment, which is again in agreement with the experimental findings. Moreover, significant stabilization of the spin magnetic moment by the presence of an energy gap in the host density of states for values of the Anderson criterion close to the magnetic to non-magnetic transition was demonstrated. By substituting the host material from gold to copper the importance of shell closure effects determining the size of the HOMO-LUMO gap for the host-impurity interaction could be revealed.

Chapter 7

Epilogue

7.1 Summary

In this thesis the interaction of a single magnetic impurity embedded in a finite non-magnetic host, exhibiting a highly discretized density of states, was studied experimentally as well as theoretically. Gold clusters doped with early $3d$-transition metals (scandium through chromium) served as model systems. By performing the experiment in the gas phase not only any support or impurity-impurity interaction was eliminated which allows to study the intrinsic properties of the system but a discretized density of states of the host material is introduced very natural by quantum confinement.

It was shown that the local electronic structure of the impurity depends on a complex interplay of the nature of the dopant element as well as on cluster size dependent quantum confinement in the host rather than on simple impurity coordination. However, a strong tendency of all investigated systems to delocalize an even number of electrons, when allowed by the boundary conditions, was found. This was inferred from x-ray absorption spectroscopy combined with density functional theory calculations.

In case of chromium doped gold clusters also the magnetic properties were probed by applying XMCD spectroscopy. The results were discussed within the Anderson impurity model [1]. Introducing an impurity with sufficiently localized valence orbitals into the non-magnetic host leads to the formation of virtual bound states. Two parameters and their relative sizes are essential in the Anderson impurity model for determining if the impurity retains its spin degree of freedom. These are for one the on-site Coulomb repulsion U_0, which is the energy necessary to add an electron to a localized orbital and secondly the width Γ of the virtual bound state caused by hybridization of the localized impurity orbitals and the electronic states of the itinerant electrons of the host material. In case of a single impurity orbital, the system undergoes a magnetic to non-magnetic transition if $U_0/\Gamma = \pi$. Since the Anderson impurity model was developed for bulk materials, severe deviations could be expected in finite systems.

Surprisingly, it was found that the Anderson impurity model is essentially in agreement with the experimental data. This agreement can be attributed to the overall large values of $U_0/\Gamma \gg \pi$ in case of CrAu_n^+, which leads to almost full spin polarization. Therefore, the highly discretized density of states in the host has only a minor influence on the impurity spin, namely scaling it as a function of the hosts energy gap. This was confirmed by exchanging the host material from gold to copper.

In order to get a more profound insight into the influence of the gap, the problem was studied within tight binding approximation. It turned out that the presence of a gap in the host density of states can substantially stabilize the impurity's magnetic moment. This is especially true for systems approaching the magnetic to non-magnetic transition, *i.e.* the parameter regime $U_0/\Gamma \approx \pi$. In this parameter regime, the description within the standard Anderson impurity model breaks down and magnetic states can also be found for values $U_0/\Gamma < \pi$.

7.2 Outlook

Although the treatment of finite systems within tight binding approximation already yields significant insight, the model should be extended to multiple orbitals in order to get a more quantitative description of the impurity-host interaction. To test this model in a quantitative manner, XMCD spectroscopy should be applied to FeAu_n^+, CoAu_n^+ and NiAu_n^+ for which the XMCD sum rules hold.

Furthermore, the size dependence of the spin of the magnetic impurity of Fe, Co, Ni in Au_n can be expected to be different from that of Cr in CrAu_n^+ clusters. That is because the on-site Coulomb repulsion U_0 varies along the $3d$-transition metal series, as does the hybridization of host and impurity electronic states. The dopant-host interaction in CrAu_n^+ clusters is reduced by shell closure in the gold host as well as the highly stable half filled valence shell of Cr^+ (^6S state). Valence states of Fe, Co, Ni are less stable, as can be inferred from their lower $3d - 4s$ promotion energy [155, 156]. It can be assumed that this brings the system closer to the magnetic to non-magnetic transition. In the regime close to the transition, the influence of the highly structured density of states in the host material should be more pronounced than in the almost fully spin polarized case of CrAu_n^+ clusters. This should lead to a strong size dependence of the magnetic moments, potentially with complete quenching of the moments for certain sizes. Hence, deviations from the bulk Anderson impurity model are supposed to be more distinct in FeAu_n^+, CoAu_n^+ and NiAu_n^+.

The presented data is a first step towards the experimental investigation of a Kondo effect in a finite system which is expected to differ considerably from its bulk counterpart. This is because the scattering processes in the Kondo effect involve states near the Fermi level in the energy range of $k_B T_K$. Therefore, it is natural to assume that the Kondo effect should be strongly altered in finite systems where the mean level spacing Δ becomes comparable to the energy scale $k_B T_K^{bulk}$.

Indeed, several theoretical publications point out the implications of the mean level spacing Δ. For instance, a partitioning of the Kondo resonance is predicted, which is different for odd and even numbers of electrons in the host material [138]. Also non-vanishing values of the susceptibility χ at low temperatures are found [130].

In principle the latter effect should be accessible by temperature dependent magnetization curves obtained from XMCD spectroscopy. However, even without extracting the exact values of the susceptibility χ the formation of a Kondo state should be observable by the deviation of a temperature dependent Brillouin-like magnetization curve. The spin polarization of the host material is even more easily to access. Above the Kondo temperature T_K no spin polarization is present in the host electron gas assuming an even number of electrons. Below T_K, upon formation of the low spin state, the itinerant electrons get spin polarized. This can possibly be observed if the impurity is underscreened, *i.e.* the number of itinerant electrons in the host is not sufficient to fully screen the localized impurity spin, because this in turn yields a finite alignment in an external magnetic field necessary to detect a dichroic signal. The unambiguous signature of the Kondo effect would then be the appearance of an antiferromagnetic coupling of impurity and host electrons spins below the Kondo temperature T_K. From a spectroscopic point of view copper would be a perfect host material due to its nicely structured x-ray absorption signal at the $L_{2,3}$-edges [32], which in turn allows to probe the spin polarization of the $4s$-derived free electron gas states.

The investigation of a Kondo effect in a finite system has thus come into reach. It would open up new paths for experimental many-body physics and promises new physical insight into an old problem of condensed matter physics: the scattering of electrons at a magnetic impurity.

List of publications

1. **K. Hirsch**, V. Zamudio-Bayer, A. Langenberg, M. Niemeyer, B. Langbehn, T. Möller, A. Terasaki, B. v. Issendorff, and J. T. Lau, *Magnetic Moments of Chromium-Doped Gold Clusters: The Anderson Impurity Model in Finite Systems*, in preparation.

2. V. Zamudio-Bayer, L. Leppert, **K. Hirsch**, A. Langenberg, J. Rittmann, M. Kossick, M. Vogel, R. Richter, A. Terasaki, T. Möller, B. v. Issendorff, S. Kümmel, and J. T. Lau, *Coordination-driven magnetic-to-nonmagnetic transition in manganese doped silicon clusters*, submitted to Phys. Rev. Lett.

3. **K. Hirsch**, V. Zamudio-Bayer, J. Rittmann, A. Langenberg, M. Vogel, B. v. Issendorff, and J. T. Lau, *Initial- and final-state effects on screening and branching ratio in 2p x-ray absorption of size-selected free 3d transition metal clusters*, Phys. Rev. B 86, 165402 (2012).

4. **K. Hirsch**, V. Zamudio-Bayer, F. Ameseder, A. Langenberg, J. Rittmann, M. Vogel, T. Möller, B. v. Issendorff, and J. T. Lau, *2p x-ray absorption of free transition-metal cations across the 3d transition elements: Calcium through copper*, Phys. Rev. A 85, 062501 (2012).

5. M. Niemeyer, **K. Hirsch**, V. Zamudio-Bayer, A. Langenberg, M. Vogel, M. Kossick, C. Ebrecht, K. Egashira, A. Terasaki, T. Möller, B. von Issendorff, and J. T. Lau, *Spin Coupling and Orbital Angular Momentum Quenching in Free Iron Clusters*, Phys. Rev. Lett. 108, 057201 (2012).

6. M. Vogel, C. Kasigkeit, **K. Hirsch**, A. Langenberg, J. Rittmann, V. Zamudio-Bayer, A. Kulesza, R. Mitri, T. Möller, B. v. Issendorff, and J. T. Lau, *2p core-level binding energies of size-selected free silicon clusters: Chemical shifts and cluster structure*, Phys. Rev. B 85, 195454 (2012).

7. J. T. Lau, M. Vogel, A. Langenberg, **K. Hirsch**, J. Rittmann, V. Zamudio-Bayer, T. Möller, and B. von Issendorff, *Communication: Highest occupied molecular orbital-lowest unoccupied molecular orbital gaps of doped silicon clusters from core level spectroscopy*, J. Chem. Phys. 134, 041102 (2011).

8. J. T. Lau, **K. Hirsch**, P. Klar, A. Langenberg, F. Lofink, R. Richter, J. Rittmann, M. Vogel, V. Zamudio-Bayer, T. Möller, and B. von Issendorff, *X-ray spectroscopy reveals high symmetry and electronic shell structure of transition-metal-doped silicon clusters*, Phys. Rev. A 79, 053201 (2009).

9. J. T. Lau, **K. Hirsch**, A. Langenberg, J. Probst, R. Richter, J. Rittmann, M. Vogel, V. Zamudio-Bayer, T. Möller, and B. von Issendorff, *Localized high spin states in transition-metal dimers: X-ray absorption spectroscopy study*, Phys. Rev. B 79, 241102 (2009).

10. **K. Hirsch**, J. T. Lau, P. Klar, A. Langenberg, J. Probst, J. Rittmann, M. Vogel, V. Zamudio-Bayer, T. Möller, and B. von Issendorff, *X-ray spectroscopy on size-selected clusters in an ion trap: from the molecular limit to bulk properties*, J. Phys. B: At. Mol. Opt. Phys. 42, 154029 (2009).

11. J. T. Lau, J. Rittmann, V. Zamudio-Bayer, M. Vogel, **K. Hirsch**, P. Klar, F. Lofink, T. Möller, and B. von Issendorff, *Size Dependence of $L_{2,3}$ Branching Ratio and 2p Core-Hole Screening in X-Ray Absorption of Metal Clusters*, Phys. Rev. Lett. 101, 153401 (2008).

List of Figures

2.1 Radial probability of $2p$ and $3d$ wave functions for atomic number $Z = 23$. 14
2.2 Transition probabilities for L_3-edge excitation with circular polarized light. 15
2.3 Accessible m_L subsets in a dipole transition at the $L_{2,3}$-edges. 15
2.4 Comparison of fluorescence and Auger yield at the $L_{2,3}$ edges as a function of the atomic number Z. 17
2.5 Kmetko-Smith diagram. 18
2.6 Mott transition as a function of U/W 19
2.7 Schematic illustration of the total energy as a function of occupation numbers. 23
2.8 Linear response function for the screened and bare system to obtain on-site Coulomb repulsion U_0. 24
2.9 Schematic illustration of the Anderson impurity model. 26
2.10 Self consistent solution within the Anderson impurity model for the occupation numbers $n_\pm$ of spin-up and spin-down state. . 27
2.11 Feynman diagram of the Kondo scattering process. 28

3.1 Schematic view of the experimental setup for XMCD spectroscopy. 32
3.2 Magnetization as a function of temperature and external magnetic field shown for a particle with $J = S = 5/2$. 33
3.3 Variation of the magnetic field of the solenoid magnet along the magnets symmetry axis. 34
3.4 Sectional view of the ion trap. 35
3.5 Sketch of an undulator and electron bunch trajectories. 36

4.1 Preparation of measurement: Mass spectra. 40
4.2 Schematic of the data acquisition cycle. 41
4.3 Background subtraction in x-ray absorption spectra. 42
4.4 Data processing of XMCD asymmetries. 43
4.5 Convergence test for the density functional theory calculations. 44

5.1 Linear XAS of ScAu_n^+ $n = 1 - 6$ at the scandium $L_{2,3}$ edges. . 47
5.2 DOS and PDOS of ScAu_n^+ clusters. 48
5.3 Population analysis of the scandium $3d$-orbitals in ScAu_n^+ clusters. 49
5.4 Linear XAS of TiAu_n^+ $n = 1 - 9$ at the titanium $L_{2,3}$ edges. . . 50
5.5 Löwdin population analysis of TiAu_n^+ clusters. 51
5.6 DOS and PDOS of TiAu_n^+ clusters, $n = 1 - 9$. 52
5.7 X-ray absorption onset of TiAu_n^+ clusters. 53
5.8 Linear XAS of VAu_n^+ $n = 1 - 7$ at the vanadium $L_{2,3}$ edges. . . 56
5.9 Total and spin resolved $3d$ occupation of VAu_n^+ clusters in a size range of $n = 1 - 7$. 57
5.10 Density of states of VAu_n^+ clusters, $n = 1 - 7$. 58
5.11 Linear XAS of CrAu_n^+ $n = 1 - 8$ at the chromium $L_{2,3}$ edges. . 60
5.12 Size dependent absorption onset in the x-ray absorption of CrAu_n^+ clusters. 61

6.1 Normalized XMCD spectra of CrAu_n^+, $n = 1 - 6$. 64
6.2 Local magnetic moment, chromium-gold interaction energy, Anderson criterion and gold HOMO-LUMO gap for CrAu_n^+ clusters. 66
6.3 Total and d-projected density of states of CrAu_n^+ clusters, $n = 1 - 9$. 70
6.4 Comparison of the self-consistent solutions for the occupation numbers from the analytical Anderson impurity model and in tight binding approximation. 71
6.5 DOS of a finite system obtained from Hamiltonian in tight bind approximation. 73
6.6 Comparison of the Anderson impurity model for continuous and discrete host density of states. 74
6.7 Comparison of spin polarization for the Anderson impurity model with and without gap. 75
6.8 Geometries of CrCu_n^+ clusters in a size range $n = 1 - 6$. 78
6.9 Linear x-ray absorption spectra at the $L_{2,3}$ edges of chromium of CrCu_n^+ in a size range $n = 1 - 6$. 79
6.10 Normalized XMCD spectra at the $L_{2,3}$-edges of chromium of CrCu_n^+ in a size range of $n = 1 - 6$. 80
6.11 Maximum intensity at the L_3-edge of the XMCD asymmetry, local chromium spin magnetic moment, Anderson criterion and HOMO-LUMO gap of the copper host of CrCu_n^+ clusters. . . . 81
6.12 Comparison of the density of states of CrCu_2^+ and CrAu_2^+. . . 83

List of Tables

3.1 Technical specification of the undulator beam lines U49-2-PGM and UE52-SGM. 36

6.1 Average nearest neighbor chromium-gold bond distance and number of nearest neighbors in CrAu_n^+ clusters. 65
6.2 Calculated on-site Coulomb repulsion U_0 and width 2Γ for CrAu_n^+ clusters. 68
6.3 Average nearest neighbor chromium-copper bond distance and number of nearest neighbors in CrCu_n^+. 82

Bibliography

[1] P. W. Anderson, “Localized Magnetic States in Metals”, Phys. Rev. **124**, 41 (1961).

[2] J. Friedel, “Metallic alloys”, Il Nuovo Cimento **7**, 287 (1958).

[3] A. Blandin and J. Friedel, “Proprietes magnetiques des alliages dilues - interactions magnetiques et antiferromagnetisme dans les alliages du type metal noble-metal de transition.”, J. Phys. Radium **20**, 160 (1959).

[4] J. Kondo, “Resistance Minimum in Dilute Magnetic Alloys”, Progr. Theoret. Phys. **32**, 37 (1964).

[5] P. Gambardella, S. S. Dhesi, S. Gardonio, C. Grazioli, P. Ohresser, and C. Carbone, “Localized Magnetic States of Fe, Co, and Ni Impurities on Alkali Metal Films”, Phys. Rev. Lett. **88**, 047202 (2002).

[6] C. Carbone, M. Veronese, P. Moras, S. Gardonio, C. Grazioli, P. H. Zhou, O. Rader, A. Varykhalov, C. Krull, T. Balashov, A. Mugarza, P. Gambardella, S. Lebèque, O. Eriksson, M. I. Katsnelson, and A. I. Lichtenstein, “Correlated Electrons Step by Step: Itinerant-to-Localized Transition of Fe Impurities in Free-Electron Metal Hosts”, Phys. Rev. Lett. **104**, 117601 (2010).

[7] P. Wahl, L. Diekhöner, M. A. Schneider, L. Vitali, G. Wittich, and K. Kern, “Kondo Temperature of Magnetic Impurities at Surfaces”, Phys. Rev. Lett. **93**, 176603 (2004).

[8] J. Li, W.-D. Schneider, R. Berndt, and B. Delley, “Kondo Scattering Observed at a Single Magnetic Impurity”, Phys. Rev. Lett. **80**, 2893 (1998).

[9] N. Néel, J. Kröger, R. Berndt, T. O. Wehling, A. I. Lichtenstein, and M. I. Katsnelson, “Controlling the Kondo Effect in CoCu_n Clusters Atom by Atom”, Phys. Rev. Lett. **101**, 266803 (2008).

[10] S. M. Cronenwett, T. H. Oosterkamp, and L. P. Kouwenehoven, “A Tunable Kondo Effect in Quantum Dots”, Science **281**, 540 (1998).

[11] D. Goldhaber-Gordon, H. Shtrikman, D. Mahalu, D. Abusch-Magder, U. Meirav, and M. A. Kastner, "Kondo effect in a single-electron transistor", Nature **391**, 156 (1998).

[12] M. B. Torres, E. Fernández, and L. Balbás, "Theoretical study of structural, electronic, and magnetic properties of $\mathrm{Au}_n\mathrm{M}^+$ clusters (M=Sc, Ti, V, Cr, Mn, Fe, Au; $n = 1-9$)", Phys. Rev. B **71**, 155412 (2005).

[13] H. Häkkinen, S. Abbet, A. Sanchez, U. Heiz, and U. Landman, "Structural, electronic, and impurity-doping effects in nanoscale chemistry: supported gold nanoclusters.", Angew. Chem. Int. Ed. **42**, 1297 (2003).

[14] D. W. Yuan, Y. Wang, and Z. Zeng, "Geometric, electronic, and bonding properties of $\mathrm{Au}_N\mathrm{M}$ ($N = 1-7$, M = Ni, Pd, Pt) clusters.", J. Chem. Phys. **122**, 114310 (2005).

[15] M. Zhang, H. Zhang, L. Zhao, Y. Li, and Y. Luo, "Low-Energy Isomer Identification, Structural Evolution, and Magnetic Properties in Manganese-Doped Gold Clusters MnAu_n ($n = 1-16$).", J. Phys. Chem. A **116**, 1493 (2012).

[16] D. Dong, X.-Y. Kuang, J.-J. Guo, and B.-X. Zheng, "Geometries, stabilities, and magnetic properties of $\mathrm{Cr@Au}_n$ ($n = 1-8$) clusters: Density functional theory study.", Physica A **389**, 5216 (2010).

[17] D. Dong, K. Xiao-Yu, G. Jian-Jun, and Z. Ben-Xia, "Density functional theory study of $\mathrm{Au}_n\mathrm{Mn}$ ($n = 1-8$) clusters.", J. Phys. Chem. Solids **71**, 770 (2010).

[18] P. V. Nhat and M. T. Nguyen, "Trends in structural, electronic and energetic properties of bimetallic vanadium-gold clusters $\mathrm{Au}_n\mathrm{V}$ with $n = 1-14$.", PCCP **13**, 16254 (2011).

[19] B. R. Sahu, G. Maofa, and L. Kleinman, "Density-functional study of palladium-doped small gold clusters", Phys. Rev. B **67**, 115420 (2003).

[20] M.-X. Chen and X. H. Yan, "A new magic titanium-doped gold cluster and orientation dependent cluster-cluster interaction.", J. Chem. Phys. **128**, 174305 (2008).

[21] X. Li, B. Kiran, L.-F. Cui, and L.-S. Wang, "Magnetic Properties in Transition-Metal-Doped Gold Clusters: $\mathrm{M@Au}_6$ (M=Ti,V,Cr)", Phys. Rev. Lett. **95**, 253401 (2005).

[22] K. Koyasu, M. Mitsui, A. Nakajima, and K. Kaya, "Photoelectron spectroscopy of palladium-doped gold cluster anions ; $\mathrm{Au}_n\mathrm{Pd}^-$ ($n = 1-4$).", Chem. Phys. Lett. **358**, 224 (2002).

[23] L. Lin, P. Claes, T. Höltzl, E. Janssens, T. Wende, R. Bergmann, G. Santambrogio, G. Meijer, K. R. Asmis, M. T. Nguyen, and P. Lievens, “The structure of Au_6Y^+ in the gas phase.”, PCCP **12**, 13907 (2010).

[24] L. Lin, P. Claes, P. Gruene, G. Meijer, A. Fielicke, M. T. Nguyen, and P. Lievens, “Far-infrared spectra of yttrium-doped gold clusters Au_nY ($n = 1 - 9$).”, ChemPhysChem **11**, 1932 (2010).

[25] S. Neukermans, E. Janssens, H. Tanaka, R. Silverans, and P. Lievens, “Element- and Size-Dependent Electron Delocalization in Au_NX^+ Clusters (X=Sc, Ti, V, Cr, Mn, Fe, Co, Ni).”, Phys. Rev. Lett. **90**, 033401 (2003).

[26] E. Janssens, H. Tanaka, S. Neukermans, R. E. Silverans, and P. Lievens, “Two-dimensional magic numbers in mass abundances of photofragmented bimetallic clusters”, New J. Phys. **5**, 46 (2003).

[27] E. Janssens, H. Tanaka, S. Neukermans, R. E. Silverans, and P. Lievens, “Electron delocalization in Au_NX_M (X=Sc, Ti, Cr, Fe) clusters: A density functional theory and photofragmentation study.”, Phys. Rev. B **69**, 85402 (2004).

[28] H. Tanaka, S. Neukermans, E. Janssens, R. E. Silverans, and P. Lievens, “σ Aromaticity of the Bimetallic Au_5Zn^+ Cluster.”, JACS **125**, 2862–2863 (2003).

[29] N. Veldeman, E. Janssens, K. Hansen, J. De Haeck, R. E. Silverans, and P. Lievens, “Stability and dissociation pathways of doped Au_nX^+ clusters (X = Y, Er, Nb).”, Faraday Discuss. **138**, 147 (2008).

[30] L.-M. Wang, J. Bai, A. Lechtken, W. Huang, D. Schooss, M. M. Kappes, X. C. Zeng, and L.-S. Wang, “Magnetic doping of the golden cage cluster $M@Au_{16}^-$ (M=Fe,Co,Ni).”, Phys. Rev. B **79**, 033413 (2009).

[31] F. M. F. de Groot, “Multiplet effects in X-ray spectroscopy”, Coord. Chem. Rev. **249**, 31–63 (2005).

[32] K. Hirsch, V. Zamudio-Bayer, F. Ameseder, A. Langenberg, J. Rittmann, M. Vogel, T. Möller, B. v. Issendorff, and J. T. Lau, “2p x-ray absorption of free transition-metal cations across the 3d transition elements: Calcium through copper”, Phys. Rev. A **85**, 062501 (2012).

[33] M. Martins, K. Godehusen, T. Richter, P. Wernet, and P. Zimmermann, “Open shells and multi-electron interactions: core level photoionization of the 3d metal atoms”, J. Phys. B: At. Mol. Opt. Phys. **39**, R79–R125 (2006).

[34] M. Niemeyer, “Untersuchung der magnetischen Eigenschaften kleiner Eisencluster mit zirkularem magnetischem Röntgendichroismus”, diploma thesis (2012).

[35] J. Stöhr, “Exploring the microscopic origin of magnetic anisotropies with X-ray magnetic circular dichroism (XMCD) spectroscopy”, J. Magn. Magn. Mater. **200**, 470 (1999).

[36] B. T. Thole, P. Carra, F. Sette, and G. van der Laan, “X-Ray Circular Dichroism as a Probe of Orbital Magnetization.”, Phys. Rev. Lett. **68**, 1943 (1992).

[37] P. Carra, B. T. Thole, M. Altarelli, and X. Wang, “X-Ray Circular Dichroism and Local Magnetic Fields”, Phys. Rev. Lett. **70**, 694 (1993).

[38] C. T. Chen, Y. U. Idzerda, H.-J. Lin, N. V. Smith, G. Meigs, E. Chaban, G. H. Ho, E. Pellegrin, and F. Sette, “Experimental Confirmation of the X-Ray Magnetic Circular Dichroism Sum Rules for Iron and Cobalt.”, Phys. Rev. Lett. **75**, 152 (1995).

[39] M. Niemeyer, K. Hirsch, V. Zamudio-Bayer, A. Langenberg, M. Vogel, M. Kossick, C. Ebrecht, K. Egashira, A. Terasaki, T. Möller, B. von Issendorff, and J. T. Lau, “Spin Coupling and Orbital Angular Momentum Quenching in Free Iron Clusters”, Phys. Rev. Lett. **108**, 057201 (2012).

[40] M. Altarelli, “Sum rules for X-ray magnetic circular dichroism”, Il Nuovo Cimento **20 D**, 1067 (1998).

[41] R. Wu, D. Wang, and A. J. Freeman, “First Principles Investigation of the Validity and Range of Applicability of the X-Ray Magnetic Circular Dichroism Sum Rule”, Phys. Rev. Lett. **71**, 3581 (1993).

[42] G. van der Laan, “Sum rule practice.”, J. Synchrotron Rad. **6**, 694 (1999).

[43] R. Wu and A. J. Freeman, “Limitation of the Magnetic-Circular-Dichroism Spin Sum Rule for Transition Metals and Importance of the Magnetic Dipole Term”, Phys. Rev. Lett. **73**, 1994 (1994).

[44] C. Piamonteze, P. Miedema, and F. de Groot, “Accuracy of the spin sum rule in XMCD for the transition-metal L edges from manganese to copper”, Phys. Rev. B **80**, 184410 (2009).

[45] P. Gambardella, H. Brune, S. S. Dhesi, P. Bencok, S. R. Krishnakumar, S. Gardonio, M. Veronese, C. Grazioli, and C. Carbone, “Paramagnetic Mn impurities on Ge and GaAs surfaces”, Phys. Rev. B **72**, 045337 (2005).

[46] W. T. Elam, B. D. Ravel, and J. R. Sieber, “A New Atomic Database for X-Ray Spectroscopic Calculations”, Radiat. Phys. Chem. **63**, 121 (2002).

[47] L. Rayleigh, “On the Equilibrium of Liquid Conducting Masses charged with Electricity”, Philos. Mag. **14**, 184 (1882).

[48] K. Hirsch, J. T. Lau, P. Klar, A. Langenberg, J. Probst, J. Rittmann, M. Vogel, V. Zamudio-Bayer, T. Möller, and B. von Issendorff, “X-ray spectroscopy on size-selected clusters in an ion trap: from the molecular limit to bulk properties”, J. Phys. B: At. Mol. Opt. Phys. **42**, 154029 (2009).

[49] P. Coleman, *The evolving monogram on Many Body Physics.* (unpublished, 2012).

[50] F. Bloch, “Bemerkung zur Elektronentheorie des Ferromagnetismus und der elektrischen Leitfähigkeit.”, Z. Phys. **57**, 545 (1929).

[51] A. H. Wilson, “The Theory of Electronic Semi-Conductors”, Proc. R. Soc. London, Ser. A **133**, 458 (1931).

[52] J. Hubbard, “Electron Correlations in Narrow Energy Bands. II. The Degenerate Band Case”, Proc. R. Soc. London, Ser. A **277**, 237 (1964).

[53] J. Hubbard, “Electron Correlations in Narrow Energy Bands. III. An Improved Solution”, Proc. R. Soc. London, Ser. A **281**, 401 (1964).

[54] N. F. Mott, “The Basis of the Electron Theory of Metals, with Special Reference to the Transition Metals”, Proc. Phys. Soc. A **62**, 416 (1949).

[55] N. F. Mott and R. Peierls, “Discussion of the paper by de Boer and Verwey”, Proc. Phys. Soc. **49**, 72 (1937).

[56] G. Kotliar and D. Vollhardt, “Strongly Correlated Materials : Insights From Dynamical Mean-Field Theory”, Phys. Today, 53 (2004).

[57] J. L. Smith and E. A. Kmetko, “Magnetism or bonding: A nearly periodic table of transition elements”, J. Less-Common Met. **90**, 83 (1983).

[58] J. G. Bednorz and K. A. Müller, “Possible High $\mathrm{T_c}$ Superconductivity in the Ba-La-Cu-O System”, Z. Phys. B: Condens. Matter **64**, 189 (1986).

[59] M. N. Baibich, J. M. Broto, A. Fert, F. Nguyen Van Dau, F. Petroff, P. Etienne, G. Creuzet, A. Friedrich, and J. Chazelas, “Giant Magnetoresistance of (001)Fe/(001)Cr Magnetic Superlattices”, Phys. Rev. Lett. **61**, 2472 (1988).

[60] G. Binasch, P. Grünberg, F. Saurenbach, and W. Zinn, “Enhanced magnetoresistance in layered magnetic structures with antiferromagnetic interlayer exchange”, Phys. Rev. B **39**, 4828 (1989).

[61] A. C. Hewson, *The Kondo Problem to Heavy Fermions (Cambridge Studies in Magnetism)*, edited by D. Edwards and D. Melville (Cambridge University Press, Cambridge, 1993).

[62] B. Surer, "First-principles simulations of multi-orbital systems with strong electronic correlations", PhD thesis (ETH Zürich, 2011).

[63] K. Capelle, "A bird's-eye view of density-functional theory", Braz. J. Phys. **36**, 1318 (2006).

[64] R. G. Parr and W. Yang, "Density-Functional Theory of the Electronic Structure of Molecules", Annu. Rev. Phys. Chem. **46**, 701 (1995).

[65] W. Koch and M. C. Holthausen, *A Chemist's Guide to Density Functional Theory* (Wiley-VCH, Weinheim, 2000).

[66] R. G. Parr and W. Yang, *Density Functional Theory of Atoms and Molecules* (Oxford University Press USA, New York, 1989).

[67] J. P. Perdew and S. Kurth, "Density Functionals for Non-relativistic Coulomb Systems in the New Century", in *A primer in density functional theory*, edited by C. Fiolhais, M. A. L. Marques, and F. Nogueira (Springer-Verlag, Berlin Heidelberg New York, 2003), pp. 1–55.

[68] M. Dreizler and E. K. U. Gross, *Density Functional Theory: An Approach to the Quantum Many-Body Problem* (Springer, Berlin, 1990).

[69] P. Hohenberg and W. Kohn, "Inhomogeneous Electron Gas", Phys. Rev. **136**, B864 (1964).

[70] W. Kohn and L. J. Sham, "Self-Consistent Equations Including Exchange and Correlation Effects", Phys. Rev. **140**, A1133 (1965).

[71] J. P. Perdew, R. G. Parr, M. Levy, and J. L. Balduz, "Density-Functional Theory for Fractional Particle Number: Derivative Discontinuities of the Energy", Phys. Rev. Lett. **49**, 1691 (1982).

[72] M. Cococcioni and S. de Gironcoli, "Linear response approach to the calculation of the effective interaction parameters in the LDA+U method", Phys. Rev. B **71**, 035105 (2005).

[73] K. Terakura, T. Oguchi, A. R. Williams, and J. Kübler, "Band theory of insulating transition-metal monoxides: Band-structure calculations", Phys. Rev. B **30**, 4734 (1984).

[74] T. C. Leung, C. T. Chan, and B. N. Harmon, "Ground-state properties of Fe, Co, Ni, and their monoxides: Results of the generalized gradient approximation", Phys. Rev. B **44**, 2923 (1991).

[75] P. Dufek, P. Blaha, V. Sliwko, and K. Schwarz, “Generalized-gradient-approximation description of band splittings in transition-metal oxides and fluorides”, Phys. Rev. B **49**, 10170 (1994).

[76] S. Kümmel and L. Kronik, “Orbital-dependent density functionals: Theory and applications”, Rev. Mod. Phys. **80**, 3 (2008).

[77] V. I. Anisimov, J. Zaanen, and O. K. Andersen, “Band theory and Mott insulators: Hubbard U instead of Stoner I”, Phys. Rev. B **44**, 943 (1991).

[78] V. I. Anisimov and O. Gunnarsson, “Density-functional calculation of effective Coulomb interactions in metals”, Phys. Rev. B **43**, 7570 (1991).

[79] V. I. Anisimov, F. Aryasetiawan, and A. I. Lichtenstein, “First-principles calculations of the electronic structure and spectra of strongly correlated systems: the LDA + U method”, J. Phys. Condens. Matter **9**, 767 (1997).

[80] V. I. Anisimov, I. V. Solovyev, M. A. Korotin, M. T. Czyzyk, and G. A. Sawatzky, “Density-functional theory and NiO photoemission spectra”, Phys. Rev. B **48**, 16929 (1993).

[81] A. I. Lichtenstein, V. I. Anisimov, and J. Zaanen, “Density-functional theory and strong interactions: Orbital ordering in Mott-Hubbard insulators”, Phys. Rev. B **52**, 5467 R (1995).

[82] M. S. Hybertsen, M. Schlüter, and N. E. Christensen, “Calculation of Coulomb-interaction parameters for La_2CuO_4 using a constrained-density-functional approach”, Phys. Rev. B **39**, 9028 (1989).

[83] W. E. Pickett, S. C. Erwin, and E. C. Ethridge, “Reformulation of the LDA+U method for a local-orbital basis”, Phys. Rev. B **58**, 1201 (1998).

[84] H. Kulik, M. Cococcioni, D. Scherlis, and N. Marzari, “Density Functional Theory in Transition-Metal Chemistry: A Self-Consistent Hubbard U Approach”, Phys. Rev. Lett. **97**, 103001 (2006).

[85] H. J. Kulik and N. Marzari, “Systematic study of first-row transition-metal diatomic molecules: a self-consistent DFT+U approach”, J. Chem. Phys. **133**, 114103 (2010).

[86] P. Giannozzi, S. Baroni, N. Bonini, M. Calandra, R. Car, C. Cavazzoni, D. Ceresoli, G. L. Chiarotti, M. Cococcioni, I. Dabo, A. Dal Corso, S. de Gironcoli, S. Fabris, G. Fratesi, R. Gebauer, U. Gerstmann, C. Gougoussis, A. Kokalj, M. Lazzeri, L. Martin-Samos, N. Marzari, F. Mauri, R. Mazzarello, S. Paolini, A. Pasquarello, L. Paulatto, C. Sbraccia, S. Scandolo, G. Sclauzero, A. P. Seitsonen, A. Smogunov, P. Umari, and R. M. Wentzcovitch, "QUANTUM ESPRESSO: a modular and open-source software project for quantum simulations of materials.", J. Phys. Condens. Matter **21**, 395502 (2009).

[87] C. Raas, "Dynamic Density-Matrix Renormalization for the Symmetric Single Impurity Anderson Model", PhD thesis (Universität Köln, 2005).

[88] P. W. Anderson, "A poor man' s derivation of scaling laws for the Kondo problem", J. Phys. C: Solid State Phys. **3**, 2436 (1970).

[89] W. J. de Haas, J. de Boer, and G. J. van den Berg, "The electrical resistance of gold, copper and lead at low temperatures", Physica **1**, 1115 (1934).

[90] J. R. Schrieffer and P. A. Wolff, "Relation between the Anderson and Kondo Hamiltonians", Phys. Rev. **149**, 491 (1966).

[91] K. Hirsch, "Röntgenabsorptionsspektroskopie an freien, massenselektierten Metallclustern", diploma thesis (2008).

[92] A. Langenberg, "Magnetische Momente freier, massenselektierter Eisen-, Cobalt- und Nickelcluster", PhD thesis (Technische Universität Berlin, 2013).

[93] J. Rittmann, "Electronic Properties of Transition Metal Doped Silicon Clusters", PhD thesis (Technische Universität Berlin, 2011).

[94] D. Gerlich, "Inhomogeneous RF-Fields - A Versatile Tool for the Study of Processes With Slow Ions", Adv. Chem. Phys. **82**, 1 (1992).

[95] JASTEC, *Operating Manual of the Superconducting Magnet System JMTD- 5T100L*, 2005.

[96] H. Adam, W. Walcher, and M. Wutz, *Handbuch der Vakuumtechnik*, 6. (Vieweg, 1997).

[97] W. C. Wiley and I. H. McLaren, "Time-of-Flight Mass Spectrometer with Improved Resolution", Rev. Sci. Instrum. **26**, 1150 (1955).

[98] W. Gohl, R. Kutscher, H. J. Laue, and H. Wollnik, "Time-of-Flight Mass Spectrometry for Ions of Large Energy Spread", Int. J. Mass Spectrom. Ion Phys. **48**, 411 (1983).

[99] U. Boesl, R. Weinkauf, and E. W. Schlag, “Review Reflectron time-of-flight mass spectrometry and laser excitation for the analysis of neutrals, ionized molecules and secondary fragments”, Int. J. Mass Spectrom. Ion Processes **112**, 121 (1992).

[100] G. Margaritondo, “Synchrotron Light in a Nutshell”, Surf. Rev. Lett. **7**, 379 (2000).

[101] G. Margaritondo, “A Primer in Synchrotron Radiation: Everything You Wanted to Know about SEX (Synchrotron Emission of X-rays) but Were Afraid to Ask.”, J. Synchrotron Rad. **2**, 148 (1995).

[102] T. Möller and J. Falta, eds., *Forschung mit Synchrotronstrahlung: Eine Einführung in die Grundlagen und Anwendungen* (Vieweg+Teubner, 2010).

[103] R. Follath, “Commissioning of the U49/2-PGM1 beamline”, AIP Conference Proceedings **705**, 348 (2004).

[104] R. Follath and F. Senf, “New plane-grating monochromators for third generation synchrotron radiation light sources”, Nucl. Instrum. Methods Phys. Res., Sect. A **390**, 388 (1997).

[105] A. C. Thompson and D. Vaughan, eds., *X-ray data booklet* (Lawrence Berkeley National Laboratory University of California, 2001).

[106] F. Weigend and R. Ahlrichs, “Balanced basis sets of split valence, triple zeta valence and quadruple zeta valence quality for H to Rn: Design and assessment of accuracy.”, PCCP **7**, 3297 (2005).

[107] J. P. Perdew, K. Burke, and M. Ernzerhof, “Generalized Gradient Approximation Made Simple”, Phys. Rev. Lett. **77**, 3865 (1996).

[108] F. M. F. de Groot, “X-ray absorption and dichroism of transition metals and their compounds”, J. Electron. Spectrosc. Relat. Phenom. **67**, 529 (1994).

[109] G. van der Laan and I. W. Kirkman, “The 2p absorption spectra of 3d transition metal compounds in tetrahedral and octahedral symmetry”, J. Phys. Condens. Matter **4**, 4189 (1992).

[110] P.-O. Löwdin, “On the Non-Orthogonality Problem Connected with the Use of Atomic Wave Functions in the Theory of Molecules and Crystals”, J. Chem. Phys. **18**, 365 (1950).

[111] P.-O. Löwdin, “On the Nonorthogonality Problem”, Adv. Quantum Chem. **5**, 185 (1970).

[112] S. G. Wang, Y. X. Qiu, H. Fang, and W. H. E. Schwarz, “The challenge of the so-called electron configurations of the transition metals.”, Chem. Eur. J. **12**, 4101 (2006).

[113] J. T. Lau, J. Rittmann, V. Zamudio-Bayer, M. Vogel, K. Hirsch, P. Klar, F. Lofink, T. Möller, B. von Issendorff, and B. v. Issendorff, “Size Dependence of $L_{2,3}$ Branching Ratio and 2p Core-Hole Screening in X-Ray Absorption of Metal Clusters”, Phys. Rev. Lett. **101**, 153401 (2008).

[114] K. Hirsch, V. Zamudio-Bayer, J. Rittmann, A. Langenberg, M. Vogel, B. v. Issendorff, and J. T. Lau, “Initial- and final-state effects on screening and branching ratio in 2 p x-ray absorption of size-selected free 3d transition metal clusters”, Phys. Rev. B **86**, 165402 (2012).

[115] R. S. Mulliken, “Electronic Population Analysis on LCAO-MO Molecular Wave Functions. I”, J. Chem. Phys. **23**, 1833 (1955).

[116] C. Ehrhardt and R. Ahlrichs, “Population analysis based on occupation numbers II. Relationship between shared electron numbers and bond energies and characterization of hypervalent contributions”, Theor. Chim. Acta, 231 (1985).

[117] W. Heitler and F. London, “The Combination of Two Hydrogen Atoms.”, Z. Phys. **44**, 455 (1927).

[118] H. Häkkinen, Y. Bokwon, U. Landman, X. Li, H.-J. Zhai, and L.-S. Wang, “On the Electronic and Atomic Structures of Small Au_N^- ($N = 4-14$) Clusters : A Photoelectron Spectroscopy and Density-Functional Study”, J. Phys. Chem. A **107**, 6168 (2003).

[119] H. Häkkinen and U. Landman, “Gold clusters (Au_N , $2 \leq N \leq 10$) and their anions”, Phys. Rev. B **62**, 2287 (2000).

[120] H. Häkkinen, “Atomic and electronic structure of gold clusters: understanding flakes, cages and superatoms from simple concepts.”, Chem. Soc. Rev. **37**, 1847 (2008).

[121] J. Sugar and C. Corliss, “Atomic-Energy Levels of the Iron-Period Elements - Potassium through Nickel”, J. Phys. Chem. Ref. Data **14**, 1 (1985).

[122] E. M. Fernández, J. M. Soler, I. L. Garzón, and L. C. Balbás, “Trends in the structure and bonding of noble metal clusters”, Phys. Rev. B **70**, 165403 (2004).

[123] B. Assadollahzadeh and P. Schwerdtfeger, “A systematic search for minimum structures of small gold clusters Au_n ($n = 2 - 20$) and their electronic properties.”, J. Chem. Phys. **131**, 064306 (2009).

[124] L. Iglesias, M. I. Cabeza, and B. de Luis, “Energy Levels of V Cation”, Pub. Inst. Opt. Madrid **47**, 1 (1988).

[125] M. Vogel, C. Kasigkeit, K. Hirsch, A. Langenberg, J. Rittmann, V. Zamudio-Bayer, A. Kulesza, R. Mitri, T. Möller, B. v. Issendorff, and J. T. Lau, “2 p core-level binding energies of size-selected free silicon clusters : Chemical shifts and cluster structure”, Phys. Rev. B **85**, 195454 (2012).

[126] G. van der Laan, “Theory of simple spectra”, J. Electron. Spectrosc. Relat. Phenom. **86**, 41 (1997).

[127] R. D. Cowan, *The Theory of Atomic Structure and Spectra.* (University of California Press, 1981).

[128] K. Yosida, A. Okiji, and C. Soshin, “Magnetic Anisotropy of Localized State in Metals”, Prog. Theor. Phys. **33**, 559 (1965).

[129] E. Sasioglu, C. Friedrich, and S. Blügel, “Effective Coulomb interaction in transition metals from constrained random-phase approximation”, Phys. Rev. B **83**, 121101 (R) (2011).

[130] R. Skomski, R. Zhang, P. Kharel, A. Enders, S.-H. Liou, and D. J. Sellmyer, “Magnetic susceptibility of nanoscale Kondo systems”, J. Appl. Phys. **107**, 09E126 (2010).

[131] G. M. Pastor, “Magnetic impurities in small metal clusters”, Ann. Phys. **14**, 547 (2005).

[132] R. Kaul, D. Ullmo, G. Zaránd, S. Chandrasekharan, and H. Baranger, “Ground state and excitations of quantum dots with magnetic impurities”, Phys. Rev. B **80**, 035318 (2009).

[133] R. Kaul, G. Zaránd, S. Chandrasekharan, D. Ullmo, and H. Baranger, “Spectroscopy of the Kondo Problem in a Box”, Phys. Rev. Lett. **96**, 176802 (2006).

[134] I. Affleck, “The Kondo screening cloud: what it is and how to observe it”, arXiv **:0911.2209** (2010).

[135] R. K. Kaul, D. Ullmo, S. Chandrasekharan, and H. U. Baranger, “Mesoscopic Kondo problem”, Europhys. Lett. **71**, 973 (2005).

[136] S. Rotter and Y. Alhassid, “Strong-coupling limit of a Kondo spin coupled to a mesoscopic quantum dot: Effective Hamiltonian in the presence of exchange correlations”, Phys. Rev. B **80**, 184404 (2009).

[137] D. E. Liu, S. Burdin, H. Baranger, and D. Ullmo, “Mesoscopic Anderson box: Connecting weak to strong coupling”, Phys. Rev. B **85**, 155455 (2012).

[138] W. Thimm, J. Kroha, and J. von Delft, “Kondo Box: A Magnetic Impurity in an Ultrasmall Metallic Grain”, Phys. Rev. Lett. **82**, 2143 (1999).

[139] P. Cornaglia and C. Balseiro, “Kondo impurities in nanoscopic systems: Confinement-induced regimes”, Phys. Rev. B **66**, 115303 (2002).

[140] B. von Issendorff, *Personal communication.*

[141] C. Kittel, *Introduction to Solid State Physics*, 8th (NJ: John Wiley and Sons, Inc, Hoboken, 2005).

[142] R. Ahlrichs, M. Bär, M. Häser, H. Horn, and C. Kölmel, “Electronic Structure Calculations on Workstation Computers: The Program System Turbomole”, Chem. Phys. Lett. **162**, 165 (1989).

[143] P. Deglmann, K. May, F. Furche, and R. Ahlrichs, “Nuclear second analytical derivative calculations using auxiliary basis set expansions”, Chem. Phys. Lett. **384**, 103 (2004).

[144] K. Eichkorn, O. Treutler, H. Öhm, M. Häser, and R. Ahlrichs, “Auxiliary basis sets to approximate Coulomb potentials”, Chem. Phys. Lett. **240**, 283 (1995).

[145] X. Chu, M. Xiang, Q. Zeng, W. Zhu, and M. Yang, “Competition between monomer and dimer fragmentation pathways of cationic Cu_N clusters of $N = 2 - 20$”, J. Phys. B: At. Mol. Opt. Phys. **44**, 205103 (2011).

[146] P. Calaminici, A. M. Köster, N. Russo, and D. R. Salahub, “A density functional study of small copper clusters: Cu_n $(n \leq 5)$”, J. Chem. Phys. **105**, 9546 (1996).

[147] H. Häkkinen, M. Moseler, and U. Landman, “Bonding in Cu, Ag, and Au Clusters: Relativistic Effects, Trends, and Surprises”, Phys. Rev. Lett. **89**, 033401 (2002).

[148] C.-Y. Cha, G. Ganteför, and W. Eberhardt, “Photoelectron spectroscopy of Cu_n^- clusters: Comparison with jellium model predictions”, J. Chem. Phys. **99**, 6308 (1993).

[149] K. J. Taylor, C. L. Pettiette-Hall, O. Cheshnovsky, and R. E. Smalley, “Ultraviolet photoelectron spectra of coinage metal clusters”, J. Chem. Phys. **96**, 3319 (1992).

[150] C. L. Pettiette, S. H. Yang, M. J. Craycraft, J. Conceicao, R. T. Laaksonen, O. Cheshnovsky, and R. E. Smalley, “Ultraviolet photoelectron spectroscopy of copper clusters”, J. Chem. Phys. **88**, 5377 (1988).

[151] M. Itoh, V. Kumar, T. Adschiri, and Y. Kawazoe, “Comprehensive study of sodium, copper, and silver clusters over a wide range of sizes $2 \leq N \leq 75$.”, J. Chem. Phys. **131**, 174510 (2009).

[152] P. J. Braspenning, R. Zeller, A. Lodder, and P. H. Dederichs, “Self-consistent cluster calculations with correct embedding for $3d$, $4d$, and some *sp* impurities”, Phys. Rev. B **29**, 703 (1984).

[153] S. Frota-Pessôa, “First-principles real-space linear-muffin-tin-orbital calculations of 3d impuritites in Cu”, Phys. Rev. B **46**, 14570 (1992).

[154] W. D. Weiss, “Localized Magnetic Moments in Diluted Solid Solutions of Titanium Vanadium Chromium and Manganese in Pure Copper”, Z. Metallkd. **58**, 909 (1967).

[155] C. E. Moore, “Atomic Energy Levels”, Natl. Bur. Stand. (U.S.) Circ. **I-III**.

[156] Y. J. Wang and J. W. Davenport, “Relativistic effects on the $s \rightarrow d$ promotion energy and spin-polarization energy of the transition metals”, Phys. Rev. A **41**, 4690 (1990).

Chapter 8

Appendix

8.1 Coordinates of $CrCu_n^+$ Clusters

All distances are given in Å.

$CrCu_1^+$ ground state	x	y	z
Cu	-2.8096432	2.1443083	0.0000000
Cr	-0.0724060	2.1773405	0.0000000

$CrCu_2^+$ ground state	x	y	z
Cu	-2.7820222	2.0691877	0.0000000
Cu	-1.7583713	-0.0300738	0.0000000
Cr	-0.2368152	2.0116150	0.0000000

$CrCu_2^+$ first isomer	x	y	z
Cu	-0.0000000	-0.0000000	0.0557006
Cu	0.0000000	0.0000000	2.3941831
Cr	0.0000000	0.0000000	-2.4498837

$CrCu_2^+$ second isomer	x	y	z
Cu	0.0000000	0.0000000	-2.5504625
Cu	0.0000000	0.0000000	2.5504626
Cr	0.0000000	0.0000000	0.0000000

$CrCu_3^+$ ground state	x	y	z
Cu	-2.1505923	-0.3483559	1.2545071
Cu	-3.5330069	0.5047884	-0.4706835
Cu	-2.8398571	1.8686943	-2.2797694
Cr	-1.1131110	1.1857723	-0.5157236

$CrCu_3^+$ first isomer	x	y	z
Cu	-3.8090847	1.3503527	-0.0364732
Cu	-2.7780393	0.7544706	-2.0562519
Cu	-5.1325497	0.3423142	-1.7752698
Cr	-1.2350227	1.8593313	-0.2323240

$CrCu_4^+$ ground state	x	y	z
Cu	-4.1048699	1.7694397	0.0140550
Cu	-1.8233374	0.9714893	-0.4527150
Cu	-5.8467743	0.9137523	-1.5031206
Cu	-3.8247137	-0.3771064	-0.9450439
Cr	-3.4683194	1.6351437	-2.4223941

$CrCu_4^+$ first isomer	x	y	z
Cu	-3.4783818	0.3372498	0.0000000
Cu	-1.7865323	-1.5293825	-0.0000000
Cu	0.5394157	-1.1959252	0.0000000
Cu	-2.9157225	2.6200534	-0.0000000
Cr	-1.0131866	0.8742243	0.0000000

$CrCu_4^+$ second isomer	x	y	z
Cu	-3.7749336	2.2958538	-0.0000007
Cu	-0.9186915	-1.5478900	0.0000006
Cu	-1.4550412	2.6911512	0.0000008
Cu	-2.2178529	0.4366716	0.0000000
Cr	0.3526315	0.6234522	-0.0000008

$CrCu_5^+$ ground state	x	y	z
Cu	-5.3025571	-2.6623380	0.5859749
Cu	-4.3078724	-0.5817841	-0.1887269
Cu	-1.8702858	-0.6260682	-0.1921873
Cu	-0.9491436	-2.7407853	0.5799354
Cu	-3.1284857	-2.7701099	-0.4867023
Cr	-3.1075401	-1.7666213	1.7702456

$CrCu_5^+$ first isomer	x	y	z
Cu	-5.2401760	-2.6827573	0.7113284
Cu	-4.4019011	-0.6094780	-0.1708348
Cu	-1.0526985	-2.8318225	0.7355800
Cu	-3.1188604	-2.7245492	-0.5611099
Cu	-3.0989335	-1.8133781	1.5979678
Cr	-1.7533153	-0.4857217	-0.2443920

CrCu$_5^+$ second isomer	x	y	z
Cu	1.5167037	0.6420737	-0.1712256
Cu	0.7337849	-1.5356580	0.1936203
Cu	-2.4023426	1.0673920	1.0762432
Cu	-0.1806753	0.2853206	1.6103346
Cu	1.0121314	-0.7627699	-2.1441690
Cr	-0.9553931	0.1766146	-0.7765314

CrCu$_6^+$ ground state	x	y	z
Cu	1.2680685	1.7445335	-0.0458994
Cu	0.0000000	0.0004092	-1.1595719
Cu	2.0510249	-0.6666058	-0.0463570
Cu	-2.0510249	-0.6666058	-0.0463570
Cu	-1.2680685	1.7445335	-0.0458994
Cu	-0.0000000	-2.1565600	-0.0454908
Cr	-0.0000000	0.0003053	1.3895754

CrCu$_6^+$ first isomer	x	y	z
Cu	1.2961846	1.6998437	0.0000000
Cu	0.0045176	-0.0054914	-1.1897664
Cu	0.0045176	-0.0054914	1.1897664
Cu	2.0501430	-0.7076098	0.0000000
Cu	-2.0171049	-0.7071098	0.0000000
Cu	0.0388649	-2.1680662	0.0000000
Cr	-1.3771227	1.8939348	0.0000000

CrCu$_6^+$ second isomer	x	y	z
Cu	-2.0054171	-5.5562396	-2.6403927
Cu	-4.0808899	-4.8003748	-1.6800297
Cu	-3.7190511	-3.0086048	0.0779657
Cu	-1.3857893	-2.4886761	0.3709471
Cu	-1.9027572	-4.7156239	-0.3859186
Cu	-5.1192088	-2.6331658	-1.8449734
Cr	-2.4285410	-2.9255677	-2.1013761

Acknowledgments

The presented thesis results from research activities at Technische Universität Berlin and Helmholtz Zentrum Berlin, where I had the pleasure to work with many people who supported me during the last years and whom I would like to thank here.

First of all I thank my supervisor Thomas Möller who not only gave me the opportunity to join his group, but also the freedom to choose a research topic not belonging to his main focus of research. I will remember his friendly, uncomplicated attitude and the possibility to drop by into his office whenever finding myself in any kind of trouble.
I am deeply indebted to Tobias Lau who has drawn me into cluster physics. He impressed me with his stamina in long beam-times, especially in the early stages of the experiment, and his everlasting enthusiasm. Scientifically, I benefited from countless discussions and extensive lab experience with him. Moreover, working with him always was a lot of fun.
I am grateful to Bernd von Issendorff, not only for reviewing this thesis. He constantly supported us with his enormous experimental experience and played a brilliant devil's advocate, thereby giving me insights into his deep understanding of physics.
I was very lucky to work together with two good friends: Jochen Rittmann and Vicente Zamudio-Bayer with whom I shared an office during the beginning of the PhD project at the TUB. We also spend uncounted hours together in the lab and at the beam-line. It really was a great time!
Coffee breaks at *Chez Marcel* were essential to overcome the fatigue in the afternoon, thanks for letting me disturb you in your office Marcel Pagels and Falk Reinhardt. I thank also the the last active member of the legendary PG 272, Max Bügler.
I like to thank Andreas Langenberg, the most patient guy I know, for designing the XMCD setup and sharing loads of funny night shifts.
Of course I want to thank all the other great people who were associated to the group at some time: Marlene Vogel, Jörg Wittich, Markus Niemeyer, Jürgen

Probst, and Arkadiusz Ławicki.

I am very thankful for the constant support by my family. Especially, I thank my brother Alexander Hirsch and his wife Mae Voon for proof-reading parts of this thesis.

For delivering numerous excellent parts I like to acknowledge the workshop.
I thank Akira Terasaki for providing the superconducting solenoid essential to perform the XMCD studies.
Calculations were carried out on the FOR 1282 computing cluster.

I thank my beloved girlfriend Linn Leppert for countless things. She encouraged me, gave me lot of advice concerning the DFT calculations, cheered me up, and furthermore proof-read this thesis over and over again. I thank you!